NORTHWESTERN UNIVERSITY

Advances in Normal and Surface-Enhanced Raman Spectroscopy for Single-Molecule Electrochemistry and Non-Invasive Molecular Sensing

A DISSERTATION

SUBMITTED TO THE GRADUATE SCHOOL IN PARTIAL FULFILLMENT OF THE REQUIREMENTS

for the degree

DOCTOR OF PHILOSOPHY

Field of Chemistry

By

Stephanie M. Zaleski

EVANSTON, ILLINOIS

December 2016

Abstract

Advances in Normal and Surface-Enhanced Raman Spectroscopy for Single-Molecule Electrochemistry and Non-Invasive Molecular Sensing

Raman spectroscopy is an established and versatile molecular sensing technique, but it is limited by its modest chemical sensitivity. Surface-enhanced Raman spectroscopy (SERS) can amplify otherwise weak normal Raman signals up to nine to ten orders of magnitude, giving rise to its application in many molecular sensing problems, including those in catalysis, biosensing, and art conservation. Additionally, the excellent molecular sensitivity of SERS can be applied to studying chemical reactions at the single molecule limit. The first half of this thesis will highlight progress in monitoring single electron transfer reactions with single-molecule SERS (SMSERS) and its implications for nanoscale electrochemistry. We will then present the optimization of a procedure to covalently functionalize SERS-active substrates with a redox active molecule, which can achieve the ultimate goal of simultaneously monitoring both redox states of an electrochemical reaction with SMSERS. The second half of this thesis will explore the use of both NRS and SERS as non-invasive and label-free sensing techniques for point-of-care applications. We first investigate the limits of detection of both NRS and EC-SERS for use in intravenous (IV) therapy drug sensing and successfully demonstrate the ability to use both a tabletop and handheld Raman setup to perform IV drug sensing experiments. We then present a non-invasive means of detecting atherosclerotic plaques using spatially-offset Raman spectroscopy. Overall, the work presented in this thesis highlights the versatility of information obtained from Raman spectroscopy and SERS, as well as its applicability to a broad spectrum of molecular sensing problems. The work presented herein paves future pathways for the further implementation of SERS in the fields of nanoscale electrochemistry and point-of-care sensing.

Stephanie M. Zaleski

Professor Richard P. Van Duyne

Research Advisor

Acknowledgements

My first acknowledgment is to my advisor Richard P. Van Duyne. Throughout my 5 years at Northwestern, I have experienced first-hand his dedication to both research and the overall well-being of his group members. I am inspired by his vast knowledge of what seems like everything (added bonus: he is a pro at Jeopardy), his constant generation of new ideas and his willingness to push the boundaries in his field – it drives me to think outside of the box when I would otherwise not do so. I also deeply appreciate his willingness to support my fairly non-traditional career path of conservation science. One could not ask for a better Ph.D. advisor and my sincerest thanks goes out to him for his enthusiasm, guidance and support throughout my graduate career.

I would like to thank my committee members Eric Weitz and Chad Mirkin, as well as my qualifying exam committee members Emily Weiss (my qualifying exam chair) and Toru Shiozaki. They pushed me to think critically about my science and how to approach research problems on a level I do not think I could have achieved on my own, and I believe that I am a much better scientist because of it. I am very grateful for their constructive criticism and feedback on my research progress throughout my time at Northwestern.

I would also like to acknowledge Francesca Casadio and Mark Ratner, with whom I have had the pleasure of collaborating. Francesca opened opportunities up for me that have been instrumental for the early development of my career path, and I am very excited to work with her more in the future. Working with Mark and his group has been very enjoyable and productive, and discussing science with Mark in a meeting is usually the highlight of my day because of his cheery disposition and enthusiasm for research.

I was very lucky to be surrounded by labmates who were both great people and excellent scientists. In particular, learning from and working alongside Jordan Klingsporn, Nathan Greeneltch, Federica Pozzi, Bhavya Sharma, and Fernanda Cardinal has been instrumental in my development as a scientist and I am extremely appreciative of the guidance and support they have given me throughout the years. I would also like to thank Mike Mattei, Natalie Gruenke, Lauren Buchanan, Hannah Mayhew, Alyssa Zrimsek, Eric Pozzi, Jon Dieringer and Alex Peroff for endless conversations about life, science, and everything in between. And I of course cannot leave out my two stellar undergraduate students, Kathleen Clark and Madison Smith, who were so much fun to work with and inspired me to be the best mentor that I could be.

Outside of lab, I never imagined having a group of friends that felt like a little Chicago/Northwestern family. I have had the great joy of spending most of my free time outside of lab with Jason Avila, Natalie Gruenke, Megan Shelby, David Weinberg, Dan Hannah, Nick Calta, Taylor Page, Charlie Macko, Evan Gilbert, Amber Davis, and Will Hoffeditz. Looking back at hundreds of takeout meals, drinks, board game sessions and sarcastic quips, I can’t imagine a better way to have spent my weekends in graduate school. Thank you all from the bottom of my heart for being some of the funniest and coolest people I know. I also want to acknowledge my Barnard College friends Alisha Kaplan, Willie Avendano, Dueaa Elzin and Shazeeda Bhola for their encouragement and support – I am so thankful for their friendship and I am proud of how successful they have all become.

My most heartfelt acknowledgment goes out to my parents, Ken and Shelley Zaleski and my sister, Maddy Zaleski. Through the good and the bad, my parents have been nothing short of amazing throughout my entire academic career. I would not be where I am today without their tireless love and support (and occasional but necessary nagging). Words cannot express how much they mean to me, and I am so grateful for all that they have done for me.

Last but not least, I would like to thank my boyfriend Jason Avila. I couldn’t imagine a better person to share my love of cheap food, weird music, cartoons and general nerdom with. He is my cynical, vastly intelligent and sarcastic rock and I wouldn’t have it any other way. Thank you so much for always telling me: “Believe in me, who believes in you!” I think I believe it now after all this time. I can’t wait to see what the future holds for us.

Table of Contents

Chapter 1. Introduction......15

1.1. Motivation...... 16

1.2. Surface-enhanced Raman Spectroscopy...... 17

1.2.1. Origin of SERS and SERS Enhancement Mechanisms...... 17

1.2.2. SERS substrates, “Hot spots” and Enhancement Factors...... 19

1.3. Single-Molecule SERS (SMSERS)...... 22

1.3.1. Beginnings of SMSERS: First Demonstrations and Development of SMSERS Proofs...... 22

1.3.2. Using SMSERS to Monitor Chemical Reactions...... 24

1.4. Investigating Nanoscale Electrochemistry with Surface-Enhanced Raman Spectroscopy...... 28

1.4.1. Introduction...... 28

1.4.2. Current Progress in EC-SMSERS...... 30

1.4.3. Redox-Active Molecules, Substrates and Substrate Functionalization for EC-SMSERS...... 34

1.5. Conclusions and Thesis Overview...... 38

Chapter 2. Observing Single, Heterogeneous, One-Electron Transfer Reactions with Single Molecule SERS......39

2.1. Introduction...... 40

2.2. Experimental Details 44

2.3. Results and Discussion 49

2.3.1. Electrochemical Characterization of R6G System 49

2.3.2. Proof of SMSERS Behavior 53

2.3.3. EC-SMSERS Signal Potential Dependence 54

2.4. Conclusions 62

Chapter 3. Towards Monitoring Electrochemical Reactions with Dual-wavelength SERS: Characterization of R6G Neutral Radical Species and Covalent Tethering of R6G to Silver Nanoparticles 64

3.1. Introduction 65

3.2. Experimental 69

3.3. Results and Discussion 74

3.3.1. Characterization of the R6G Neutral Radical Species with EC-RRS 74

3.3.2. EDC Crosslinking of R6G on Ag Nanoparticles for EC-SERS 80

3.4. Conclusions and Future Work 92

Chapter 4. Rapid Identification and Quantification of Intravenous Therapy Drugs using Normal Raman Spectroscopy and Electrochemical Surface-Enhanced Raman Spectroscopy 93

4.1. Introduction 94

4.2. Experimental Details 97

4.3. Results and Discussion 100
  4.3.1. Normal Raman Spectroscopy of Gentamicin 100
  4.3.2. Electrochemical SERS of Dobutamine 107
4.4. Conclusions and Future Work 115

Chapter 5. Noninvasive Identification of Atherosclerotic Plaques with Spatially Offset Raman Spectroscopy 116

5.1. Introduction... 117
5.2. Experimental Details.. 120
5.3. Results and Discussion 122
5.4. Conclusions and Future Directions... 124

List of Figures

Figure 1.1 Physical origins of SERS. 18

Figure 1.2 Film over nanosphere SERS substrates. 20

Figure 1.3 Frequency domain proof of SMSERS. 23

Figure 1.4 Photocatalytic conversion of *para*-nitrothiophenol to thiophenol on AuNPs. 25

Figure 1.5 SMSERS detection of curcubit[7]uril host-guest complex. 27

Figure 1.6 Surface-dependent nanoscale electrochemistry. 29

Figure 1.7 Electrochemical super-localization SMSERS imaging of Nile Blue. 32

Figure 1.8 Representative EM images of SERS-active substrates that can be implemented for EC-SERS. 36

Figure 2.1 Electrochemical characterization of R6G. 42

Figure 2.2 Preparation of EC-SMSERS substrate and experimental setup 44

Figure 2.3 Experimental glassware for EC-SMSERS experiment. 46

Figure 2.4 Demonstration of well-behaved, reversible electrochemistry for R6G in solution. 49

Figure 2.5 Electrochemical demonstration of uncompensated solution resistance and the presence of a surface-bound electroactive species. 50

Figure 2.6 EC-SERS of R6G at many-molecule coverage. 51

Figure 2.7 Representative SMSERS spectra of R6G. 53

Figure 2.8 SMSERS validation and EC-SMSERS Signal Loss Histogram. 55

Figure 2.9 EC-SMSERS in the underpotential region. 58

Figure 2.10 Representative SMSERS spectra displaying a blue shift in the 1350 cm^{-1} mode of R6G as a function of increasingly negative potential. 59

Figure 2.11 R6G vibrational mode positions versus applied potential. 61

Figure 3.1 EDC Crosslinking Reaction Schematic. 67

Figure 3.2 Experimental glassware used for electrochemical resonance Raman spectroscopy (EC-RRS) experiment. 69

Figure 3.3 Comparison of experimental and theoretical R6G· and R6G$^+$ Raman spectra. 75

Figure 3.4 Selected eigenvector diagrams for R6G·. 77

Figure 3.5 Selected eigenvector diagrams for R6G$^+$. 78

Figure 3.6 Molecular structures of R6G and R6G-amine. 80

Figure 3.7 Cyclic voltammetry of EDC-crosslinked R6G on AgNPs on ITO. 81

Figure 3.8 SERS of R6G-amine$^+$ using a heterogeneous EDC crosslinking procedure. 84

Figure 3.9 Representative SERS spectra from heterogeneous EDC coupling of R6G-amine$^+$ on an AgFON. 85

Figure 3.10 Schematic (not to scale) of homogeneous EDC-crosslinking of R6G performed on AgNPs in solution. 87

Figure 3.11 Representative SERS spectra of R6G-amine$^+$ homogeneously EDC-crosslinked on AgNPs. 88

Figure 3.12 EC-SERS of R6G-amine$^+$ homogeneously EDC-crosslinked onto AgNPs. 89

Figure 3.13 Representative SERS spectrum of R6G-amine· with 405 nm excitation. 90

Figure 4.1 Experimental schematic for EC-SERS measurements. 98

Figure 4.2 NRS of gentamicin in MQ H_2O at various concentrations. 100

Figure 4.3 Comparison of the full-width half-maximum (FWHM) of the 801.3 cm^{-1} mode of cyclohexane on a standard macro Raman instrument (LS785) and the CBEx™ handheld Raman spectrometer. 101

Figure 4.4 NRS of neat propofol.......... 102

Figure 4.5 Linear NRS calibration curves for gentamicin using integrated peak intensity. 103

Figure 4.6 Linear NRS calibration curves for gentamicin using integrated peak area. 104

Figure 4.7 Electrochemical behavior of dobutamine. 108

Figure 4.8 AuFON substrates used for EC-SERS. 109

Figure 4.9 EC-SERS of dobutamine. 110

Figure 4.10 Dobutamine EC-SERS 1605 cm^{-1} mode integrated peak intensity as a function of applied potential. 111

Figure 4.11 Accuracy determination of EC-SERS of dobutamine. 112

Figure 4.12 Limit of Detection determination for dobutamine.......... 113

Figure 4.13 Photographs of the commercializable EC-SERS chip.......... 114

Figure 4.14 EC-SERS of 4 mg/mL dobutamine on AuFON chip device taken with CBex™ spectrometer. 114

Figure 5.1 SORS Instrumental Setup. 120

Figure 5.3 SORS of atherosclerotic plaques 121

Figure 5.4 SORS of additional atherosclerotic plaques. 123

Figure 5.5 SORS of atherosclerotic plaque with surrounding fatty tissue. 124

List of Tables

Table 3.1 R6G· RRS, R6G$^+$ and R6G-amine SERS peak positions for experimentally calculated (Exp.) and theoretically predicted (Theor.) spectra. 76

Table 3.2 Sample preparation conditions under study for homogeneous EDC crosslinking reaction. 86

Table 4.1 Calculated mean peak intensities, standard deviation and 95% confidence intervals for the 980 cm^{-1} mode of gentamicin as measured with the macro Raman instrument. 105

Table 4.2 Calculated mean peak intensities, standard deviation and 95% confidence intervals for the 980 cm^{-1} mode of gentamicin as measured with the CBEx™ handheld Raman spectrometer. 106

Chapter 1. Introduction

1.1. Motivation

Since its experimental realization, SERS has presented itself as a powerful molecular sensing technique, with the potential to detect and study single molecules. It is with this sensitivity that chemical reactions or mechanisms can be studied at their lowest fundamental limits. In particular, electron transfer reactions are crucial to study because they lie at the heart of numerous fundamental processes: electrocatalysis, solar energy conversion, energy storage in batteries, and biological events such as photosynthesis. While electrochemical reactions are commonly monitored and described on a macroscopic scale, observing billions of electrochemical events per second, the ability to examine electrochemistry at the nanoscale would unravel details that would otherwise be obscured in a bulk measurement. The use of optical spectroscopy to elucidate nanoscale electrochemical behavior is an attractive alternative to traditional amperometric techniques like scanning electrochemical microscopy (SECM). SERS, in particular, shows great promise for exploring electrochemistry at the nanoscale due to its high chemical specificity and sensitivity. The first half of this thesis will highlight progress in monitoring single electron transfer reactions with SMSERS and its implications for nanoscale electrochemistry.

The excellent chemical sensitivity of SERS originates from high E field enhancements from noble metallic nanostructured substrates, which can yield Raman enhancements up to 10^{10}. SERS has been applied to many sensing problems, including those in catalysis, biosensing, and art conservation because of this high enhancement. While SERS is a highly sensitive, molecule-general technique, not all molecules will strongly bind to noble metal, SERS-active surfaces; this limitation restricts many SERS sensing applications to the use of a SERS-active surface decorated with a capture layer that will bind the analyte of interest. Understanding how molecules bind to and react on SERS-active surfaces will further the optimization of SERS-active surfaces for molecular sensing. Additionally, using the highest enhancing SERS substrates will push the routine sensitivity limit of SERS towards the single-molecule limit and further validate it as a sensing technique. The second half of this thesis will explore using EC-SERS, a label-free SERS methodology, to detect analytes used in intravenous drug therapies.

1.2. Surface-enhanced Raman Spectroscopy

1.2.1. Origin of SERS and SERS Enhancement Mechanisms

SERS has established itself as a powerful tool for molecular sensing, with the potential to detect and study single molecules, thanks to the ability of noble metallic nanoparticles to enhance otherwise weak Raman scattering by orders of magnitude. The phenomenon of SERS was first observed in 1974 by Fleischmann[1] and later described in 1977 by Jeanmaire and Van Duyne,[2] where they sought to explain the origins of a million-fold Raman signal amplification of pyridine adsorbed onto a roughened Ag electrode. Indeed, they had understood that the Raman signal amplification could not have originated from the increased number of pyridine molecules adsorbed onto a roughened Ag electrode surface, but to a physical surface enhancement mechanism. It is now widely accepted that Raman enhancement has two mechanisms, the chemical (CE) enhancement and electromagnetic (EM) enhancement mechanisms, as dictated by fundamental equation of Raman scattering (Equation 1.1):

$$\vec{\mu}_{induced} = \alpha \vec{\mathrm{E}} \qquad \text{(Equation 1.1)}$$

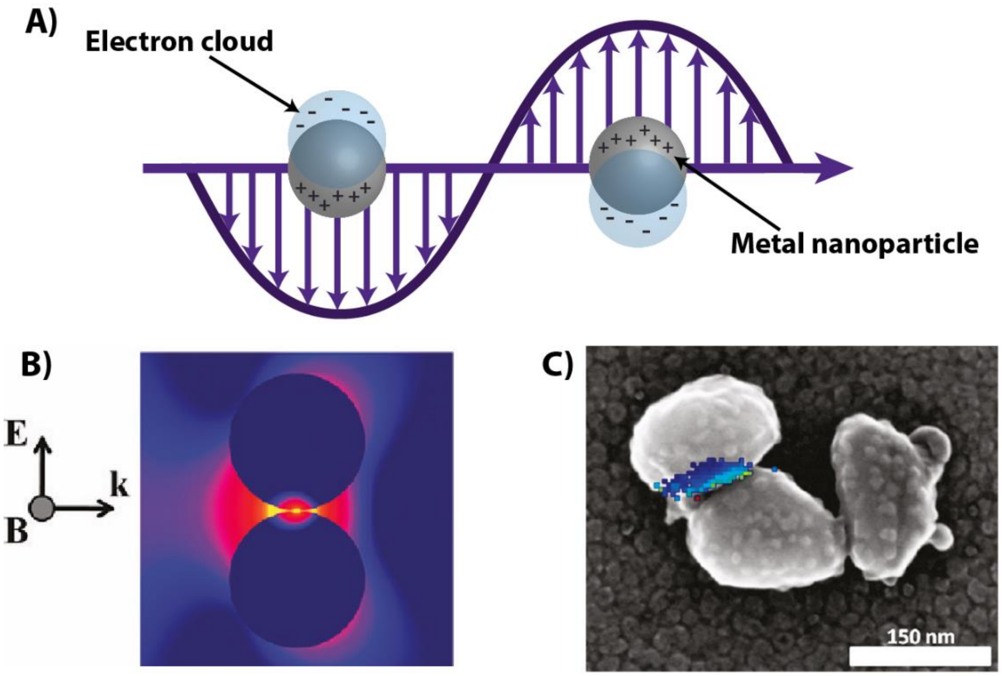

Figure 1.1 Physical origins of SERS. (A) Schematic of the electromagnetic enhancement mechanism of SERS (B) Illustration of a hotspot at the junction of a dimer aggregate of gold particles. FDTD calculations of the $|E|^2/|E_0|^2$ contour profiles show local field enhancements in the gap between the two 100 nm particles, where the areas of highest enhancement are located in the gap. (C) Overlay of R6G SERS signal intensity spatial map and SEM image of the Ag colloidal trimer data from which the SERS data was collected. B and C reprinted with permission from References 4 and 65. Copyright 2011-2012 American Chemical Society.

where the $\mu_{induced}$ is the induced dipole of the molecule, α is the molecule's polarizability tensor and E is the electric field. Enhancement from the chemical mechanism occurs by enhancing α through excitation of adsorbate-surface charge transfer resonances; recent theoretical studies predict maximum chemical enhancements with highly polar substituted adsorbates to be on the order of 10^2.[3] It is the electromagnetic (EM) enhancement that contributes the majority of the Raman enhancement, typically on the order of 10^4-10^8. Both the incoming excitation source and scattered Raman photons are enhanced by E^2, yielding a total E field enhancement of E^4.[4] (**Figure 1.1**B) The EM enhancement originates from a phenomenon known as the localized surface plasmon resonance (LSPR). An LSPR is generated by irradiating a metallic nanoparticle that is significantly smaller than the incident wavelength of light, which in turn induces a coherent oscillation of the metal's free conduction electrons relative to the metal nuclei (Figure 1.1A).[5] Au and Ag nanoparticles have the strongest LSPRs in the visible range due to their dielectric properties. The LSPR is also highly sensitive to nanoparticle shape, size, local refractive index and nanoparticle material.

1.2.2. SERS substrates, "Hot spots" and Enhancement Factors

As shown in **Figure 1.1**B, there is a spatial distribution of E field strength about the particle. The junction between two nanoparticles, or "hot spot" have high E fields which lead to upper limits of reported EFs and allow SERS to reach the single molecule detection limit. A wide variety of SERS substrates have been fabricated to yield a high density of SERS hot spots and therefore high SERS enhancements. The majority of SERS substrates either fall under the category of nanoparticle assemblies or flat lithographic substrates.[6] For the purpose of this thesis, the discussion of SERS substrates will focus on Ag colloidal nanoparticles and metal film over nanospheres (MFONs); representative SEM images of each substrate are shown in Figure 1.1C and Figure 1.2B, respectively. Ag colloids are commonly synthesized using the Lee and Miesel method, which is a simple reduction of silver nitrate in the presence of citrate under boiling conditions; this reaction produces quasi-spherical Ag nanoparticles (AgNPs) that are typically 40-80 nm in diameter.[7] One benefit of using aggregated Ag colloids is the high density of hot spots; theoretical and experimental work shows that hot spots yield SERS enhancements up to 10^{10} due to extremely high E fields at the junction of two nanoparticles (**Figure 1.1**). Despite their high enhancements, Ag colloids are generally irreproducible in size, shape and aggregate formation.[8]

An alternative to Ag colloids are lithographic MFON substrates, pioneered by the Van Duyne group.[9,10] MFON substrates are relatively low-cost and simple to fabricate; a schematic of the

MFON fabrication procedure is highlighted in Figure 1.2A. First, a layer of silica microspheres is dropcast on a cleaned silicon wafer, evenly distributed on the surface and allowed to dry; the spheres dry in a hexagonal close packed array. Next, a relatively thick (150-200 nm) layer of plasmonic metal, typically Ag or Au, is then deposited directly on the sphere surface. The metal deposition on the microspheres yields a high density of rough, nanoscale features that lead to high SERS enhancements across the entire area of the substrate (Figure 1.2B-C). In addition, the LSPR of MFONs is readily tunable by changing the diameter of microspheres used or the type of metal and amount deposited.[11] MFONs can also be implemented as a working electrode for electrochemical SERS (EC-SERS) measurements because the metal is also deposited between and

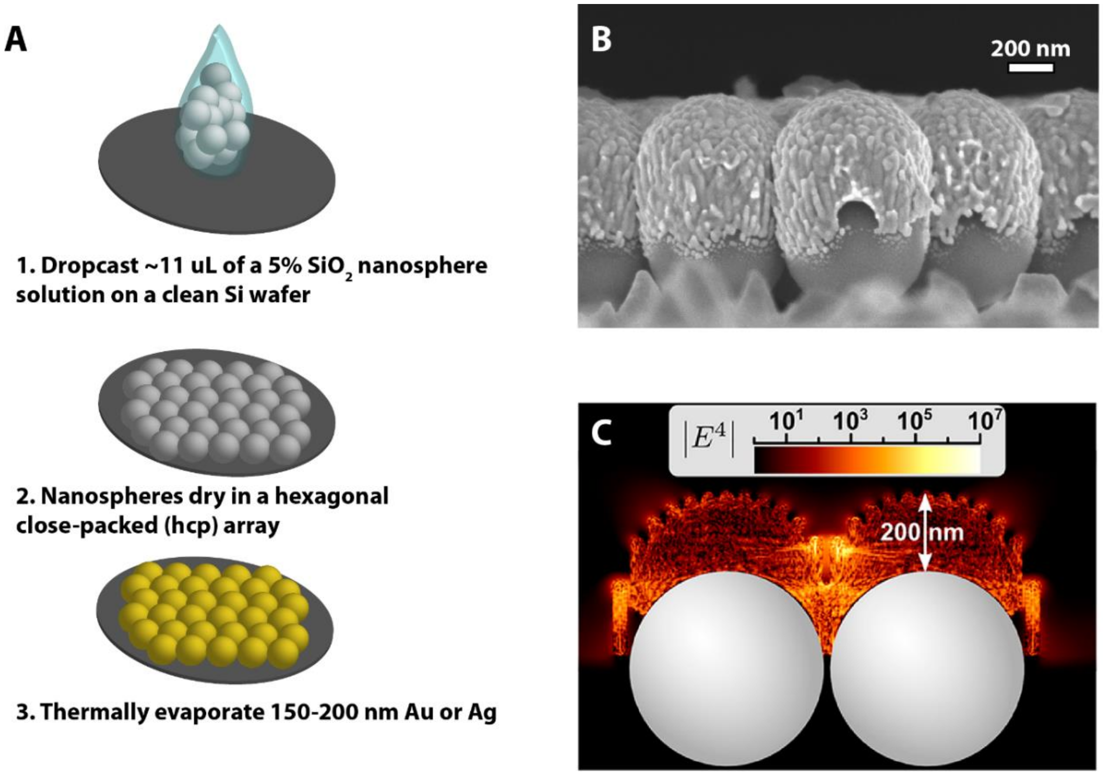

Figure 1.2 Film over nanosphere SERS substrates. (A) Schematic of the preparation of FON substrates. (B) Representative SEM image of 200 nm Ag deposited on 600 nm silica microspheres. (C) Theoretical predictions, using DDA calculations, of enhancements of electric field enhancement for a dimer of silica microspheres coated with 200 nm of Ag. B and C adapted from Reference 11. Copyright 2013 American Chemical Society

underneath the microspheres.[12] Using MFONs for EC-SERS will be discussed in detail in Chapter 4.

A standard metric used to quantitate the enhancing ability of a SERS substrate, and ultimately its sensing capability, is the analytical enhancement factor (EF) (Equation 1.2):

$$EF = \frac{I_{SERS}/N_{surf}}{I_{NRS}/N_{vol}} \qquad \text{(Equation 1.2)}$$

where I_{SERS} is the integrated peak intensity of a Raman mode, normalized by the number of molecules on the surface, N_{surf}. This is divided by the I_{NRS}, or the intensity of the normal Raman mode, normalized by the number of molecules within the laser spot volume, or N_{vol}. Calculating EFs for SERS substrates allows one to take into account experimental factors such as laser power, spot size, number of molecules probed, size of nanostructures, etc. EFs for Ag colloids have been reported to range between 10^6-10^{10}, and EFs for MFONs have a much wider spectrum of EF values, ranging from 10^3-10^{11}.[6,13] Such high enhancements and the ability to use a wide variety of substrates yield SERS as a powerful sensing tool; since its inception, SERS has been applied to a large spectrum of problems including analysis of single molecules,[14] identification of trace dyestuffs in artworks,[15] chemical warfare agent detection,[16,17] and monitoring catalytic reactions.[18] In particular, Chapter 4 will highlight recent progress in SERS detection of clinically relevant analytes for intravenous drug therapies.

1.3. Single-Molecule SERS (SMSERS)

1.3.1. Beginnings of SMSERS: First Demonstrations and Development of SMSERS Proofs

The first two demonstrations of SMSERS occurred in 1997 from the Nie and Kneipp groups. Kneipp et al. used 834 nm laser excitation with crystal violet (CV) dye on citrate-reduced colloidal Ag nanoparticle aggregates in solutions.[19] They found that the SERS signal intensity was quantized, which they then fit to a Poisson distribution of 0-3 molecules within the laser focal volume and estimated an average of 0.6 molecules within the laser focal volume. Nie and Emory used rhodamine 6G (R6G) dye (Figure 1.3A) on an Ag nanoparticle substrate with a 514.5 nm laser excitation wavelength. They justified SM detection by observed signal intensity fluctuations in SMSERS spectra, which they attributed to single molecules diffusing in and out of an Ag nanoparticle aggregate hot spot.[20] Both groups reported 10^{14} enhancements relative to the normal Raman signal.

While this work regenerated an interest in SERS, both initial proofs of SMSERS were eventually disproven: first, the intensity fluctuation argument is not a sufficient proof for observing single molecules with SMSERS because signal "blinking" was found to occur with and without a SERS-active probe on the substrate.[21] Secondly, Etchegoin et al. demonstrated the observed Poisson distribution by Kneipp et al. was an artifact of limited sampling number (< 100 events).[22] Work by the Etchegoin and Le Ru groups demonstrated an alternative, more statistically rigorous approach where one implements two distinct adsorbates (e.g. R6G and benzotriazole) at sufficiently low adsorbate coverage and detects the SMSERS signal from one or the other.[23] This was coined the bianalyte approach, and is the most widely accepted SMSERS proof to date.

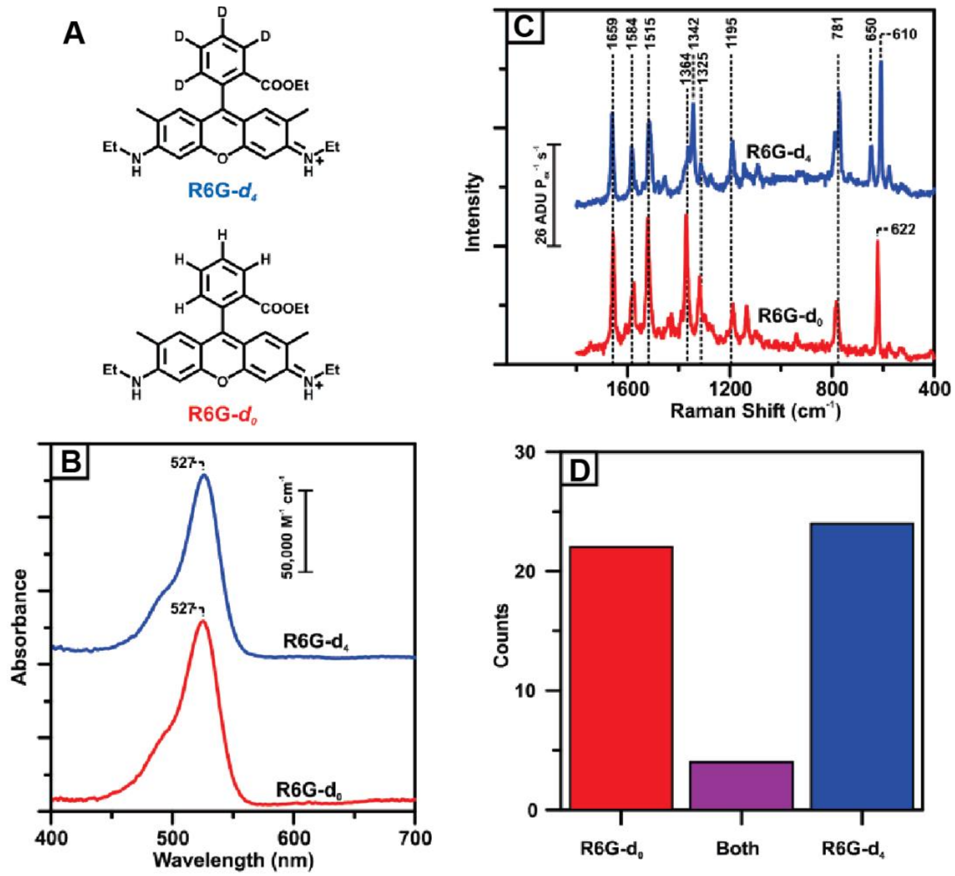

Figure 1.3 Frequency domain proof of SMSERS. (a) Chemical structures of R6G-*d4* and R6G-*d0*. (b) Visual absorbance spectra of R6G isotopologues, demonstrating no significant change in electronic properties upon deuteration. (c) Representative SMSERS spectra of R6G-*d4* and R6G-*d0*. Spectra were collected under an N_2 flow environment. Acquisition parameters: λ_{ex} = 532 nm, P_{ex} = 2.4 W/cm^2 (grazing incidence) t_{acq} = 10 s. (d) Collected SMSERS histogram of total R6G-*d0*, both isotopologues and R6G-*d4* spectra observed. Figure adapted from Reference 25. Copyright 2007 American Chemical Society.

Despite its utility, the bianalyte approach can be plagued with challenges such as differences in molecular cross section and binding affinity for the SERS substrate; one must carefully take these factors into account when conducting SMSERS experiments.[24]

An improvement of the bianalyte approach, coined the isotopologue or frequency domain approach, was first established by Dieringer et al.[25] The isotopologue approach uses two isotopic analogs, like R6G-*d0* and R6G-*d4*, to validate SMSERS. The benefit of this approach is the minimal difference in molecular cross section and substrate binding between the two molecules (**Figure 1.3**A-B). As shown in Figure 1.3C, the SMSERS spectra are unique to each isotopologue. In an SMSERS experiment, a frequency histogram of either R6G-d_0, both, or R6G-d_4 events is counted (**Figure 1.3**D) and fit to a binomial Poisson distribution (Equation 1.3):

$$P(n_4, n_0, \alpha) = \frac{e^{-\alpha}\alpha^{n_4+n_0}}{(n_4+n_0)!} x \frac{(n_4+n_0)!}{n_4 n_0!}\left(\frac{1}{2}\right)^{(n_4+n_0)} = \frac{e^{-\alpha}}{(n_4+n_0)!}\left(\frac{\alpha}{2}\right)^{(n_4+n_0)} \qquad \text{(Equation 1.3)}$$

where n_4 and n_0 are the number of R6G-d_4 and R6G-d_0 molecules in a given SMSERS spectrum, respectively, and α is the approximate number of molecules per nanoparticle. Assuming $\alpha = 1$ at sufficiently low R6G concentration,[7] the probability of R6G-d_0:both:R6G-d_4 should be 2.5:1:2.5; experimental results typically have higher ratios due to observation of less both events.[8,10,24-26]

After the establishment of a statistically valid SMSERS proof, a great amount of work was done and is still being done to understand the fundamental properties of SMSERS. However, for purpose of this thesis, the following sections will highlight recent progress of applying SMSERS to monitor chemical reactions.

1.3.2. Using SMSERS to Monitor Chemical Reactions

SMSERS is a powerful tool to use to monitor chemical reactions due to its high sensitivity. In particular, SERS has been recently applied to studying heterogeneous catalytic reactions because SERS-active nanoparticles can serve both as the catalyst material and Raman-enhancing substrate.[18] Many studies have focused on examining the model dimerization reaction of *para*-nitrothiophenol (p-NTP) or *para*-aminothiophenol (p-ATP) to 4,4-dimercaptoazobenzene (DMAB) with SERS.[18,27-35] Recently, efforts have pushed towards studying DMAB formation reaction at the single molecule limit. The Deckert group explored the effect of p-NTP coverage on AuNPs and how this effects the DMAB formation yield. Furthermore, they examine the fate of a single p-NTP molecule if it cannot react with another molecule and dimerize to form DMAB. [27] Below 5 x 10^{-8} M, the coverage of p-NTP is too sparse and there is no apparent DMAB formation on the AuNP surface; the authors therefore assume that there are 1-2 distinct molecules in the AuNP hot spot junction. As illustrated in **Figure 1.4**, upon sample illumination, there is the appearance of new vibrational modes which indicates the cleavage of the nitro group of p-NTP to

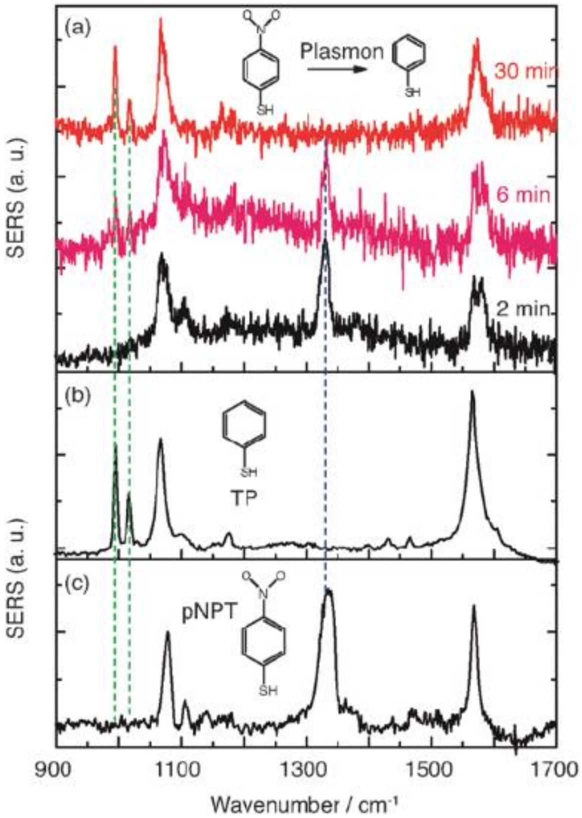

Figure 1.4 Photocatalytic conversion of *para*-nitrothiophenol to thiophenol on AuNPs. (a) Time-dependent SERS spectra of reacting 10^{-9} M pNTP on AuNPs with P_{ex} = 3 mW after 2 (black trace), 6 (pink trace) and 30 (red trace) minutes. Over time, two peaks associated with TP appear and the major peak of pNTP disappears. (b) and (c) high coverage SERS spectra of TP and pNTP, respectively. Reproduced from Ref. 27 with permission from the Royal Society of Chemistry.

form thiophenol (TP). The authors rationalize the formation of TP via plasmon induced hot electron generation, providing sufficient activation energy to cleave the nitro group from the p-NTP molecule. This work demonstrates the power of monitoring single molecule reactions on a plasmonic nanoparticle surface using SERS. In a separate study, Choi et al. demonstrate the heterogeneity of reactivity of single pairs of p-NTP molecules dimerizing to DMAB, which they attribute to the relative location of the p-NTP molecules within the hot spot junction.[28] They demonstrate "hot" and "mild" photoswitching regimes, as defined by two unique types of temporal fluctuations in the DMAB signal, illustrating the importance of how the location of a molecule within nanoparticle hot spot structure effects chemical reactivity.

SERS can not only potentially measure temperature or catalytic reactions, but can also observe transient intermediates, such as the rare cis-tautomer of porphycene as studied by Gawinkowski and coworkers.[36] SMSERS detection of porphycene was proven using the isotopologue method. It is interesting to note that in each SMSERS histogram collected, more porphycene-d_0 counts were measured than porphycene-d_{12}, indicating that the d_0 had a higher surface diffusion coefficient for the nanoparticle surface. This result highlights the importance of taking into account the subtle differences in molecular properties (e.g. molecular cross section, binding affinity) when conducting a statistically valid SMSERS proof.[24] Overall, this study demonstrates the ability to observe transient species, in this case the rare cis tautomeric form of porphycene, with SMSERS as well as the potential for studying similar molecules such as substituted porphycenes and porphyrins with SMSERS.

SMSERS can also monitor host-guest interactions, as demonstrated by Sigle and coworkers.[37] They implement curcubit[7]uril (CB[7]) as a means of detecting single molecules within a Au

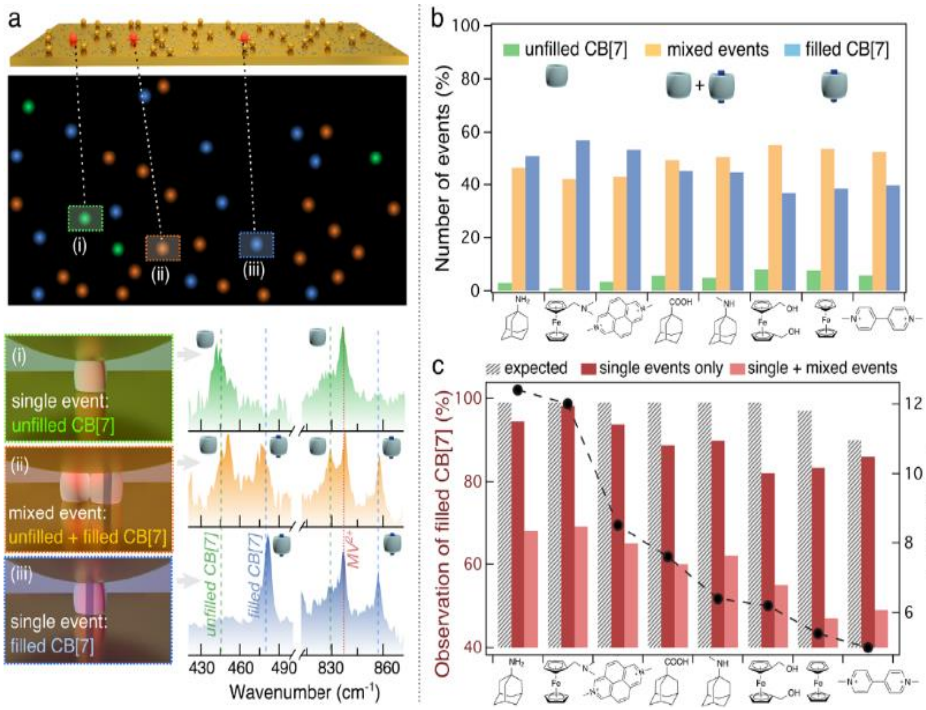

Figure 1.5 SMSERS detection of curcubit[7]uril host-guest complex. (a) (top) Schematic of distribution of CB[7] and MV^{2+}·CB[7] mixture in the NPoM probes showing three observable events. (bottom) Representative SERS spectra of the CB[7] Raman modes (CB[7]: gray dashed lines and MV2+: red dotted lines). Each spectra corresponds to (i) NPoM with purely unfilled CB[7] (green), (ii) a mix of filled and unfilled CB[7] (orange), and (iii) only filled CB[7] (blue). (b) Statistical representation of the number of events observed, where 300−400 NPoMs had sufficient SERS signals. (c) Comparison of the number of times signals from filled CB[7] is observed for SM events only and mixed events as a function of binding affinities of guests for CB[7] versus binding strengths of the guest molecules (black trace). Reproduced with permission from Reference 37. Copyright 2015 American Chemical Society.

nanoparticle on Au mirror (NPoM) junction. Curcubit[n]urils (CB[n]s) are macrocyclic molecules with a barrel-like structure consisting of a glycouril monomer unit where [n] is the total number of monomers in the CB[n] molecule.[38] CB[n]s are ideal for sensing applications because a single molecule binds in the CB[n] cavity volume and the CB[n] subsequently undergoes structural changes when a guest molecule enters the CB[n] cavity, which is readily detectable using Raman spectroscopy.[39] Bianalyte SERS spectra of either the empty CB[7] or filled CB[7] with 8 different molecules (methyl viologen (MV), adamantane or ferrocene derivatives) were acquired. (**Figure 1.5**) Despite the clear distinction between empty and filled CB[7] used to prove bianalyte SERS detection, nearly half of complex binding events detected were both filled and unfilled CB[7] for all guest molecules studied, indicating the presence of at least one CB[7] molecule in the Au mirror-nanoparticle junction. While the molecular coverage of the SERS-active substrate needs to be optimized in order to rigorously demonstrate SMSERS, this work is a promising step forward towards using SMSERS to probe biologically relevant molecules including drug molecules, cellular metabolites (e.g. pyruvate and lactate)[40], proteins and DNA.

1.4. Investigating Nanoscale Electrochemistry with Surface-Enhanced Raman Spectroscopy

1.4.1. Introduction

Electrochemical reactions are typically monitored and described on the ensemble level, taking into account many surface site conditions and molecule-molecule interactions. However, electrochemical reactions occurring at different surface sites will have a different formal potential, E^0, and heterogeneous rate constant, k^0 (Figure 1.6); these single-site characteristics are masked in bulk measurements. Therefore, it is necessary to look to single-molecule, single-site nanoelectrochemistry in order to understand how nanoscale surface features and molecular orientation affects fundamental electrochemical properties.

Electrochemical single molecule detection was first achieved using scanning electrochemical microscopy (SECM).[41-43] While other electrochemical methods such as lithographic nanogap electrodes[44] and nanopipettes[45] have been implemented to study nanoelectrochemistry, there has been a recent burst of interest in investigating nanoelectrochemistry with optical spectroscopy.[46-48] The appearance or disappearance of an optical signal from a molecule during an electrochemical reaction requires a molecular system in which either the reduced or oxidized form is optically active. Using optical spectroscopy to study nanoelectrochemistry is advantageous over redox cycling amperometric techniques in that single-molecule detection is readily attainable and the signal does not need amplification. Detecting single-molecule and single-nanoparticle electrochemical events via optical spectroscopy has been achieved through fluorescence microscopy,[49-54] electrogenerated chemiluminescence (ECL)[55-57] and single-molecule SERS (SMSERS)[58-63].

SERS is an ideal method to study nanoelectrochemistry because it provides chemical information and, during the reaction, structural changes of a molecule in close proximity to a nanostructured metallic surface can be monitored. As discussed previously, SMSERS is now an

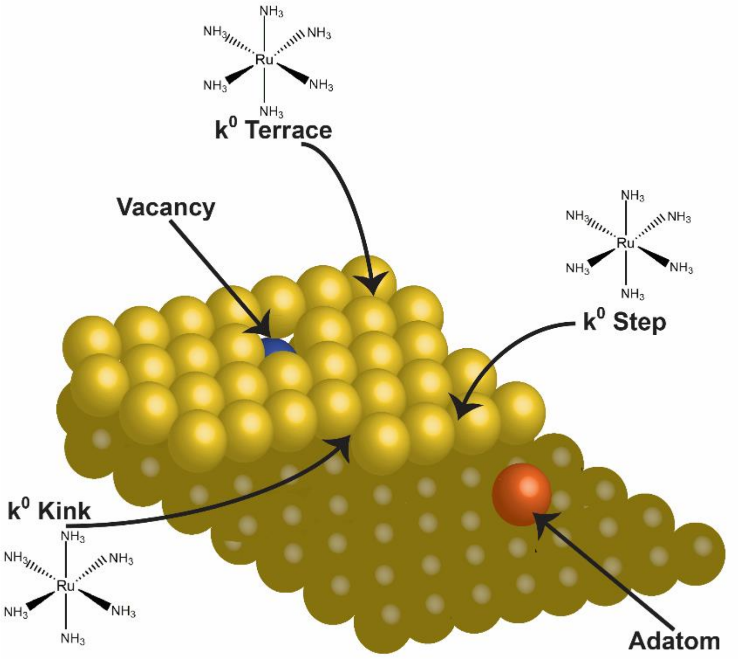

Figure 1.6 Surface-dependent nanoscale electrochemistry. Schematic illustration of an Au(111) surface with various surface site features. The electrochemical reduction of ruthenium hexaamine will have a different formal potential (E^0) and heterogeneous rate constant (k^0) depending on the surface site at which it reacts.

established technique for studying single molecule reactivity, and was first used to study electrochemistry in 2010 by Cortés et al.[58] Later work demonstrated that electrochemical SMSERS (EC-SMSERS) can provide insight into nanoscale potential-dependent charge transfer dynamics[59] and the heterogeneity in redox potentials of Nile Blue (NB) on Ag nanoparticles.[58,60] More recently, the Van Duyne group investigated single-electron transfer with EC-SMSERS and the Willets group has implemented super-localization SERS imaging to understand site-specific nanoelectrochemistry with 5-10 nm spatial precision, as will be described in this Chapter.[61-63]

The implementation of EC-SERS provides the ability to monitor molecular behavior on the nanoscale in parallel with fundamental electrochemical properties (e.g. E^0 and k^0). In this section, recent progress in the field, focusing on EC-SMSERS and super-localization SMSERS imaging, will be discussed. We then describe substrates and molecular systems of interest in order to gain maximum insight from these experiments.

1.4.2. Current Progress in EC-SMSERS

1.4.2.1. Observing Single-Electron Transfer with EC-SMSERS

The ability of EC-SMSERS to monitor single electrochemical events provides insight into the site-specific, heterogeneous electrochemical behavior at the nanoscale. Recently, the Van Duyne group implemented EC-SMSERS to study single electron reduction events of the dye molecule Rhodamine-6G (R6G).[63] This work will be discussed in detail in Chapter 2. Because single electron transfer can be altered by the presence of water and oxygen, a custom spectroelectrochemical cell was designed for dry solvent transfer under vacuum and measurements in a non-aqueous environment.

SMSERS events were validated by the isotopologue proof,[25] where a sufficiently low concentration of an equimolar mixture of non-deuterated and deuterated forms of R6G are physisorbed on Ag nanoparticles. R6G isotopologues have the same electronic properties and binding affinities but unique SERS spectra; the statistical distribution of recorded SMSERS spectra follows a binomial Poisson distribution. The spectroelectrochemistry of single R6G molecules was observed by stepping the potential of the indium tin oxide (ITO) working electrode, functionalized with SERS-active Ag nanoparticles, from 0 V to -1.2 V in -0.1 V steps. A SMSERS signal loss event indicated the reduction of R6G. However, most signal loss events did not have a signal return, indicative of electrochemical desorption of the R6G neutral radical species. Strategies to avoid desorptive losses include covalent linking of redox active molecules to the AgNP surface, which will be introduced in Section 1.4.3.2 and in detail in Chapter 3. Experimentally, the SMSERS signal loss event frequency histogram as a function of applied potential was broader than the surface CV of R6G adsorbed on Ag, demonstrating relative underpotential reduction events. These events were hypothesized to originate from variations in the reduction potential of the Ag nanoparticle-adsorbed R6G binding site, as well as heterogeneity of the local environment around the R6G molecule. Observing single electron transfer with EC-SMSERS strongly demonstrates the electrochemical heterogeneity of nanoparticles and highlights the importance site-specific electrochemical activity on surfaces.

1.4.2.2. Super Localization EC-SMSERS Imaging

Spatially resolving the location of a single molecule on a nanoparticle would aid in understanding the coupling between a single molecule and the optical fields of a nanoparticle, and how the location and density of nanoparticle hot spots affects the overall optical response of the molecule. However, obtaining nanometer scale spatial resolution from optical spectroscopies like SERS is restricted by the diffraction limit, or approximately half of the emission wavelength (~250

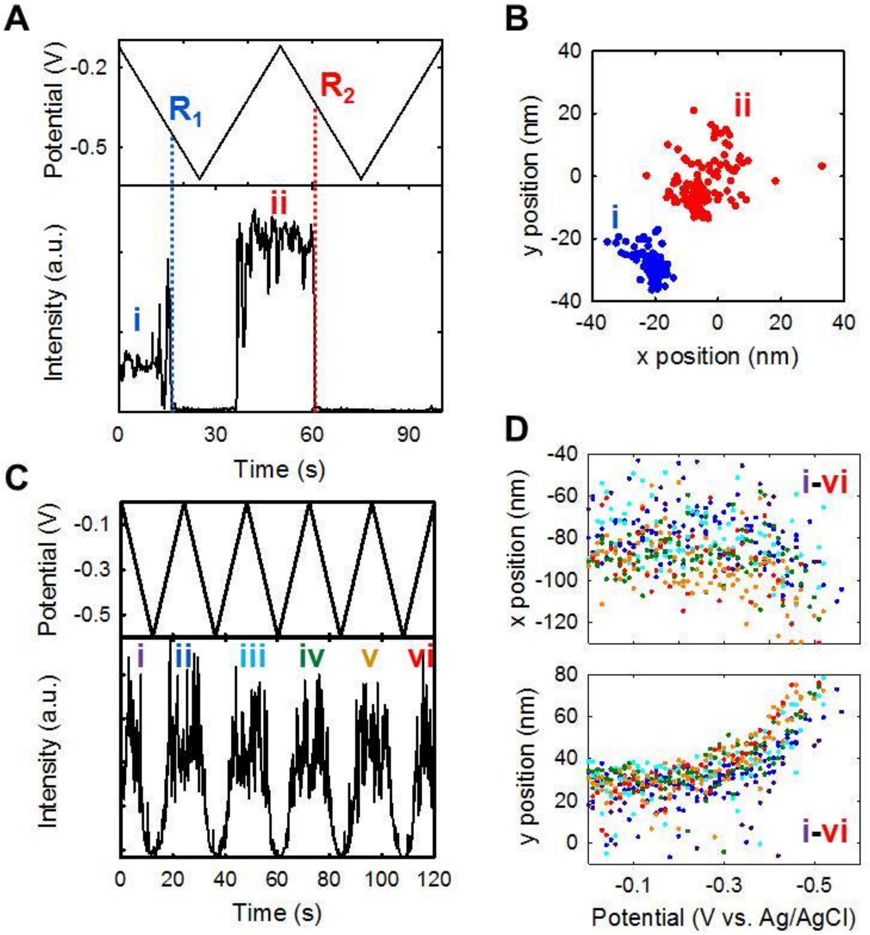

Figure 1.7 Electrochemical super-localization SMSERS imaging of Nile Blue. (A) Single-molecule and (C) few-molecule integrated SERS intensity trajectories modulated by electrochemical reduction and oxidation waveforms, as shown. (B) Localized SERS emission corresponding to the two emission events in (A). (D) Localized SERS emission voltammograms corresponding to the emission events in (B). Adapted with permission from Reference 61. Copyright 2014 American Chemical Society.

nm with 532 nm excitation). One means of overcoming the diffraction limit and therefore achieving sub-250 nm resolution is to fit the diffraction-limited emission from a single emitter, such as a noble metal nanoparticle (NP) aggregate labeled with a SERS-active probe, in order to localize the emitter with sub-10 nm precision. Stranahan and Willets first combined principles of super-resolution fluorescence microscopy[64] with SERS, coined super-localization SERS[65,66], where they imaged the spatial profile of R6G SMSERS signal on single Ag colloidal NP aggregates with sub-15 nm spatial precision.[67] (Figure 1.1C) The position of the R6G SERS emission is determined by fitting the signal to a two-dimensional Gaussian point spread function (PSF) where the peak of the fit is defined as the centroid position.

Wilson and Willets recently applied SERS super-localization imaging to NB physisorbed onto Ag colloidal nanoparticle (NP) aggregates, to understand the site-specificity of nanoscale electrochemistry. The NB SERS intensity modulates off and on with reduction and oxidation.[61] The SERS intensity rises and falls in a single digital step upon oxidation and reduction, indicative of a single NB molecule on the nanoparticle electrode surface. The loss of SERS intensity caused by reduction during the two potential cycles occurs at distinct potentials (Figure 1.7A, R1 and R2), which correspond to unique positions of the molecule (Figure 1.7B, i and ii). This observation suggests that there is a spatial dependence associated with the potentials at which a molecule reacts on a nanoparticle electrode. While intriguing, these measurements are limited by small sampling of the electrode area, the limited number of potential cycles the molecule remains emissive, and the inability to discriminate between a reduction and photobleaching event.

Figure 1.7C shows the integrated SERS intensity from an AgNP aggregate labelled with multiple NB molecules in response to an applied potential. Here, the SERS intensity gradually rises and falls during oxidation and reduction, indicating few molecule coverage on the AgNP aggregate. Because of the higher NB coverage, when the diffraction-limited SERS emission is fit to a two-dimensional Gaussian, the calculated position represents an intensity-weighted superposition of all molecules in the oxidized state.[68] The spatial origin of the SERS emission reproducibility shifts as the potential is swept, suggesting that individual molecules are being oxidized or reduced at unique potentials based on their location on the electrode. (Figure 1.7D) This observation further supports the conclusion of site-specific redox potentials of molecules on AgNPs.

1.4.3. Redox-Active Molecules, Substrates and Substrate Functionalization for EC-SMSERS

1.4.3.1. Molecular Systems: Surface Adsorption, Redox and Optical Properties

Ideal molecular systems for directly monitoring nanoscale electrochemical processes using SERS must have both large Raman cross sections and well-characterized, robust electrochemistry. Additionally, the affinity of the molecular system to the electrode is of extreme importance, and we will discuss it in a later section. The most common class of molecules used to optically monitor electrochemical processes are redox dyes, such as NB and R6G, which have relatively simple electrochemistry, and strong resonance Raman cross sections. Several SERS studies in the past decade have exploited the well-characterized electrochemistry of NB using 633 nm excitation to monitor the disappearance of NB_{OX} signal upon reduction to the nonresonant NB_{RED} .[58,60-62,69,70]

Adapting EC-SERS to non-aqueous systems will greatly expand the list of candidate molecules for studying nanoelectrochemistry spectroscopically. As will be further elaborated in Chapter 2, recent work from the Van Duyne group has demonstrated the first non-aqueous EC-SMSERS study using R6G, a dye which undergoes a reversible 1-electron transfer in acetonitrile.[63] The most significant experimental challenge in monitoring single 1-electron transfer events is careful removal of oxygen and water from the system, which can alter the mechanism. For SERS measurements, a gas-tight cell was used to conduct single-molecule 1-electron transfer measurements and will be discussed further in Chapter 2.

Ultimately, EC-SERS will benefit from studying molecules with practical applications instead of model dye systems. Porphyrins, for example, have large resonance Raman cross sections adequate for single-molecule detection and have extensive applications in solar cells and conductive polymers.[71,72] Typically, charge transfer dynamics of porphyrins are studied using single-molecule fluorescence[52,53] but only SERS can give detailed structural information at the single-molecule level[36,59], highlighting the advantage over fluorescence to study nanoelectrochemistry.

1.4.3.2. Substrates and Substrate Functionalization

Substrates for EC-SERS require nanoscale features which support a localized surface plasmon resonance (LSPR) to enhance Raman signals. Lithographic nanohole and nanopore arrays are well-suited for EC-SERS due to their homogeneity, reproducible roughness, and trivial electrical contact. (**Figure 1.8**B-C)[73,74] Alternatively, periodic particle arrays prepared by nanosphere lithography (NSL) have a tunable LSPR, can be prepared on an optically transparent electrode (OTE) such as ITO and have highly enhancing triangular features that allow for SMSERS detection as shown in Figure 1.8A.[9] Colloidal AgNP and AuNP aggregates offer highly enhancing hot-spots that can be optically isolated, but aggregates are commonly polydisperse involving varied cores (dimer, trimers, tetramers, etc.) and suffer from large variations in size, shape, and

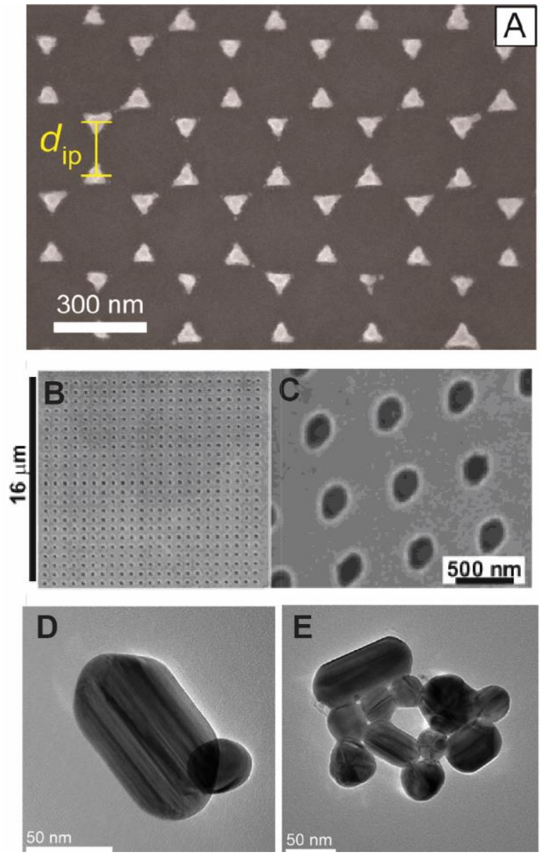

Figure 1.8 Representative EM images of SERS-active substrates that can be implemented for EC-SERS. (A) Representative SEM image of a periodic particle array (PPA), (B) and (C) Representative SEM images of a lithographic nanohole array. (D) and (E) Representative TEM images of aggregated Ag colloidal nanoparticles. Adapted from Refs. 8, 24 and 74. Copyright 2004,2011,2013 American Chemical Society.

surface structure and functionalization.[8,23,25] (**Figure 1.8**D-E) Shell-isolated nanoparticle enhanced Raman scattering has been applied to surface electrochemistry and could provide an alternative substrate in future nanoelectrochemistry experiments.[75]

Molecule immobilization is important to prevent desorption and diffusion of analyte molecules, which can limit the information obtained from EC-SERS experiments. Immobilization can provide a better survey of the entire electrode surface and enable targeted labeling. There are many strategies to attach optically-active redox molecules on substrates, including spontaneous physisorption, self-assembly of thiolated reporter molecules, and crosslinking reactions (e.g. EDC coupling or “click” chemistry). Each strategy has advantages and disadvantages, and requires careful characterization in order to properly interpret the nanoelectrochemistry.

Spontaneous adsorption of molecules onto nanoscale noble metals has been widely used from the discovery of SERS to the observation and application of SMSERS.[2,20,26,58,69] Major advantages of this labeling strategy are that a wide range of molecules can be used and the average number of adsorbates on a substrate can be controlled by changing the solution concentration. Limitations include preferential adsorption, diffusion on the electrode surface, and spontaneous desorption, all of which complicate the correlation of nanoscale electrochemical properties to optical signal changes. One strategy to overcome these shortcomings is to implement a thiol-containing redox probe, which can react with plasmonic metals to form a covalent sulfur-metal bond. For example, SERS- and redox-active viologens can be thiolated and subsequently self-assembled into a monolayer on gold electrodes[76] to detect three Raman-distinct redox states.[77] The electrochemistry of a monolayer of self-assembled molecules needs to be carefully characterized because intermolecular interactions and variable molecule-electrode distances can change the electrochemical behavior and resultant SERS signals.[78,79]

Alternatively, SERS-active molecules can be covalently bound to an electrode using a coupling reaction. One example is the well-known 1-ethyl-3-(3-dimethylaminopropyl)carbodiimide/N-hydroxysulfosuccinimide (EDC/NHS) pair, which can be used to couple a carboxylic acid terminated alkanethiol SAM with a primary amine to form an amide linkage.[62,80,81] Using EDC coupling to covalently tether R6G on AgNPs for EC-SERS experiments will be discussed in Chapter 3.

1.5. Conclusions and Thesis Overview

SERS is an extremely powerful tool for molecular sensing with the potential to detect single molecules. The sensitivity of SERS lies in noble metallic nanostructured substrates with “hot spots”, such as MONs or Ag colloidal nanoparticle aggregates, which yield Raman enhancements on the order of 10^4-10^{10}. Using the highest enhancing SERS substrates will push the routine sensitivity limit of SERS towards the single-molecule limit and further validate it as a sensing technique. Moreover, understanding how molecules bind to and react on SERS-active surfaces will contribute to both the understanding of chemical reactions on plasmonic nanoparticles and the optimization of SERS-active surfaces for molecular sensing. With these aims in mind, this thesis demonstrates the combination of electrochemistry and SMSERS for monitoring single molecule electron transfer reactions, as well as the use of Raman spectroscopy and EC-SERS for point-of-care sensing applications. Chapters 2 and 3 focus on using EC-SERS to study electrochemical reactions: Chapter 2 discusses the detection and study of single electron transfer events with SMSERS, and Chapter 3 explores SERS- and electrochemically-active sample preparation strategies to ultimately achieve the goal of monitoring two distinct redox states of a single-molecule electron transfer reaction with EC-SERS. Chapters 4 and 5 will discuss the use of Raman spectroscopic methodologies, including EC-SERS, for point-of-care applications: Chapter 4 highlights the use of normal Raman spectroscopy and EC-SERS to detect clinically relevant analytes used for intravenous drug therapies, and Chapter 5 illustrates the use of spatially offset Raman spectroscopy (SORS) to non-invasively detect atherosclerotic plaques.

Chapter 2. Observing Single, Heterogeneous, One-Electron Transfer Reactions with Single Molecule SERS

2.1. Introduction

The most fundamental event in electrochemistry is the chemically reversible, one-electron, heterogeneous electron transfer (HET) reaction. A HET reaction

$$O + 1e^{-} \underset{k_r}{\overset{k_f}{\rightleftarrows}} R \qquad \text{(Equation 2.1)}$$

involves the oxidized form of the analyte, O, being reduced to its reduced form, R. This reaction is characterized by its standard potential, E^0, and rate constant, k^0. To date, HET reactions have only been studied at the ensemble average level. Consequently, the measured E^0 and k^0 represent an average over many microscopic configurations of O and R and their interactions with the electrode surface.[26,58,61,69,82,83]

Electrochemical reactions play a central role in numerous fields such as electrocatalysis[84], energy storage[85,86], materials synthesis[87,88] and biological processes[50,89,90], averaging different local conditions i.e. molecule-molecule and molecule-substrate interactions, temperature, and transport properties among others. Single-molecule electrochemistry has been sought after for a long time in order to probe nanoscale local environments. The first demonstration of electrochemistry of a single molecule was reported by Fan and Bard in 1995 by trapping molecules between an insulated Pt/Ir scanning probe tip and an indium tin oxide (ITO) substrate; the bursts in current were attributed to redox of a single molecule moving in and out of the electrode-substrate gap.[41] There was a spike of interest in developing alternative methods to simultaneously detect single molecules and understand their electrochemistry.[44,46,48,91,92] To this end, optical techniques have been combined with electrochemical measurements in order to observe the change in a single molecule as a function of applied potential.[93] Some studies have combined fluorescence spectroscopy with electrochemistry by correlating the fluorescence intensity of a single molecule with applied potential.[49,55] Others used electrochemical scanning tunneling microscopy (EC-STM) to monitor the conformational changes of molecules on a surface as a function of applied potential.[94] Despite the great amount of information gathered from these studies, the techniques used cannot provide detailed chemical information about the changes in electroactive species as a function of applied potential.

Single-molecule SERS (SMSERS) is an ideal technique to investigate the electrochemistry of single molecules because it provides detailed chemical information about the molecular species in question. SMSERS was first claimed as strong intensity fluctuations in an ultra-low concentration of Raman-active reporters and with laser excitation on resonance with the electronic absorption of the analyte.[20] Since then, the intensity fluctuation argument for SMSERS has been disproven and groups have explored different single-molecule proofs. The two most commonly used and widely accepted proofs for SMSERS detection are: (i) The bianalyte method[95,96], and (ii) The frequency domain, or isotopologue, approach[25]. Both experimental approaches study the statistics of the relative intensities of two distinct molecules (bianalyte approach) or one molecule and its deuterated isotopologue (frequency domain approach) to infer the single-molecule nature of the SERS response. Further investigations focused on achieving: (i) SMSERS on various substrates, including colloids[8,58,67,96-101], lithographic substrates[10,102,103], and STM tips using TERS[26,104], (ii) non-resonant SMSERS[97] (iii) improved statistics, i.e. a large number of clearly demonstrated SMSERS events[22]. The fundamental aspects of SMSERS have been well-explored[68,98,99,105-107] and the next step in SMSERS research is to probe the chemical behavior of single molecules, such as monitoring the pressure-sensitive behavior of single R6G molecules.[108]

The first use of SMSERS to explore electrochemical events was reported by Cortés *et al.* in 2010. Using the bianalyte approach with dye molecules R6G and nile blue (NB), the authors demonstrated the feasibility of monitoring single-molecule electrochemistry of NB by SERS.[58] In later work, the authors extended the study to high resolution SMSERS spectra of NB by observing changes in the vibrational frequencies as a function of applied potential. The vibrational changes were attributed to reorientation of the NB molecule in the electrochemical double layer and molecular orientation relative to the nanoparticle surface.[60] Another SMSERS study combined

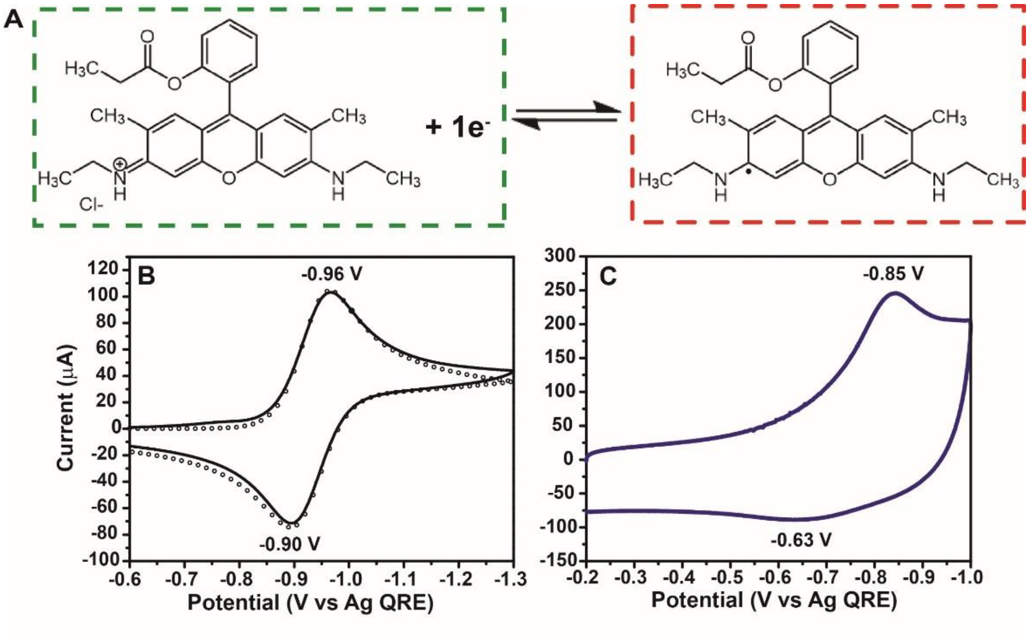

Figure 2.1 Electrochemical characterization of R6G. (A) Schematic of heterogeneous 1-electron transfer reaction for the reduction of Rhodamine-6G cation (green box) to its neutral radical product (red box). (B) 1 mM R6G solution phase CV on Ag working electrode (black trace) and fitted electrochemical simulation data (black circles) (C) Surface CV of high coverage R6G AgNPs on ITO.

with electrochemistry was reported by Wang *et al.* using ultra low concentrations of the hemin, an iron porphyrin molecule. In this work, the authors proposed that local thermal fluctuations govern the single electron transfer dynamics of hemin immobilized on Ag nanoparticles.[59] More recently, Willets *et al.* have demonstrated SMSERS and electrochemistry of NB with a super resolution microscopy approach, postulating that the NB molecules are sequentially reduced/oxidized on the nanoparticle surface.[61]

From our perspective, the aforementioned reports do not use the most rigorous proof of SM sensitivity; that is, the frequency domain or isotopologue approach[25], and is therefore our choice for this study. Herein, our primary goal is to understand the electrochemical behavior of R6G on the nanoscale as compared to a bulk electrochemical experiment. First, we characterize the 1-electron transfer electrochemistry of R6G both in solution and adsorbed on Ag surfaces at high concentration and coverage in a non-aqueous environment. Second, we demonstrate the first proof of non-aqueous, single-molecule electrochemistry optically monitored with the isotopologue approach of SMSERS. Last, we compare our distribution of EC-SMSERS-detected reduction events to the bulk and elaborate upon the origins of this behavior. We propose that the broadened distribution on the single molecule, single particle aggregate scale is primarily due to variations in the surface site or chemical potential of the Ag nanoparticle where the R6G is bound. We believe that this work, together with previously discussed works, demonstrate the power of SERS as a tool to optically monitor various classes of electrochemical reactions at the single molecule level.

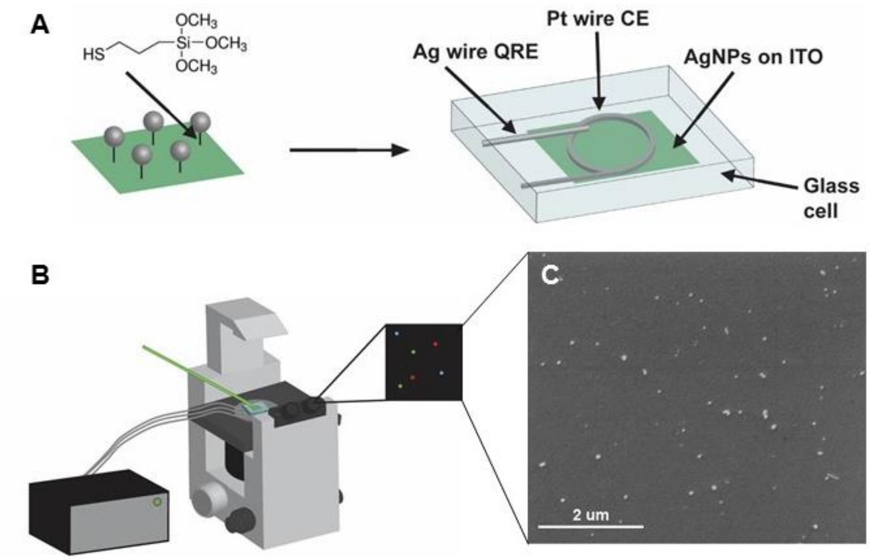

Figure 2.2 Preparation of EC-SMSERS substrate and experimental setup. (a) Schematic of AgNP functionalization on an ITO coverslip using MPS and an assembled spectroelectrochemistry glass cell with the functionalized ITO as a working electrode, an Ag wire as the quasi-reference electrode and a Pt wire as the counter electrode. (b) The assembled spectroscopy glass cell is attached to a potentiostat and then placed on a microscope stage. The laser excitation is focused onto the sample by grazing incidence at an angle of 60° relative to the surface normal. Single nanoparticle aggregates are selected by visually locating and centering a brightly scattering particle in the field of view. (c) Representative SEM image of an AgNP-functionalized ITO substrate at 20,000x magnification.

2.2. Experimental Details

Chemicals. Trisodium citrate dihydrate 90%, silver nitrate +99.99% ($AgNO_3$), sodium chloride +90% (NaCl), tetrabutylammonium perchlorate +99% (TBAP), hydrogen peroxide solution 30% (H_2O_2), ammonium hydroxide solution 28-30% (NH_4OH), (3-mercaptopropyl)trimethoxysilane (MPS) were purchased from Sigma-Aldrich and used without further purification. HPLC grade acetonitrile (≥99.5%) was purchased from Avantor Performance Materials and further purified prior to use by passing through a Pure Process Technology solvent drying system. Milli-Q water with a resistivity higher than 18.2 MΩ*cm was used in all preparations.

Deuterated R6G. The synthesis of R6G-d_4 are based on previous conditions given by Zhang *et al.*[109] and have been reported elsewhere.[25] Standard solutions of R6G-d_0 and R6G-d_4 in MQ H_2O were prepared and characterized with UV-Vis absorbance spectroscopy.

Bulk Electrochemistry. Bulk electrochemical measurements were performed in a capped scintillation vial. An Ag wire (0.25 mm diameter, Alfa Aesar) was utilized as the working electrode and was submerged in solution approximately 1 cm above the Pt wire counter electrode. The reference potential was determined by a non-aqueous Ag wire quasi-reference electrode (QRE) in a tetrabutylammonium perchlorate (TBAP) solution in acetonitrile. A 1 mM R6G solution was prepared in 100 mM TBAP in acetonitrile. For the surface cyclic voltammetry measurements, a polished 2 mm diameter Ag disc electrode (CH Instruments) was incubated in 150 µM R6G-d_0 for 15 minutes and then gently rinsed with acetonitrile to remove any unbound molecules. The supporting electrolyte solution was degassed with N_2 for 30 minutes prior to obtaining electrochemical measurements. Electrochemical measurements were performed using a CH Instruments potentiostat (CHI660D).

R6G Neutral Radical Absorbance Characterization. Thin layer cells were prepared by first attaching Ag wire to an ITO coverslip using Ag colloidal paste (Ted Pella). Next, a clean glass coverslip was placed on top and the outsides were sealed with TorrSeal epoxy. The cell was clamped together using reverse-close tweezers and allowed to cure overnight. The cell was placed in a custom made freeze pump thaw (FPT) spectroelectrochemical glass cell with 1 cm optic path length. A 1 mM R6G solution was prepared in 100 mM TBAP in acetonitrile. 4 FPT cycles were performed on the solution prior to the measurements. Electrochemical potential was controlled with a CH Instruments Potentiostat (CHI660D) and UV-Vis extinction spectra were acquired using an Agilent Cary 5000 spectrophotometer. Solution phase CVs were simulated using the cyclic voltammetry fitting mode of DigiElch (version 6.0) simulation software.

Ag Nanoparticle Synthesis. Silver colloids were synthesized using the Lee and Miesel method.[7] Briefly, 90 mg silver nitrate was dissolved in 500 mL of water, stirred and brought to boil. Once the solution was vigorously boiling, 10 mL of a 1 % w/v trisodium citrate solution was added under strong stirring. This solution was boiled for 30 minutes, removed from the heat and allowed to cool to room temperature; then the final volume was topped off at 420 mL with ultrapure water. Transmission electron microscopy characterization of the colloid showed spherical silver particles of approximately 56 ± 13 nm in diameter. The silver colloid was stored in darkness and used within one week.

Sample cell for EC-SERS. A glass cell for spectroscopic and electrochemical measurements and for FPT of the solvent were custom blown (Reliance Glassware, Elk Grove, IL). The sample cell consists of two inlets for Ag and Pt wire, as well as a #5 valve connection (Figure 2.2A and Figure 2.3B). The FPT cell consists of a tube for the solvent, and a two #5 valve connections for connection to the pump and sample cell (Figure 2.3A).

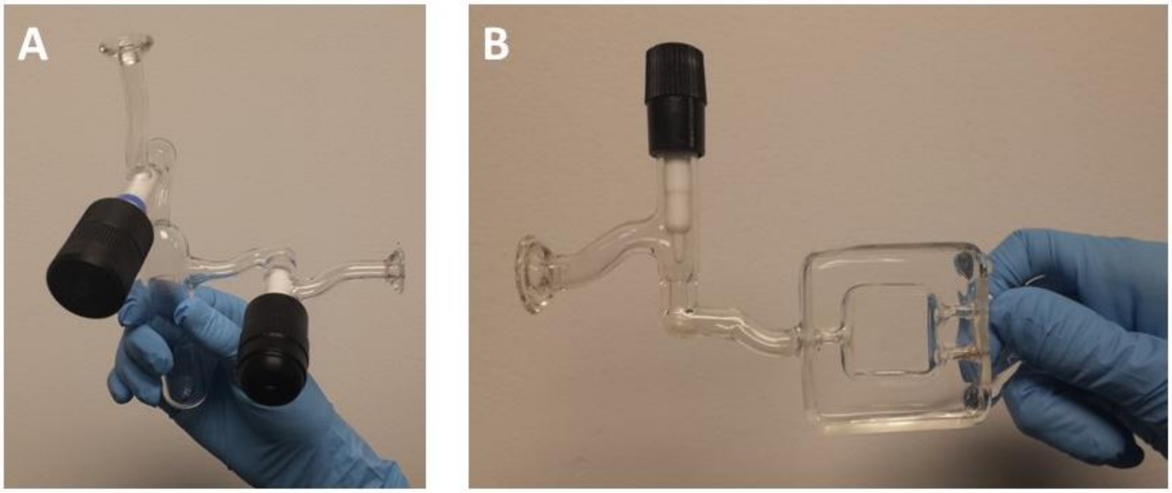

Figure 2.3 Experimental glassware for EC-SMSERS experiment. Photographs of the A) custom-made glass freeze pump thaw cell and B) glass spectroscopic cell.

EC-SERS and EC-SMSERS Sample Preparation. Briefly, 2 mL of the as prepared Ag colloids were washed and concentrated by two centrifugation steps (2000 rpm, 6 min; supernatant to 5000 rpm 6 min), the pellets were redispersed with 0.5 mL of ultrapure water. For the SERS sample, to the colloid 100 µL of 1 x 10^{-5} M total (50 µL of 0.5 x 10^{-6} M each) of R6G-d_0 and R6G d_4 isotopologues was added and incubated with mild stirring for one hour. For the SMSERS sample, to the colloid 100 µL of 1 x 10^{-7} M total (50 µL of 0.5 x 10^{-8} M each) of R6G-d_0 and R6G-d_4 isotopologues was added and incubated with mild stirring for one hour. We calculated the maximum R6G:nanoparticle ratio at the SM concentration regime as 3:1, assuming total reduction of silver salt to 30 nm spherical nanoparticles[7] and complete (100%) adsorption of R6G molecules to the particles surface. We assume that R6G:nanoparticle ratio is close to 1:1 in our final experimental conditions since i) during the incubation, not all the R6G might adsorb[20] ii) after incubation the samples were thoroughly rinsed and iii) further desorption of R6G might take place to the electrolyte solution. Later, 0.5 mL of 40 mM NaCl was added to induce nanoparticle aggregation and left overnight before using the sample. ITO coverslips (22 x 22 mm^2, 8-12 Ω, copper busbar, SPI Supplies) were functionalized with (3-mercaptopropyl)trimethoxysilane to covalently attach the Ag nanoparticles. First, the ITO was sonicated in isopropanol for 5 minutes, then cleaned in a solution of 5:1:1 $H_2O:NH_3OH:H_2O_2$ for 12 minutes at 50 ºC. Then, 0.5 mL of (3-mercaptopropyl)trimethoxysilane in 50 mL isopropanol was allowed to react at RT for 5 minutes. The Ag colloids were then drop casted onto the ITO surface and allowed to dry in an N_2 environment and then substrates were thoroughly washed to remove any unbound particle or salts. After the ITO is fully dried with N_2, copper tape is placed on the ITO to allow for electrical contact. The sample is then mounted on the SMSERS glass sample cell using TorrSeal epoxy (Duniway

Stockroom Corporation, Fremont, CA) and allowed to cure overnight. Next, the cell is placed under vacuum and the supporting electrolyte is transferred in vacuum in order to remove oxygen and water, which quenches radical species and/or cause R6G degradation. The assembled cell was connected to the custom FPT cell which is then connected to a custom built high vacuum line (base pressure = ~10^{-6} Torr). The FPT cell is then filled with 10-15 mL electrolyte solution prior to FPT and solvent transfer to the SMSERS cell. After solvent transfer, the SMSERS cell valve was closed and was disconnected from the FPT cell for spectroscopic measurements.

EM Characterization. SEM images were obtained using a FEI Helios NanoLab 600 microscope operating at an acceleration voltage of 3.0 kV and an operating current of 1.4 nA.

Raman Instrumentation. Samples were analyzed on an inverted microscope (Nikon Eclipse Ti-U) with a 100x oil immersion objective and 0.5 numerical aperture. Particle aggregates are initially viewed under dark field illumination with a 0.8-0.95 numerical aperture condenser. To illuminate the entire field of view for SMSERS measurements, a 532 nm CW laser (Millenia VIIIs, Spectra Physics) was focused onto the sample using grazing incidence at an angle of 60° relative to the surface normal. Scattered light was collected from SERS active particles, laser light was filtered (RazorEdge Long Pass 532 nm Filter, Semrock) and focused onto a 1/3 m imaging spectrograph (SP2300, Princeton Instruments). The scattered light was then dispersed (1200 groove/mm grating, 500 nm blaze) and focused onto a liquid nitrogen-cooled CCD detector (Spec10:400BR, Princeton Instruments).

2.3. Results and Discussion

2.3.1. Electrochemical Characterization of R6G System

Prior to SMSERS measurements, we characterized the bulk electrochemistry of R6G in solution and adsorbed on silver surfaces. R6G undergoes a 1-electron transfer, as shown in the schematic in Figure 2.1A. The solution phase cyclic voltammogram (CV) using a silver wire working electrode is displayed in Figure 2.1B. In this figure, a peak separation of 64 mV is observed, which is common in diffusion-controlled process; as well as a good correlation between the experimental (solid line) and simulated (open circles) CVs. Also, we observed a linear relationship between the solution phase CV cathodic peak current and the square root of the scan rate which indicates that this is a reversible, diffusion-controlled process (Figure 2.4). Next, we studied the electrochemical

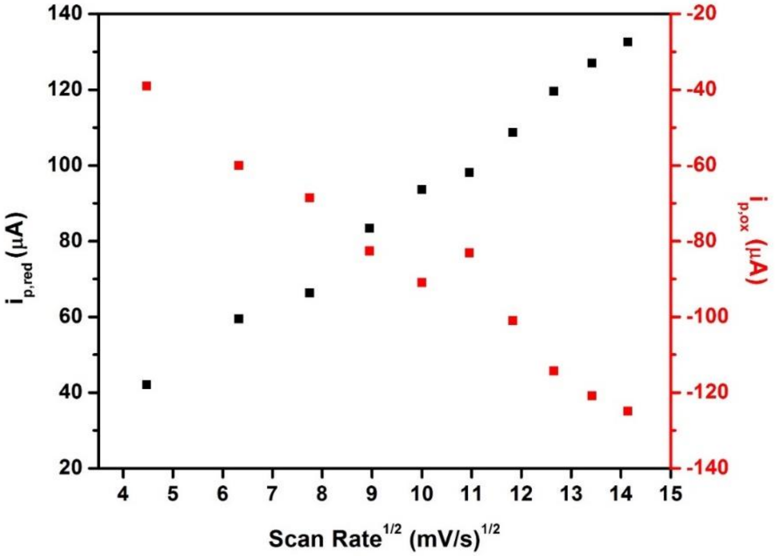

Figure 2.4 Demonstration of well-behaved, reversible electrochemistry for R6G in solution. Square root of scan rate versus peak reduction (black) and oxidation (red) current for 1 mM R6G in 100 mM TBAP in acetonitrile. (Ag wire working electrode, Pt wire counter electrode, Ag wire QRE)

behavior of R6G adsorbed on Ag nanoparticles (NPs) on ITO i.e. a high-coverage analog of the electrode used for SMSERS measurements as shown in Figure 2.1C. We note that the magnitude of the reduction and oxidation peaks are not equal, suggesting electrochemical desorption of the R6G neutral radical species after reduction. Additionally, the difference in shape between the solution CV in Figure 2.1B and surface CV in Figure 2.1C is due to background capacitance, characteristic of a surface CV.[110] In the case of AgNPs on ITO as working electrode, when the CV scan rate is increased, we observe a linear relationship with the position of the peak cathodic current, indicative of uncompensated solution resistance (Figure 2.5, black trace).[110] Also, we confirm that R6G is the surface-bound electroactive species by plotting the cathodic peak current versus scan rate. This relationship is linear which confirms a surface-bound electroactive species[110] (Figure 2.5, red trace). These results show that R6G has well-behaved electrochemistry as a surface-bound species on an AgNP surface. This thorough characterization of R6G

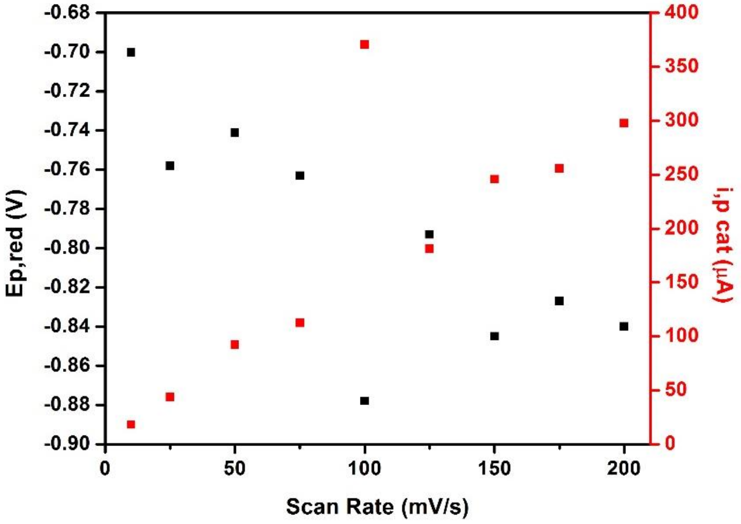

Figure 2.5 Electrochemical demonstration of uncompensated solution resistance and the presence of a surface-bound electroactive species. Scan rate versus peak reduction potential (black) and peak reduction current (red) for high coverage R6G adsorbed on AgNPs in 100 mM TBAP in acetonitrile. (Pt wire counter electrode, Ag wire QRE)

electrochemistry at high concentration and coverage gives us a solid platform to compare multi-molecule and single-molecule reduction potential data.

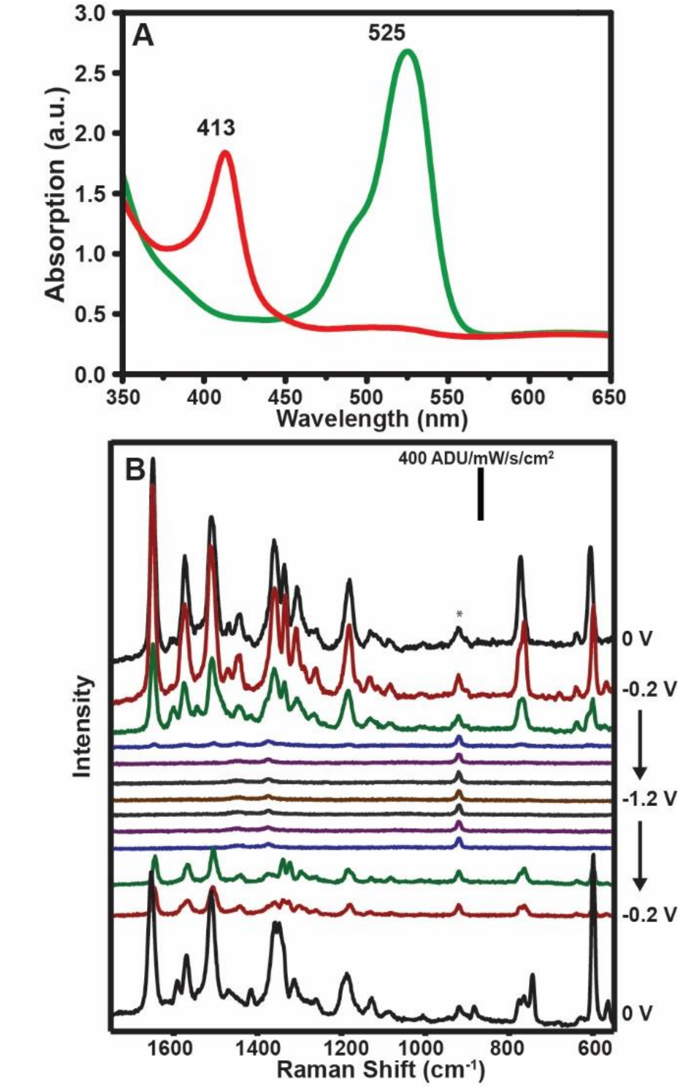

Figure 2.6 EC-SERS of R6G at many-molecule coverage. (A) Thin-layer absorbance spectra of 1 mM R6G in 100 mM TBAP in MeCN with no potential applied (green trace) and after 1 minute -0.8 V applied potential (red trace). The absorbance measurements were performed with an ITO thin layer working electrode, Ag wire quasi reference electrode, and a Pt wire counter electrode and (B) EC-SERS of R6G at many molecule coverage where the potential is swept from 0 V (black trace) to -1.2 V (brown trace) in -0.2 V steps, then stepped back to 0 V. The signal is lost at -0.8 V (top purple trace) and returns at -0.4 V (bottom green trace). The starred peak is due to the acetonitrile solvent.

Later, we characterized the absorbance of the R6G cation and neutral radical species to know if a resonance contribution to the SERS signal is feasible for both species at our experimental conditions (i.e. 532 nm excitation). In order to characterize the relative absorption maxima absorbance of R6G cation and neutral radical, we performed thin-layer chronoabsorptometry. After holding the potential at -0.8 V for 1 minute, the cation is fully reduced to the neutral radical, which exhibits an absorption maximum at 413 nm (Figure 2.6A). This behavior is reversible; after holding the potential at -0.2 V, the absorption trace of the R6G neutral radical is lost and the R6G cation returns.

Lastly, we characterized the electrochemical SERS (EC-SERS) response of R6G on AgNPs covalently attached on ITO (Figure 2.2A) at multi-molecule coverage using 532 nm excitation. The spectral response was monitored from a single nanoparticle aggregate as the potential was stepped from 0 V to -1.2 V and back to 0 V in 0.2 V steps, where the potential was held equal to the length of a spectral acquisition. We observe reversibility in SERS signal as a function of applied potential (Figure 2.6B), where the SERS signal is lost at -0.8 V and returns at -0.4 V.

From the macroscopic scale electrochemical characterization and multi-molecule EC-SERS measurements we conclude that: i) R6G has well-behaved 1-electron transfer both in solution and adsorbed on Ag working electrodes and ii) the electronic resonance of the neutral radical is off-resonance relative to the 532 nm excitation used for EC-SMSERS measurements. Therefore, in this work, the optical readout of a reduction event is defined as the loss of R6G cation SMSER(R)S signal due to the conversion to its neutral radical species.

2.3.2. Proof of SMSERS Behavior

SMSERS detection was first statistically proven with the frequency domain proof in our laboratory by Dieringer *et al.*[25] The benefit of this approach over the bianalyte proof approach is that the analytes have identical surface binding chemistry and Raman scattering cross sections. To this end, equal amounts of R6G-d_0 and R6G-d_4 isotopologues are used in low coverage of the sample The SMSERS substrate used for these experiments is salt-aggregated Ag Lee and Miesel colloids incubated with 50 µL 10^{-7} M of each isotopologues, R6G-d_0 and R6G-d_4. The particles are then drop-casted on ITO functionalized with (3-mercaptopropyl)trimethoxysilane (MPS), which serves as the working electrode. The Ag nanoparticles covalently bind to MPS, as depicted in the schematic in Figure 2.2A. This ensures that the AgNPs are electroactive and will not detach

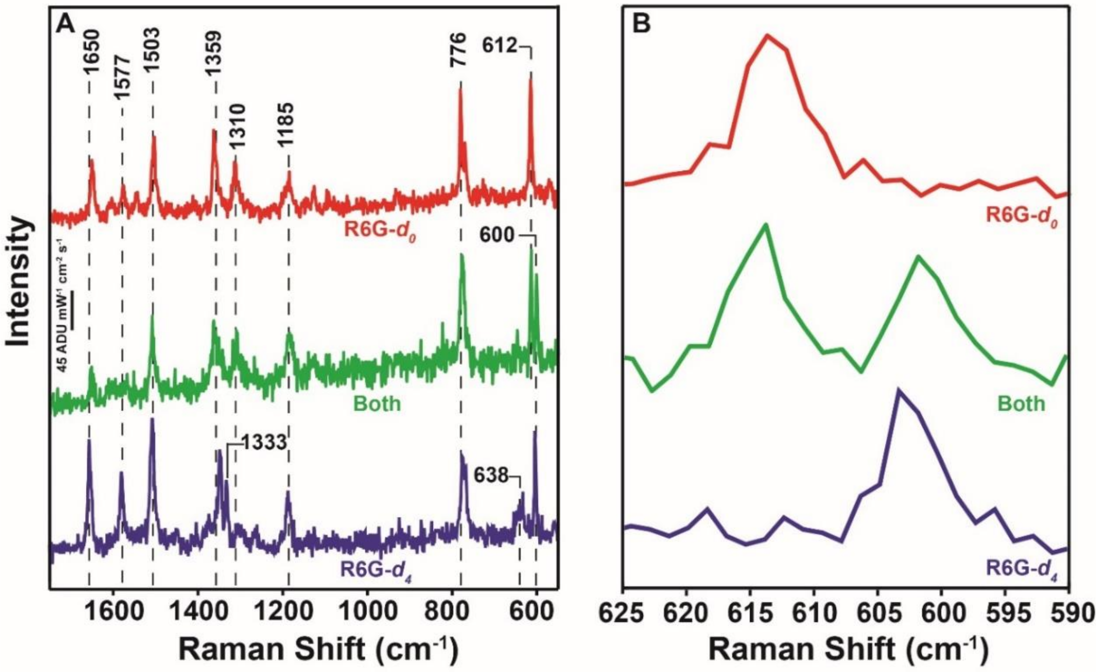

Figure 2.7 Representative SMSERS spectra of R6G. (A) Representative SMSERS spectra of R6G-d_0 (red), both (green) and R6G-d_4 (blue). (B) SMSERS spectra focused on the 600 cm^{-1} region, displaying the unique isotopologue spectral features for R6G-d_0 (red) and R6G-d_4 (blue). Data acquisition parameters for SMSERS measurements were: λ_{ex} = 532 nm, P_{ex} = 13.6 mW, t_{acq} = 3 s.

from the ITO during SERS measurements. Figure 2.2C shows a representative SEM image of the Ag colloids functionalized to an ITO coverslip. The SEM images show that the particles are heterogeneous in size and shape and, more importantly, that the aggregates are well distributed on the ITO, enabling SMSERS measurements.

Figure 2.7A shows representative SMSERS spectra of R6G-d_0 (red trace), R6G-d_4 (blue trace), and both (green trace). In order to differentiate those possible events, i.e. single isotopologue or mixed isotopologues spectrum, we use the characteristic vibrational modes of each molecule. More precisely, there is a clear spectral distinction between the 601 cm^{-1} peak of R6G-d_0 and the 610 peak of R6G-d_4, therefore this spectral region was used to differentiate the isotopologues (Figure 2.7B). Additionally, R6G-d_4 exhibits a unique doublet feature at 1350 cm^{-1} and 1330 cm^{-1} which was also used for molecular identification. SMSERS spectra were acquired from 80 individual particle aggregates for which the events were classified as shown in the histogram in Figure 2.8B. The ratio of R6G-d_0:both:R6G-d_4 events is 35:5:40 or 7:1:8, confirming single-molecule detection. Our results deviate from a theoretical binomial Poisson distribution for one molecule per particle with a probability ratio of 2.5:1:2.5 and this deviation can be attributed to having less than one R6G molecule per particle, molecules located outside a hot spot during spectral acquisition, molecules not bound to the surface during the incubation time and/or molecules desorbed in solution.[25]

2.3.3. EC-SMSERS Signal Potential Dependence

For electrochemical SMSERS (EC-SMSERS) measurements, the SMSERS signal of each single Ag nanoparticle aggregate was monitored as the potential was stepped from 0 to -1.2 V in 0.1 V intervals and then swept positive from -1.2 to 0 V in 0.1 V intervals. The potential was held constant for the length of SMSERS spectral acquisition (pulse width = 3 s) and the total acquisition time was relatively long (~ 5 min). A representative trace of the potential step function and the corresponding SMSER signal response is shown in Figure 2.8A and Figure 2.8C, respectively. The histogram in **Figure 2.8**D corresponds to the R6G SMSERS signal loss events that we understand as the potential at which the R6G cation was reduced to the neutral radical species. Figure 2.8D only includes single isotopologue signal loss events; we do not include 'both' isotopologues spectra. In our experiments, we do not observe SMSERS spectra of the neutral radical species with 532 nm excitation because of the absence of resonance enhancement. The total number of events

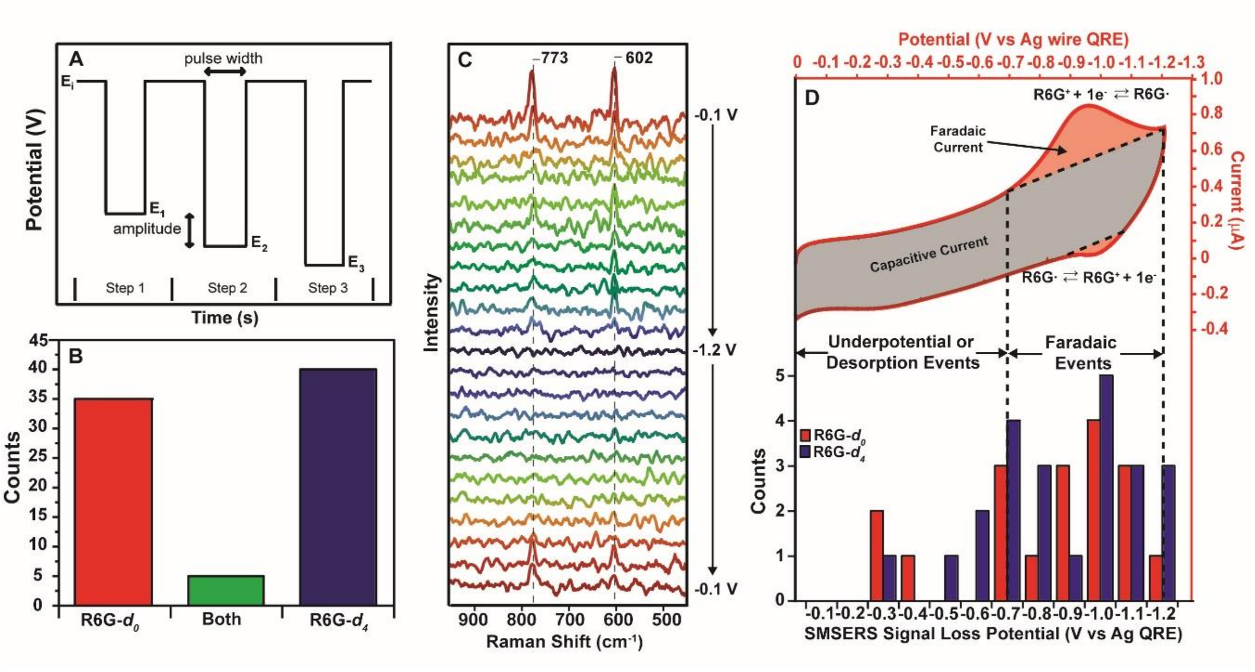

Figure 2.8 SMSERS validation and EC-SMSERS Signal Loss Histogram. (a) Representative trace of the potential step function applied in electrochemistry measurements to each single Ag nanoparticle aggregate, where E_i = 0 V, E_1 = -0.1 V. The amplitude between steps is -0.1 V and the pulse width is equivalent to the spectral acquisition time. (b) Histogram displaying all SMSERS events. (c) Representative SMSERS spectra from a single particle aggregate displaying signal change as a function of applied potential. The SMSERS signal is lost at -1.2 V (center, dark blue trace) and returns at -0.2 V (bottom, red trace). (d) Surface CV of high coverage R6G on a polished Ag disc electrode in 100 mM TBAP in MeCN (top) compared to the histogram of all SMSERS measured signal loss events (bottom).

in Figure 2.8D (44) is less than that of the histogram in **Figure 2.8**B due to signal loss prior to the electrochemical measurements. Sporadic intensity fluctuations, ‘blinking’, and signal loss are common in SMSERS measurements as a result of molecular diffusion, variations of the electric field enhancement, photobleaching and photochemical effect among others,[25,95] making data acquisition challenging. Figure 2.8D includes only those particle aggregates in which SMSERS signal was stable for more than ~ 1 min before the potential step. Overall, it was found that there was significantly less random blinking and signal loss in the liquid cell as compared to previous SMSERS experiments performed in air or nitrogen. Not included in Figure 2.8D were 17 other studied particles that did not undergo SMSERS signal loss with the applied potentials. More likely, these particles did not have electrical contact due to defects on the ITO surface or to the particle aggregate required a much more negative potential to sufficiently reduce the R6G molecule.

Only 2 SMSERS signal loss events in Figure 2.8D had a corresponding signal return, or oxidation. In both cases, the signal return occurred at -0.2 V, which is similar to the behavior observed in the high coverage SERS data (Figure 2.6B). Possible sources for complete SMSERS signal loss includes hot spot reshaping or particle desorption from the ITO, quenching of the R6G radical with water or oxygen traces, or molecular diffusion outside the hot spot. Additionally, this results correlates strongly to the fact that the reduction and oxidation peaks are not of equal magnitude in the surface CV of or AgNPs on ITO (Figure 2.1C) or R6G on polished Ag (**Figure 2.8**D). We hypothesize that molecular diffusion or desorption away from the hot spot of the neutral radical species is the main cause of complete SMSERS signal loss after a reduction event. It is also possible that the SMSERS signal is lost due to potential-induced structural changes to the nanoparticle aggregate and therefore loss of SMSERS activity in the hot spot.[111-113]

We attempted to differentiate between possible non-electrochemical desorption of the R6G cation before the potential step (Equation 2.2) from electrochemical desorption of the neutral radical during or after the reduction (Equation 2.3):

$$\mathrm{R6G}^{+}_{\mathrm{surf}} \underset{k_{\mathrm{d}}}{\overset{k_{\mathrm{ads}}}{\rightleftarrows}} \mathrm{R6G}^{+}_{\mathrm{soln}}$$

(Equation 2.2)

$$\mathrm{R6G}^{+}_{\mathrm{surf}} + \mathrm{e}^{-} \underset{k_{\mathrm{d}}}{\overset{k_{\mathrm{ads}}}{\rightleftarrows}} \mathrm{R6G}\cdot_{\mathrm{surf}} \underset{k_{\mathrm{a}}}{\overset{k_{\mathrm{d}}}{\rightleftarrows}} \mathrm{R6G}\cdot_{\mathrm{soln}}$$

(Equation 2.3)

For this, we repeated the measurements stepping the potential only in the underpotential window, from -0.1 to -0.7 V, as compared to the surface CV in Figure 2.1C. We chose to step within this potential window because there should be few electrochemical events occurring, and therefore there should be no SMSERS signal loss with the potential step. In this experiment, 16 of 20 SMSERS spectra collected showed no signal loss during the potential step; the consistent SMSERS signal indicates that neither R6G cation desorption (Eq. 2.2) nor electrochemical reduction followed by radical desorption (Eq. 2.3) occurred (Figure 2.9A). Of the 20 SMSERS spectra collected, 4 showed signal loss between -0.4 V and -0.7 V as illustrated in Figure 2.9B, which could be caused by Eq. 2.2 or Eq. 2.3. We are inclined to think that these 4 cases were most likely reduction events followed by diffusion of the radical as represented by Eq. 3. Due to the fact that at this control experiment we do not observe any signal loss at -0.3 V we assume that the loss events observed at -0.3 V in Figure 2.8D are most likely caused by desorption of the R6G cation (Eq. 2.2) and we hypothesize that the complete SMSERS signal loss between -0.6 V and -1.2 V, without signal return or oxidation, is probably due to electrochemical desorption of the R6G neutral radical (Eq. 2.3).

We observe a broadened SMSERS signal loss potential distribution (Figure 2.8D) relative to the Faradaic region in the surface CV. In light of this, we now discuss the origin of the broadened distribution of the SMSERS R6G signal loss potential histogram. For example, a similar broadening effect has been observed in a SMSERS experiment across a smaller potential range for an aqueous 2 electron, 2 proton transfer of Nile Blue (NB) from Cortés *et al*.[58,60] The authors found

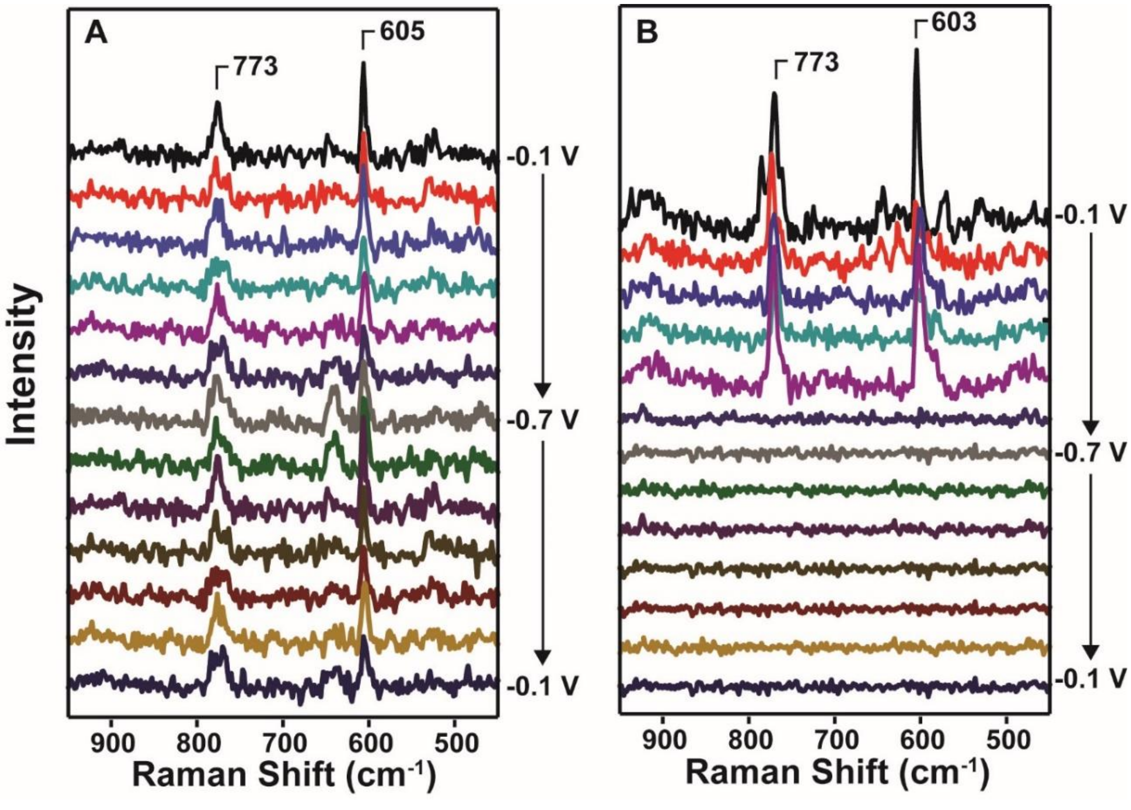

Figure 2.9 EC-SMSERS in the underpotential region. (A) Representative SMSERS spectra from a potential sweep in the underpotential region (-0.1 - -0.7 V), which displays no loss in SMSER signal. This indicates that SMSERS signal loss is not due to R6G cation desorption. (B) Representative SMSERS spectra from a potential sweep in the non-Faradaic region which displays a loss in SMSER signal at -0.6 V, further indicating that SMSERS signal loss is most likely due to electrochemical reduction of R6G and not R6G cation desorption.

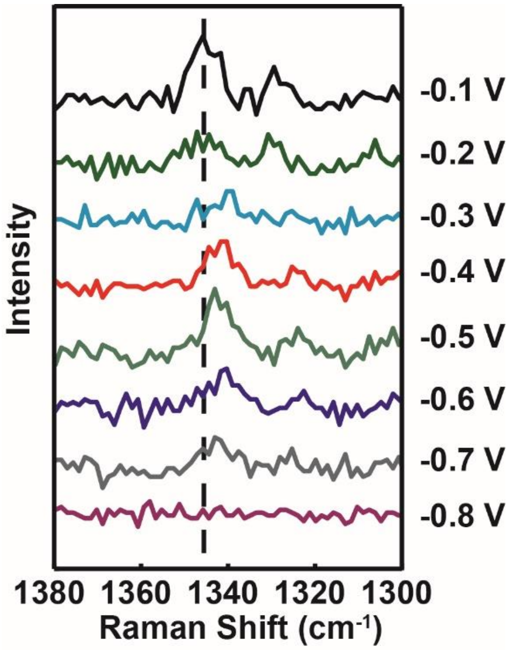

Figure 2.10 Representative SMSERS spectra displaying a blue shift in the 1350 cm^{-1} mode of R6G as a function of increasingly negative potential.

a correlation between the peak positions of the 590 cm^{-1} ring breathing mode in NB to the reduction potential. They attribute this phenomenon to molecular orientation and the molecule’s relative interaction strength with the nanoparticle surface. Additionally, another study by Salverda *et al.* found that when azurin, a Cu protein, is bound on Au electrodes at low coverage, the electron transfer rates were broadly distributed, which they attributed to heterogeneous protein orientation.[50] Based on these preceding studies and our experimental results, we propose two primary contributing factors to the observed broadened potential distribution: molecular reorientation on the surface and variations in the local hot-spot nanostructure, surface curvature or surface chemical potential, including in the former variations due to surface curvature and oxide layers.

We note that we do not attempt to extract information of the molecular position on the surface from the relative intensities of the SMSERS signal. Commonly, the intensity of SERS spectra will decay accordingly to the distance of the Raman molecule to the substrate.[114] Distinctly, at single molecule level, the intensity of the peaks might change due to the distance or relative position of the molecule to the hot spot or variations in its excited-state properties.[115] To this end, we analyze the R6G peak positions as a function of potential, which is sensitive to position relative to the AgNP surface.

To simplify the spectral analysis, we divide it into 2 regions. First, we examine the 600 cm^{-1} region R6G peak, which has been determined by DFT calculations to be a ring breathing mode.[116] While the position of the mode varies spectrum to spectrum, we do not observe any correlation between the applied potential and peak position shift. Also, there is no connection between peak position and the potential of an SMSERS signal loss event when correlating the data in Figure 2.8D to that of Figure 2.11A. Then, we examined the 1350 cm^{-1} region mode, determined by DFT calculations to have 93.9% ethylamine moiety vibrational character and hypothesized as the anchoring moiety.[116] If R6G binds to the Ag nanoparticle surface via the ethylamine moiety its corresponding vibrational mode peak position should therefore be sensitive to changes in the orientation relative to the Ag nanoparticle. In half of the spectra collected, there is a blue shift of the 1350 cm^{-1} mode with increasingly applied negative potential (Figure 2.10). Yet, there is no correlation between the peak position and the reduction or signal loss potential when correlating the data from Figure 2.8D to Figure 2.11B. The shifts observed in the 1350 cm^{-1} mode could be attributed to a vibrational Stark effect, which occurs when a molecular dipole is perturbed by a local electric field.[117-119] Hence, the major difference between our results and Cortés *et al*.[60] is lack of a distinct correlation between Raman shift of either the 600 or 1350 cm^{-1} modes and the applied or reduction potential. Disregarding the difference in the spectral resolution, our measurements were performed with a lower spectral resolution, our results suggest that molecular orientation and interaction with the nanoparticle surface are not the only contributors to the broad SMSERS signal loss potential histogram.

We hypothesize that the major contribution to the broadened SMSERS signal loss potential distribution relative to the bulk is due to the local radius of curvature, surface site and corresponding surface chemical potential of the specific site of the Ag nanoparticle where the R6G

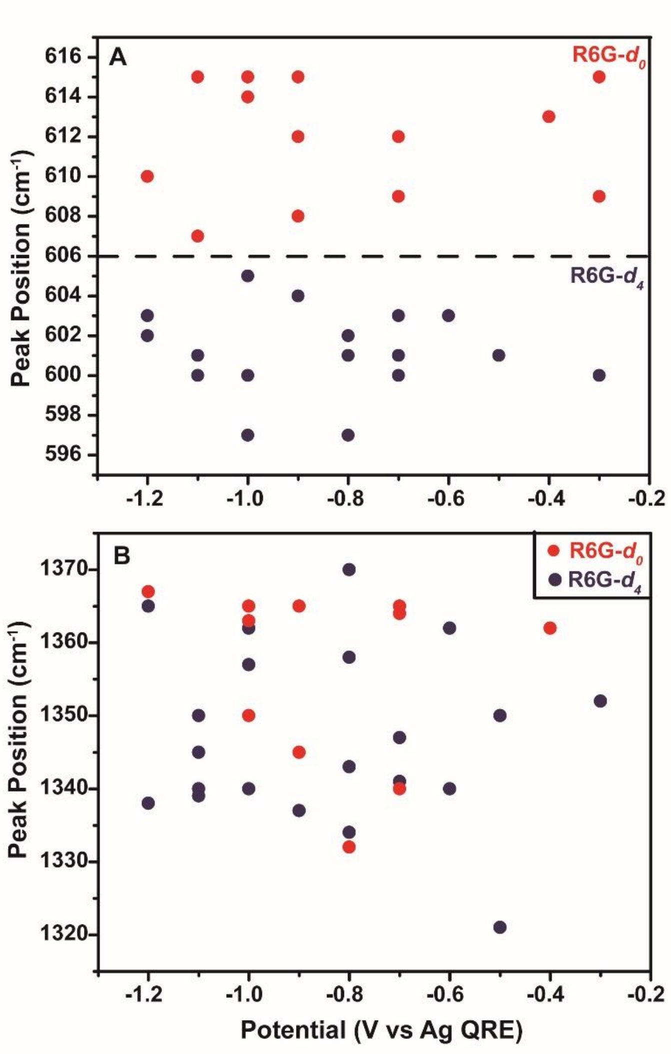

Figure 2.11 R6G vibrational mode positions versus applied potential. Plot of the (A) 600 cm^{-1} mode position and (B) 1350 cm^{-1} region mode versus SMSERS signal loss potential from R6G-d_0 (red) and R6G-d_4 (blue).

molecule is bound. Preceding theoretical and experimental studies indicate the structure-dependent electrochemical behavior of Ag nanostructures and that sharp, small radius of curvature features are the most electrochemically active.[120-123] For example, Zhang *et al.* measured the electrochemical oxidation of Ag nanotriangles and found that as a positive potential is applied to the substrate, the sharp, bottom edges first oxidize, followed by the more rounded triangular tip regions.[124] This behavior was rationalized based on a previous statement that the work function of a small, metallic particle varies inversely with the radius of a metallic nanoparticle. Recent work has also demonstrated the heterogeneous chemical activity of various nanoparticle shapes and sizes on the single particle level and supports the idea that electrochemical activity is dependent on surface structure.[51] We can extend these ideas to our findings, postulating that particles with smaller radii of curvature, or sharper nanofeatures, will be more electrochemically active and therefore lead to SMSERS underpotential events. For our SMSERS measurements, the subtle difference in local surface site structure, binding geometry and overall nanoparticle shape and size can be a possible explanation of the lack of correlation between the broad potential range of SMSERS signal loss events and the Raman shifts observed.

2.4. Conclusions

In summary, we first characterize the bulk electrochemistry of R6G, which undergoes a single electron redox reaction. Next, we characterize the spectroelectrochemical response of the R6G electron transfer reaction with absorbance spectroscopy and SERS at high R6G coverage. Finally, we demonstrate the first observation of single-electron transfer with EC-SMSERS. The potential distribution of SMSERS signal loss events is broader than of the bulk electrochemical system. We attribute this behavior to variations in molecular orientations and variations in the radius of curvature, binding site and/or chemical potential where the R6G molecule is bound to the Ag nanoparticle substrate. Future efforts will address the correlation of SMSERS measurements with electron microscopy to understand nanofeatures impact on the distribution of reduction potentials together with density functional theory (DFT) calculations. Overall, this work has presented challenges involved in studying single-molecule single-electron electrochemical events through SERS, and pursue electrochemical control at the nanoscale.

Chapter 3. Towards Monitoring Electrochemical Reactions with Dual-wavelength SERS: Characterization of R6G Neutral Radical Species and Covalent Tethering of R6G to Silver Nanoparticles

3.1. Introduction

The study of electron transfer (ET) reactions has been rapidly moving towards the nanoscale with the aim of understanding fundamental, site-specific electrochemical behavior. Micro- and nanoscale electrodes in current-detection techniques yields site specific information about molecular or particle collisions with the electrode, however, nanoscale electrodes are challenging to fabricate reproducibly and amperometric redox cycling methods do not provide structural information about the redox couple being studied.[47,48] Optical techniques such as fluorescence or Raman spectroscopy provide an attractive alternative to studying ET reactions.[49,51-54,59] In particular, SERS is a powerful tool to monitor few- to single-molecules reacting on a nanoscale electrode, where the loss or gain in SERS signal is correlated to the applied potential and therefore determines the occurrence of an ET event.[12,58,60,61,63,69,80] Using SERS over other techniques is advantageous in that it provides the vibrational spectra of adsorbates, and by comparison of the experimental spectra to previous literature or theoretically calculated SERS spectra, structural changes can be monitored while the electrochemical reaction progresses.

Electrochemical SERS (EC-SERS) and TERS (EC-TERS) have recently been demonstrated as a very useful means of studying electrochemistry at the nanoscale. While EC-TERS has the potential to provide direct, correlated structural information of the electrochemically active surface/molecule pair being probed, non-aqueous EC-TERS is experimentally challenging due to the open configuration of the scanning probe tip and cell. Therefore, EC-SERS is an excellent means of studying single-electron transfer events in non-aqueous environments. The majority of recent EC-SERS and EC-TERS reports have focused on studying the redox activity of large dye molecules, specifically phenoxazine dye Nile Blue (NB)[58,60,61,69,70,80,125,126] and Rhodamine-6G

(R6G) . The electrochemical and optical activity of NB has been well-characterized: NB undergoes a reversible two-proton, two-electron reduction at pH 2-6 and a two-proton, one-electron reduction at pH 6-10.[126] The reduced form of NB is optically active in the visible region (~640 nm) and oxidized form is optically active in the UV (365 nm).[69] Previous studies monitor the reduction of NB by monitoring the loss in oxidized NB SERS signal. Alternatively, R6G, in non-aqueous conditions, undergoes a one-electron transfer redox reaction where the oxidized form of R6G strongly absorbs at 532 nm and the reduced form absorbs at 413 nm. Previous work, discussed in Chapter 2, monitored the loss of R6G cation signal at 532 to indicate electrochemical reduction to its neutral radical form, which can currently only be experimentally realized with EC-SERS. The absorbance and SERS spectra of both the redox forms of NB have been reported previously,[69,126] but only the oxidized form of R6G has been characterized with SERS. Full spectroscopic characterization of both redox states of optically active dyes used in EC-SERS experiments can provide a greater insight on the electrochemically-induced structural changes and overall site-specific redox activity of these molecules.

The outcome of studying nanoscale electrochemistry with EC-SERS is site-specific molecular electrochemical reactivity of the adsorbate. However, there are experimental challenges that need to be addressed in order to successfully perform EC-SERS and accurately interpret the spectroelectrochemical data. The major experimental challenge for EC-SERS, especially at the single-molecule level, is the loss of molecular emissivity over the course of successive potential scans. The loss in emissivity can originate from molecular desorption or oxygen-induced losses, which severely limits the number of molecules that can be probed in a single experiment.[61,63] Previous reports have also demonstrated potential-dependent alterations in nanoparticle structure as an avenue of loss in emissivity.[111,112] One strategy to prevent desorptive losses during an EC-SERS measurement is to covalently link the redox probe of interest to the electroactive SERS substrate instead of relying on spontaneous adsorption. Carbodiimide crosslinking forms amide bonds between a primary amine and a carboxylic acid group, and is a common strategy used in forming "zero-length" bonds between two biomolecules.[127] *N*-(3-Dimethylaminopropyl)-*N′*-ethylcarbodiimide hydrochloride (EDC) is a common coupling agent for carbodiimide crosslinking, as it is relatively stable and soluble in water. The EDC crosslinking reaction is illustrated in Figure 3.1, where the EDC and carboxylic acid form an *O*-acylisourea intermediate (Figure 3.1, step 1). That intermediate then reacts with sulfo-NHS to form a sulfo-NHS ester intermediate (Figure 3.1, step 2), and the primary amine acts as a nucleophile to displace the sulfo-

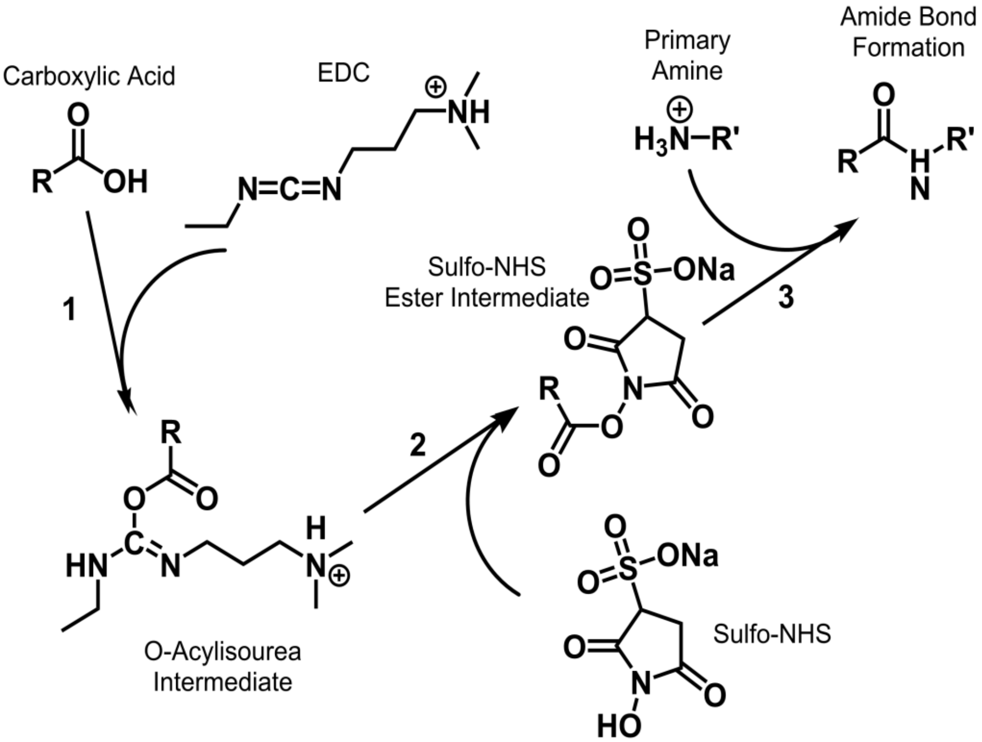

Figure 3.1 EDC Crosslinking Reaction Schematic. EDC reacts with a carboxylic acid to form an *O*-acylisourea intermediate. The primary amine of interest acts as a nucleophile to displace the sulfo-NHS from the sulfo-NHS ester intermediate carbonyl group, and form the desired amide bond. Figure adapted from Bioconjugate Techniques, Greg T. Hermanson,. 2nd Ed., pages 219-220.

NHS moiety to form the desired amide bond between the carboxylic acid and the primary amine (Figure 3.1, step 3). While the addition of sulfo-NHS is not necessary, it increases the stability of the ester intermediate and improves the overall reaction yield. Recently, the Willets group used EDC crosslinking to tether NB to SERS-active electrodes.[62,80,125] Interestingly, the authors found that the presence of the amide bond and the length of the alkanethiol chain will alter the electrochemistry of NB, as observed with differential pulse voltammetry and high-coverage SERS measurements on Au island films. This finding implies that new molecules or sample preparation strategies for studying nanoscale electrochemistry must be carefully characterized prior to EC-SERS or EC-TERS measurements in order to properly interpret the results.

Herein, we present work towards complete monitoring of one-electron transfer reactions with EC-SERS. First, we characterize the reduced form of R6G (R6G neutral radical, or R6G·) with resonance Raman spectroscopy (RRS) and correlate the results to theoretical resonance Raman spectra. We then implement EDC crosslinking in order to covalently tether R6G to SERS-active substrates (Ag nanoparticles), and characterize them with cyclic voltammetry (CV) and SERS. For EC-SERS, we study and compare two EDC crosslinking strategies: first, we study a previously reported “heterogeneous” method and we then optimize a novel “homogeneous” solution-phase crosslinking procedure. Additionally, we compare the SERS and EC-SERS response of spontaneously adsorbed R6G and EDC-coupled R6G on AgNPs to ensure that there are no significant spectral differences due to R6G tethering. Finally, we present recent attempts for detecting covalently tethered R6G neutral radical species with 405 nm excitation. This work demonstrates the importance of sample preparation optimization for EC-SERS measurements and

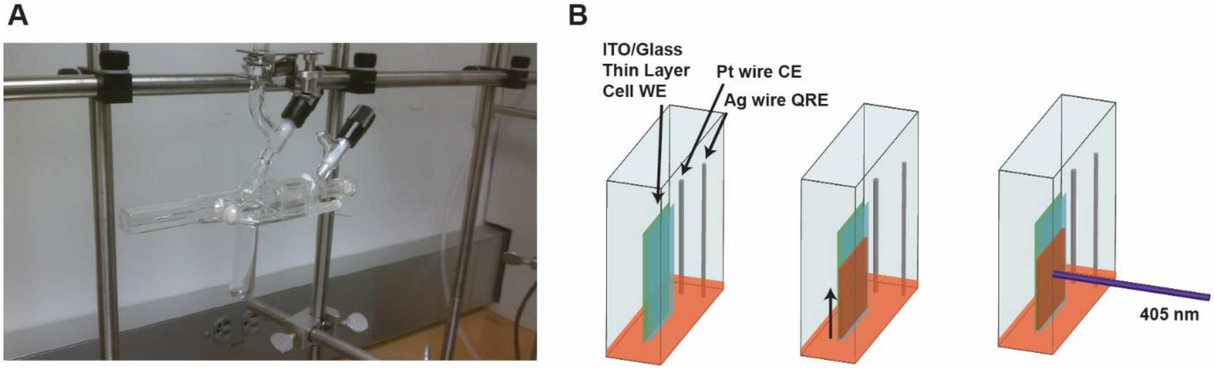

Figure 3.2 Experimental glassware used for electrochemical resonance Raman spectroscopy (EC-RRS) experiment. A) Photograph of glassware used for EC-RRS measurements. B) Schematic of capillary action in the thin layer cell, where the solution of interest is added to the bottom of the glass cuvette cell, the solution is drawn up into the thin layer cell via capillary action, and the laser is then focused on the working electrode surface for EC-RRS measurements.

presents steps towards the ultimate goal of studying one-electron reactions and simultaneous detection of both redox states of a single R6G molecule with dual-excitation EC-SERS.

3.2. Experimental

Chemicals. Trisodium citrate dihydrate 90%, silver nitrate +99.99% ($AgNO_3$), sodium chloride +90% (NaCl), tetrabutylammonium perchlorate +99% (TBAP), hydrogen peroxide solution 30% (H_2O_2), ammonium hydroxide solution 28-30% (NH_4OH), (3-mercaptopropyl)trimethoxysilane (MPS), *N*-(2-Aminoethyl)rhodamine 6G-amide bis(trifluoroacetate) (R6G-amine), *N*-(3-Dimethylaminopropyl)-*N′*-ethylcarbodiimide hydrochloride (EDC), *N*-Hydroxysulfosuccinimide sodium salt (sulfo-NHS), 2-mercaptopropionic acid (MPA) and 6-mercaptohexanoic acid (MHA) were purchased from Sigma-Aldrich and used without further purification. HPLC grade acetonitrile (MeCN) (≥99.5%) was purchased from Avantor Performance Materials and further purified prior to use by passing through a Pure Process Technology solvent drying system. Milli-Q water with a resistivity higher than 18.2 MΩ*cm was used in all preparations.

R6G Neutral Radical Absorbance Characterization. Thin layer cells were prepared by first using Ag epoxy (Ted Pella) to attach an Ag wire to a cleaned ITO coverslip. Next, a clean glass coverslip was placed on top and the outsides were sealed with TorrSeal epoxy. The cell was clamped together using reverse-close tweezers and allowed to cure overnight. The cell was then placed in a custom made freeze pump thaw (FPT) spectroelectrochemical glass cell with 1 cm optic path length. A photograph of the cell is shown in Figure 3.2A. A 1 mM R6G solution was prepared in 100 mM TBAP in acetonitrile. 4 FPT cycles were performed on the solution prior to the measurements. Pt wire was used as the counter electrode and an Ag quasi reference electrode (QRE) was used. Electrochemical potential was controlled with a CH Instruments Potentiostat (CHI660D) and resonance Raman spectra were acquired.

SERS Sample Preparation I: Heterogeneous EDC crosslinking on Ag colloids pre-functionalized on ITO. Ag nanoparticles (AgNPs) were prepared using the Lee and Miesel method.[7] Two mL of the as prepared Ag colloids were washed and concentrated by two centrifugation steps (2000 rpm, 6 min; supernatant to 5000 rpm 6 min), the pellets were redispersed with 0.5 mL of ultrapure water, and to induce nanoparticle aggregation, 0.5 mL of 40 mM NaCl was added. ITO coverslips (22x22 mm^2, 8 - 12 Ω, with copper busbar, SPI Supplies) were cleaned by sonication in isopropanol for 5 minutes; then base treated in 5:1:1 H_2O:NH_4OH:H_2O_2 at 50ºC for 12 minutes followed by water and isopropanol rinsing steps, to activate hydroxyl groups. Then, ITO coverslips were functionalized with MPS, where the ITO coverslips were incubated in 0.5 mL MPS in 50 mL isopropanol for 6 minutes at room temperature, and then thoroughly rinsed with isopropanol and dried under N_2. Once dried, 0.15 mL of aggregated Ag colloids were immediately dropcast on the MPS-functionalized ITO and allowed to dry in a N_2 box, after which they were thoroughly rinsed with ultrapure water and dried under N_2. Each clean AgNP-functionalized ITO was immersed in a 10 mM ethanolic solution of MPA or MHA overnight. The sample was then rinsed thoroughly with ethanol and dried with a stream of N_2. Next, 200 µL of 20 mM EDC and 40 mM sulfo-NHS in water was dropcast on the ITO surface and allowed to react for 30 minutes in ambient conditions. The sample was then rinsed thoroughly with water and dried with a stream of N_2. Lastly, 200 µL R6G-amine in pH = 5 phosphate buffer was dropcast on the surface, allowed to react for 2 hours at ambient conditions and rinsed with water and isopropanol and dried with N_2.

SERS Sample Preparation II: Homogeneous EDC Crosslinking on Ag colloids in solution. Five mL of the as prepared Ag Lee and Miesel colloids were washed and concentrated by two centrifugation steps (2000 rpm, 7 min; supernatant to 5000 rpm, 7 min), the pellets were resuspended in 0.9 mL MQ H_2O. 20-90 µL of 1 mM or 10 mM ethanolic solution of mercaptopropionic acid (MPA) or mercaptohexanoic acid (MHA) were slowly and dropwise added to the AgNP solution while vortexing the sample. The AgNP samples were then sonicated for 20 minutes and centrifuged to remove MPA or MHA excess. The particles were resuspended in 0.45 mL of in MQ H_2O under sonication- it is worth noting that they visually appeared aggregated. Then two different methods were used to covalently attach R6G to the AgNP sample. <u>Method II-A</u>: 50 µL of 20 mM EDC and 40 mM sulfo-NHS aqueous solution and 50 µL 140 µM R6G-amine in pH = 5 phosphate buffer were added simultaneously, sonicated for 30 minutes, and then allowed to incubate for an additional 30 minutes without sonication. <u>Method II-B</u>: 50 µL 20 mM EDC and 40 mM sulfo-NHS aqueous solutions was added to the Ag colloid and sonicated for 30 minutes. The sample was then centrifuged (2000 rpm, 5 min) and resuspended in 0.4 mL MQ

H_2O. Later, 50uL of 140 µM R6G-amine in phosphate buffer (pH = 5) was added to the solution and incubated for 2 hours. After each method, either A or B, the sample was centrifuged (2000 rpm, 5 min) and resuspended in 0.3 mL MQ H_2O, and 25 µL of the colloid solution with 50 µL MQ H_2O was dropcasted on a cleaned ITO surface and allowed to dry in a N_2 box. The sample was then thoroughly rinsed with MQ H_2O, acetone and ethanol, respectively, and dried with a N_2 stream.

EC-SERS Sample Preparation. After the functionalized ITO from sample preparation I or II was fully dried with N_2, copper tape is placed on the ITO to allow for electrical contact. The sample was then mounted on the SMSERS glass sample cell using TorrSeal epoxy (Duniway Stockroom Corporation, Fremont, CA) and allowed to cure overnight. Next, the cell was placed under vacuum and the supporting electrolyte is transferred in vacuum in order to remove oxygen and water, which quenches radical species and/or causes R6G degradation. The assembled cell was connected to the custom FPT cell (Figure 2.3) which was then connected to a custom built high vacuum line (base pressure = ~10^{-6} Torr). The FPT cell was filled with 10-15 mL electrolyte solution prior to FPT and subsequent solvent transfer to the SMSERS cell. After solvent transfer, the SMSERS cell valve was closed and was disconnected from the FPT cell for spectroscopic measurements.

FON Fabrication. 25 mm #1.5 circular glass coverslips were first cleaned with piranha solution for 30 minutes (3:1 $H_2SO4:H_2O_2$), rinsed copiously with MQ H_2O and then treated with 5:1:1 $H_2O:H_2O_2:NH_4OH$ for 45 minutes to render the surface hydrophilic. The coverslips were stored in MQ H_2O prior to use. 10-12 µL 300 nm carboxyl latex microspheres (4% w/v, Invitrogen) were dropcasted, homogeneously distributed onto the glass coverslip and then allowed to dry.

After drying, 200 nm Ag was thermally deposited on the FON mask surface at a rate of 2 Å·s $^{-1}$ under vacuum (~5.0 × 10^{-6} Torr) using a custom-built thermal vapor deposition system.

Electrochemical measurements. Surface cyclic voltammetry (CV) measurements of EDC coupled R6G on AgNPs on ITO were performed in a capped scintillation vial. Conductive copper tape was attached onto the border of the ITO surface and extended out 10 cm to make electrical contact with the AgNP on ITO working electrode. The Pt wire counter electrode was shaped into a ~2 cm diameter ring and placed in close proximity to the ITO surface. The reference potential was determined by a non-aqueous Ag wire quasi-reference electrode (QRE) in a 100 mM tetrabutylammonium perchlorate (TBAP) solution in acetonitrile. All electrochemical measurements in this work use this configuration unless otherwise stated. The supporting electrolyte solution was degassed with N_2 for 30 minutes prior to obtaining electrochemical measurements. Electrochemical measurements were performed using a CH Instruments potentiostat (CHI660D). Background subtraction and R6G surface coverage was calculated using a custom exponential fitting procedure in MATLAB.

Raman Instrumentation. RRS spectra of R6G· in the thin layer cell setup were acquired using a macro Raman setup. A 405 nm CW laser (Micro Laser Systems, Inc.) was passed through a clean-up filter (MaxLine® laser clean-up filter, Semrock) to clean up the laser line, and focused on the thin layer cell working electrode surface. The scattered light was back-collected and Rayleigh scattering was filtered out with a notch filter (405 nm StopLine® single-notch filter, Semrock). The filtered light was then focused onto a 1/2 m imaging spectrograph (PI Acton SP2500i, Princeton Instruments), dispersed with a 500 nm blaze 1200 groove/mm grating and focused onto a thermoelectrically-cooled CCD detector (Pixis 400BR, Princeton Instruments).

SERS spectra were acquired on an inverted microscope setup (Nikon Eclipse Ti-U) with a 100x oil immersion objective and 0.5 numerical aperture. Particle aggregates were initially viewed under dark field illumination with a 0.8-0.95 numerical aperture condenser. To illuminate the entire field of view for SMSERS measurements, a 532 nm CW laser (Millenia VIIIs, Spectra Physics) was focused onto the sample using grazing incidence at an angle of 60° relative to the surface normal. Scattered light was collected from SERS active particles, laser light was filtered (RazorEdge Long Pass 532 nm Filter, Semrock) For acquisition of SERS spectra at 405 nm, a 405 nm CW laser (Micro Laser Systems, Inc.) was passed through a band pass filter (MaxLine® laser clean-up filter, Semrock) to clean up the laser line, directed to the microscope objective using a 405 nm dichroic beamsplitter (405 nm laser BrightLine® single-edge super-resolution laser dichroic beamsplitter, Semrock) and focused on the sample surface using the 100x objective. Scattering was back-collected through the microscope objective and laser light was filtered (405 nmStopLine® single-notch filter, Semrock) Scattered light for both 532 nm and 405 nm measurements was then focused onto a 1/3 m imaging spectrograph (SP2300, Princeton Instruments, dispersed (1200 groove/mm grating, 500 nm blaze) and focused onto a liquid nitrogen-cooled CCD detector (Spec10:400BR, Princeton Instruments).

3.3. Results and Discussion

3.3.1. Characterization of the R6G Neutral Radical Species with EC-RRS

We first characterized the R6G neutral radical species (R6G·) using electrochemical RRS (EC-RRS). We note that we did not detect the R6G cation ($R6G^+$) with RRS due to its high fluorescence/quantum yield (0.95).[128] The R6G neutral radical species has a smaller extinction coefficient (2.7 x 10^4 M^{-1} cm^{-1}) as determined by chronoabsorptometry measurements, which agrees well with previously reported values (5.1 x 10^4 M^{-1} cm^{-1})[129] and therefore should be

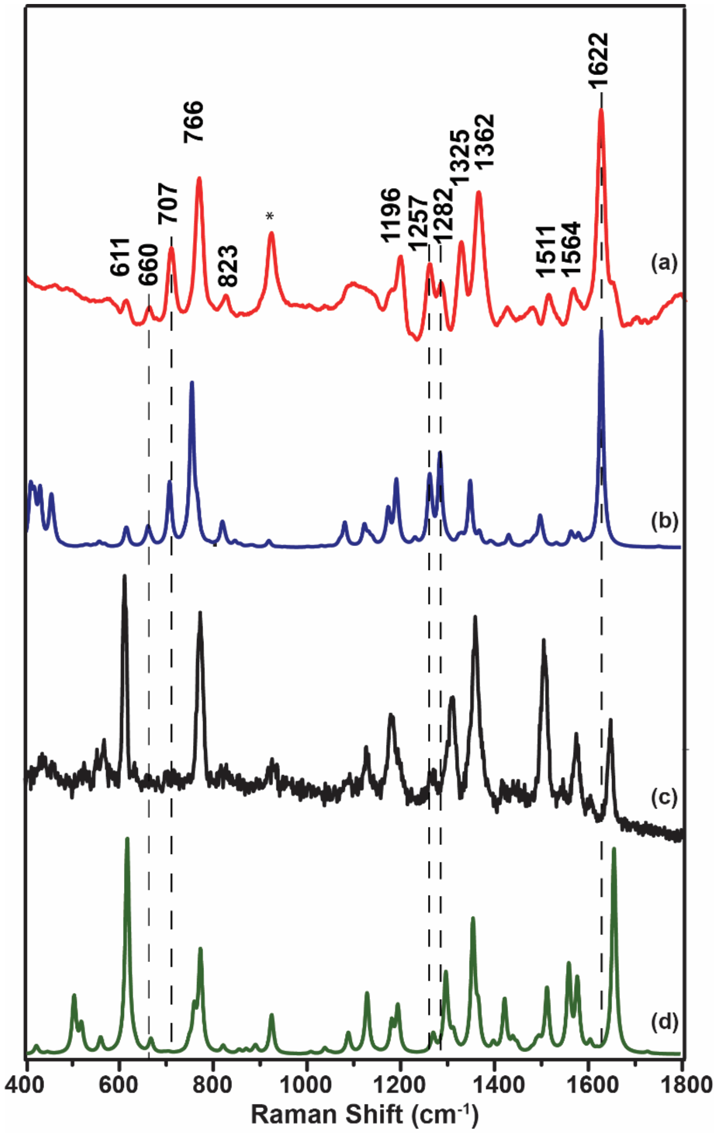

Figure 3.3 Comparison of experimental and theoretical R6G· and $R6G^+$ Raman spectra. (a) Experimental RRS spectrum of 1 mM R6G· in 100 mM TBAP in MeCN, which was acquired in an ITO thin layer cell with an applied potential of -1.2 V (vs Ag QRE). Acquisition parameters: λ_{ex} = 405 nm, P_{ex} = 2 mW, t_{acq} = 120 s (red trace). (b) DFT RRS spectrum of R6G· geometry optimized with B3LYP/6-311G* and spectra were broadened with Lorentzians with a FWHM of 10 cm^{-1} (blue trace). (c) Experimental SERS spectrum of $R6G^+$ acquired from a single AgNP aggregate. λ_{ex} = 532 nm, P_{ex} = 25 mW (grazing incidence), t_{acq} = 5 s (black trace). (d) DFT RRS spectrum of $R6G^+$ (green trace). Dashed lines highlight peaks that are unique to R6G· and will allow distinction from $R6G^+$ by Raman spectroscopy.

detectable with RRS. In order to detect R6G· with RRS, we performed a thin layer spectroelectrochemical measurement to observe the appearance of the R6G neutral radical RRS spectrum. We used 405 nm laser excitation in order to overlap with the R6G neutral radical peak absorbance previously observed at 413 nm (Figure 2.6A). The spectroelectrochemical glassware used consists of a FPT tube, square glass cuvette and valve. (Figure 3.2A) The ITO thin layer cell, Ag QRE and Pt wire CE are suspended in the glassware and extend to the bottom of the glass

Raman Shift (cm^{-1})					
R6G+		**R6G·**		**R6G-amine$^+$**	**R6G-amine·**
Exp. (SERS)	**Theor. (RRS)**	**Exp. (RRS)**	**Theor. (RRS)**	**Exp. (SERS)**	**Exp. (SERS)**
609	615	611	613	609	600
		660	661		
772	772	766	766	771	
	821	823	819		
925	924				
1127	1129			1124	1141
1183	1182	1196	1192	1180	
		1257	1262		1250
1308	1314	1325	1325	1307	
1363	1356	1362	1369	1360	
1509	1514	1511	1506	1501	
1575	1579	1564	1565	1569	1581
1652	1657	1622	1629	1646	

Table 3.1 R6G· RRS, R6G$^+$ and R6G-amine SERS peak positions for experimentally calculated (Exp.) and theoretically predicted (Theor.) spectra.

cuvette. The thickness of ITO thin layer cell is approximately 300 μm, allowing for any solution in the bottom of the cuvette to be drawn up via capillary action, as illustrated in the schematic in Figure 3.2B. The potential of the ITO thin layer working electrode is held at -1.2 V (vs Ag QRE)

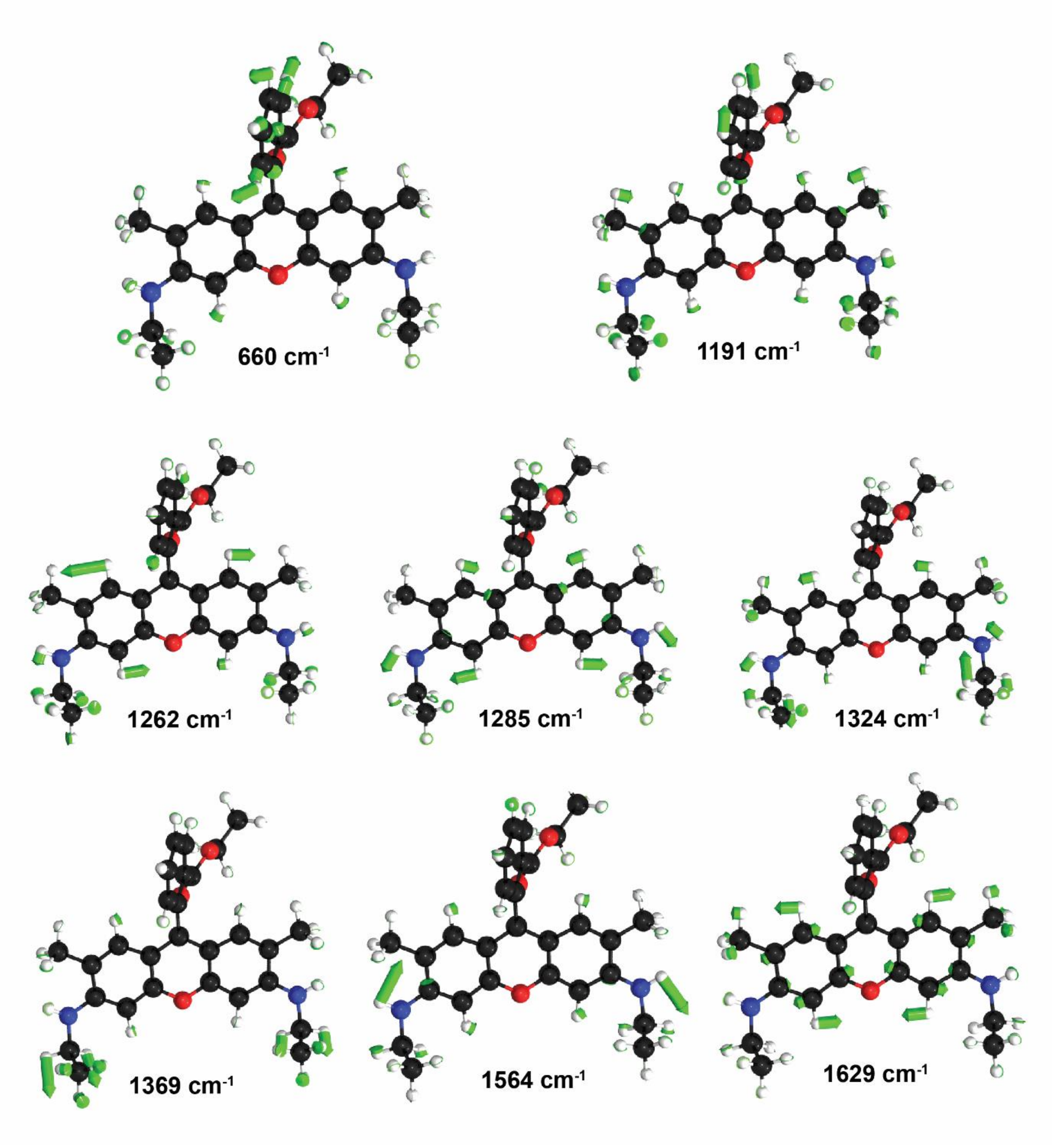

Figure 3.4 Selected eigenvector diagrams for R6G·.

to fully reduce R6G$^+$ to R6G·, and the laser is focused on the ITO in order to acquire RRS spectra. Figure 3.3 shows that the R6G· RRS spectrum (red trace) has excellent agreement with its theoretically predicted spectrum (blue trace); peak values for Figure 3.3 are reported in Table 3.1.

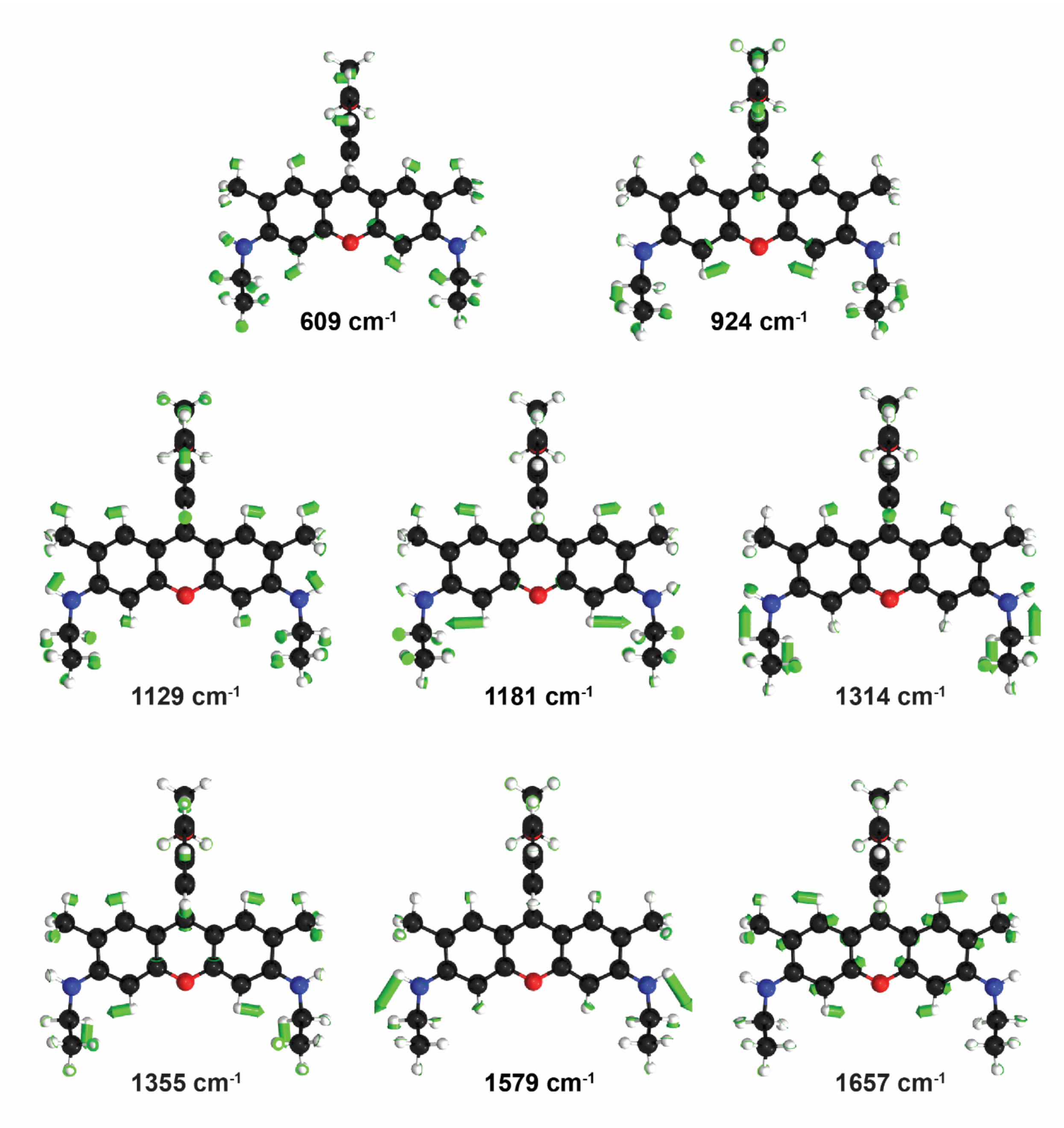

Figure 3.5 Selected eigenvector diagrams for R6G$^+$.

There are distinctive peak shifts and new modes that appear in the resonance Raman spectrum of R6G·. These spectral shifts will be useful to differentiate between the spectra of R6G· and R6G$^+$ in an EC-SERS measurement. New modes appear in the R6G· spectrum centered at 660, 1257 and 1282 cm^{-1} and modes at 925 and 1129 cm^{-1} are lost. Modes centered at 1196, 1325, 1564, and 1622 cm^{-1} are shifted significantly (> 10 cm^{-1}) in the R6G· spectrum relative to the R6G$^+$ spectrum. The mode at 660 cm^{-1} is dominated by phenyl ring vibrations, as shown in the R6G· eigenvector diagrams in Figure 3.4. We also note that position of the pendant phenyl ring in the lowest energy configuration of the R6G· is slightly rotated with respect to the xanthene ring in comparison to the configuration of R6G$^+$, which is most likely the origin of the new 660 cm^{-1} mode. Furthermore, upon reduction of the R6G$^+$, the xanthene ring loses conjugation and therefore, vibrational modes dominated by the xanthene ring are expected to shift. The most significant shift is the 30 cm^{-1} blue shift from 1652 cm^{-1} (R6G$^+$) to 1622 cm^{-1} (R6G·); this mode has been previously calculated to have 89% xanthene character in R6G$^+$.[130] The 1196 cm^{-1} mode is also high in xanthene ring character, which red shifts 16 cm^{-1} compared to the same R6G$^+$ mode. Additionally, the loss of the peaks at 925 cm^{-1} and 1129 cm^{-1} (40% and 28% xanthene character, respectively) in the R6G· spectrum compared to the R6G$^+$ spectrum can also be due to the loss in conjugation of the xanthene ring. Interestingly, the shift in the R6G· 1564 cm^{-1} mode, primarily ethylamine in character, is attributed to a change in symmetry of the vibrational mode.[130] (see Figure 3.4 and Table 3.1)

In conclusion, we have successfully characterized the neutral radical species of R6G with EC-RRS and compared our results to theoretically predicted spectra with excellent agreement. There are unique vibrational modes that are present in R6G·, making it readily differentiable from its oxidized R6G$^+$ form by Raman spectroscopy. Unfortunately, our attempts to detect R6G· by EC-

SERS starting from physisorbed R6G$^+$ have been unsuccessful which we attribute to desorption of the neutral radical species from the AgNP surface. Therefore, the next section addresses covalent tethering of R6G onto SERS-active surfaces in order to circumvent adsorption differences between these two redox forms.

3.3.2. EDC Crosslinking of R6G on Ag Nanoparticles for EC-SERS

3.3.2.1. Electrochemical Characterization of EDC-Coupled R6G on AgNPs

EDC crosslinking requires a primary amine and a carboxylic acid to form an amide bond.(see Figure 3.1) R6G does not have a primary amine or carboxylic acid moiety, so we used an R6G analog, *N*-(2-Aminoethyl)rhodamine 6G-amide bis(trifluoroacetate), which we will refer to as R6G-amine. R6G-amine has a primary amine on the pendant phenyl ring instead of the ester moiety, making it possible to EDC couple to an electroactive surfaces functionalized with a carboxylic acid-containing molecule (e.g. carboxylic acid-terminated alkanethiol, see Figure 3.6). Additionally, the structure of the R6G-amine is not significantly altered compared to R6G, and we therefore expect the SERS response to be similar to R6G used in previous experiments.

Prior to performing SERS measurements, EDC-coupled R6G AgNPs on ITO were prepared using Sample Preparation I and electrochemically characterized with CV to ensure the R6G-amine exhibited well-behaved surface electrochemistry. We performed surface CVs on a sample prepared

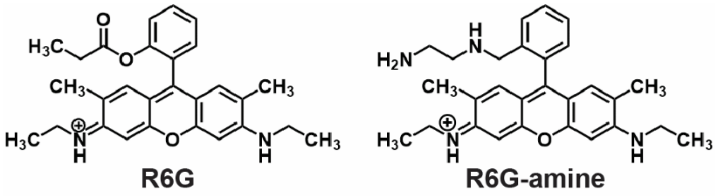

Figure 3.6 Molecular structures of R6G and R6G-amine.

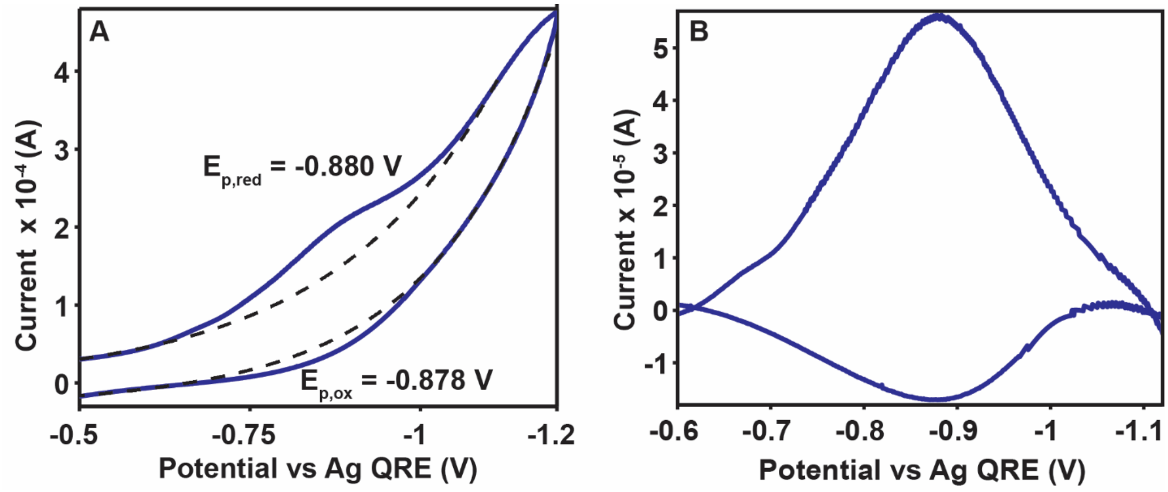

Figure 3.7 Cyclic voltammetry of EDC-crosslinked R6G on AgNPs on ITO. A) MPA, EDC and sulfo-NHS added to AgNPs with R6G-amine (blue trace) and without R6G-amine (black dashed trace). Scan rate = 100 mV/s. B) The blue trace in A) was fit to an exponential and RC-term baseline, which was then subtracted from CV of EDC-crosslinked R6G on AgNPs from A) to yield the displayed CV.

with and without the final R6G-amine incubation step. Figure 3.7A shows the resultant CVs, where $E_{p,red}$ = -0.880 V and $E_{p,ox}$ = -0.878 V for the CV corresponding to R6G addition. For ease of fitting the cathodic and anodic current peaks, we performed an exponential baseline correction of the CV with EDC crosslinked R6G-amine. The resultant CV is shown in Figure 3.7B. The difference between the reduction potentials between the EDC-coupled R6G and previously measured CVs of AgNPs on ITO (Figure 2.1) are most likely due to the presence of thiolated molecules on the AgNP surface, which in turn effects redox potentials. This can also introduce solution resistance effects, as observed previously and discussed in Chapter 2. (Figure 2.1) We note that there are no peaks in the sample without R6G (black dashed trace, Figure 3.7A), simply a background capacitive feature characteristic of surface CVs, indicating the success of the EDC crosslinking reaction. The peak separation of the EDC-coupled R6G surface CV is 2 mV, which strongly indicates a well-behaved, surface-bound species.[110,131-133] The peak widths of the cathodic and anodic waves at half height are greater than what is expected for a one-electron reaction (~90 mV).[110] This can be attributed to interactions between adjacent R6G molecules tethered to the surface as well as heterogeneities between surface interactions.[78] We then calculated the R6G-amine surface coverage using Equations 3.1 and 3.2:

$$Q_c = \frac{1}{\nu} \int_{E_0}^{E_\tau} i_c dE \qquad \text{(Equation 3.1)}$$

where Q_c is the cathodic charge, ν is the CV scan rate, E_τ is the final potential and E_0 is the initial potential, and i_c is the cathodic current. Integrating Equation 3.1 yields Equation 3.2:

$$\Gamma = \frac{Q_c N_A}{nFA} \qquad \text{(Equation 3.2)}$$

where Q_c is the cathodic charge, N_A is Avogadro constant, *n* is the charge passed in the ET reaction being studied, *F* is Faraday's constant and A is the area of the electrode. To calculate the cathodic and anodic charge, we first corrected for the capacitive background in the surface CV. Q_c was determined from the integrated area under the cathodic peak in Figure 3.7B and was calculated to be 1.29×10^{-4} C; Q_a, or the anodic charge, was calculated to be 3.72×10^{-5} C. The discrepancy between Q_c and Q_a indicates how sensitive the system is to oxygen or water, which can react with the reduced R6G neutral radical species and render the one-electron transfer irreversible. If we approximate the area of the electrode to be 2 cm^2 and n = 1, Γ_c is 4.03×10^{14} molecules/cm^2. This value is consistent with previous calculations for determining monolayer surface coverages, where 10^{14} molecules/cm^2 was the upper limit of monolayer coverage of NB on ITO[69] and 4.64×10^{14} molecules/cm^2 was the high coverage limit of ferrocene-terminated alkanethiol.[78] We note that our calculation is an overestimation of surface coverage due to the added AgNPs on the ITO surface and therefore higher total surface area of the electrode. The CV measurements confirm that R6G amine is covalently bound to the NP surface and is electrochemically active, and it should be readily observable with SERS.

3.3.2.2. Heterogeneous EDC Crosslinking: AgNPs on ITO and AgFONs

After characterizing the electrochemistry of EDC-coupled R6G on AgNPs, we then analyzed samples prepared via Sample Preparation I with SERS. This was done to ensure that the SERS response of the EDC coupled R6G-amine is not significantly different from that of R6G physisorbed onto AgNPs, previously used in the EC-SMSERS experiments in Chapter 2. Figure 3.8 shows the SERS spectra of R6G-amine heterogeneously EDC-coupled with MPA compared to physisorbed R6G on AgNPs.

Table 3.1 includes the corresponding peak positions for comparison purposes. Most vibrational modes of the EDC crosslinked R6G-amine are in strong agreement with physisorbed R6G, however, there are peak shifts in the 1300-1600 cm^{-1} region. We attribute this to the presence of a new amide mode from the EDC crosslinking reaction. Despite acquiring this reference spectra, acquiring many high quality SERS spectra from the sample was very challenging due to strong fluorescent backgrounds throughout the sample and low density of SERS-active AgNP aggregates. Additionally, we were not able to acquire SERS spectra from an AgNP sample prepared using MHA (not shown). Therefore, using this type of sample preparation (heterogeneous EDC crosslinking) to collect a statistically significant number of SMSERS spectra would be extremely challenging. We attribute the lack of high-quality SERS spectra from samples prepared by Sample Preparation I to the fact that EDC-coupled R6G-amine molecules are located on SERS hot spots at a low yield since Ag particles were pre-aggregated prior to deposition on the ITO surface.

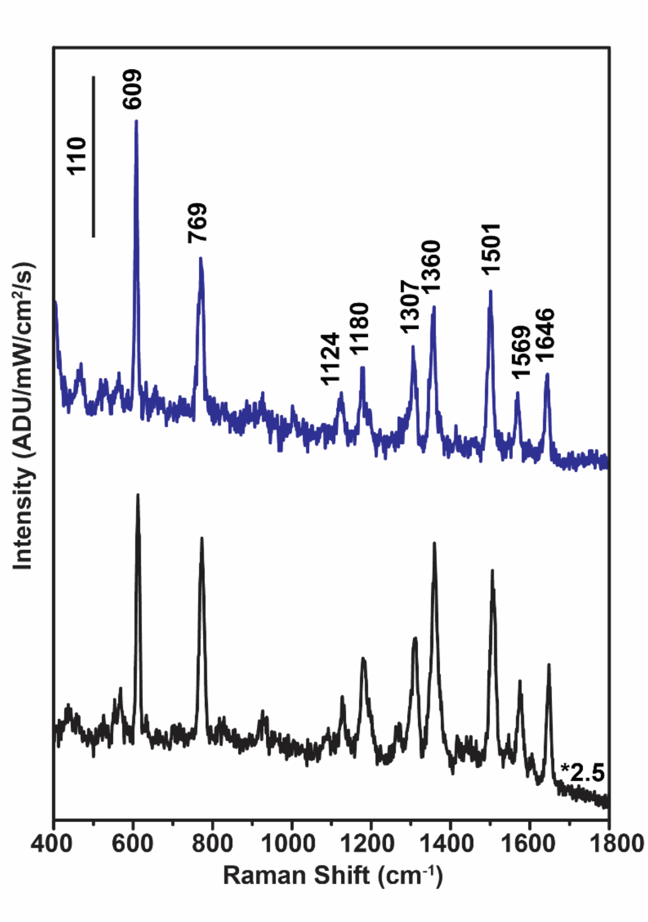

Figure 3.8 SERS of R6G-amine$^+$ using a heterogeneous EDC crosslinking procedure. The acquired spectra of R6G-amine$^+$ on AgNPs (blue trace) was compared to physisorbed R6G$^+$ on AgNPs (black trace). R6G SERS acquisition parameters: λ_{ex} = 532 nm, P_{ex} = 25 mW (grazing incidence), t_{acq} = 5 s. R6G-amine SERS acquisition parameters: λ_{ex} = 532 nm, P_{ex} = 15 mW (grazing incidence), t_{acq} = 3 s.

Additionally, the large fluorescent backgrounds (not shown) could also be due to R6G-amine molecules potentially bound to the ITO surface and away from SERS active sites.

We confirmed that the SERS spectra, as well as fluorescent background, of R6G-amine$^+$ observed originated from the successful linkage of R6G-amine to the Ag surface by performing the same heterogeneous EDC-coupling procedure on an Ag film over nanosphere (AgFON) SERS substrate. FONs are highly enhancing SERS substrates with a high density of hot spots, as described in Chapter 1. We therefore expect to observe SERS signal if the R6G-amine is bound to the AgFON surface. We performed the EDC crosslinking reaction on an AgFON optimized for 532 nm excitation[11] with both MPA and MHA; and we found that both yield strong SERS signals sitting on top of a fluorescent background, as shown in Figure 3.9. Because the R6G-amine is not directly adsorbed to the AgFON surface, it is possible that the fluorescence background is originating from a surface-enhanced fluorescence (SEF) effect. Like SERS, SEF is highly distance dependent, and is quenched within ~1 nm of the enhancing substrate due to non-radiative emission to the metal particle.[134] We therefore expect to observe more pronounced fluorescence from the MPA sample, which is indeed the case. Moreover, the MPA EDC crosslinked R6G-amine signal

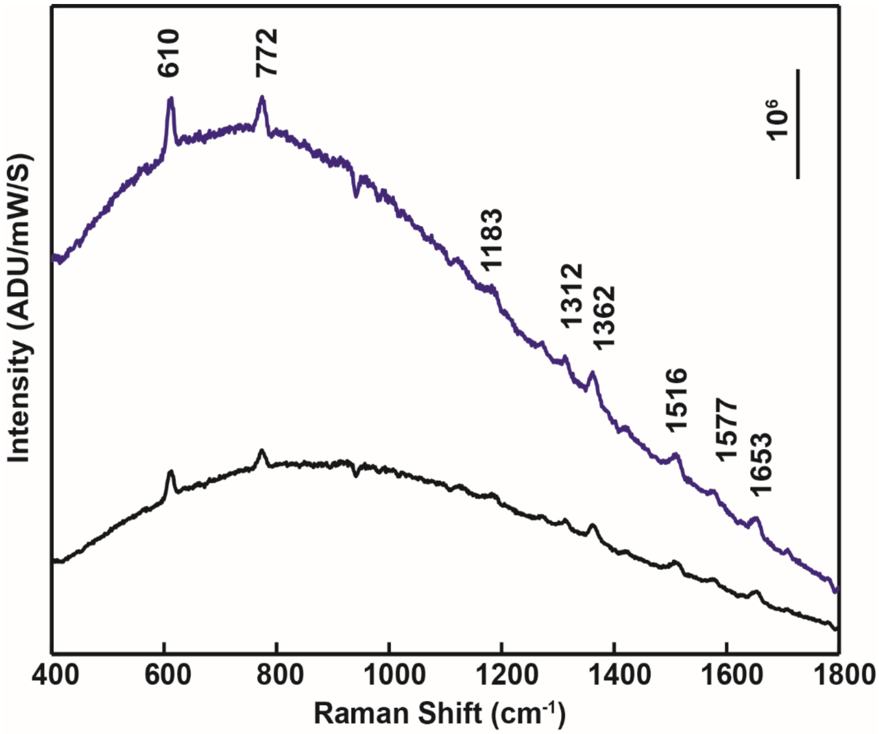

Figure 3.9 Representative SERS spectra from heterogeneous EDC coupling of R6G-amine$^+$ on an AgFON. SERS spectra of EDC-coupled R6G-amine$^+$ using MPA (blue trace) and MHA (black trace) on an AgFON substrate. Acquisition parameters: λ_{ex} = 532 nm, P_{ex} = 3 μW (40x objective, epi illumination), t_{acq} = 5 s.

is approximately two times more intense than that of the MHA, which is expected due to the distance dependence of SERS. This result indicates the importance of using a short-chain alkanethiol when coupling molecules to the surface in order to obtain the maximum SERS signal, especially for SMSERS studies. Now that we were successfully able to confirm surface-bound R6G-amine on AgFONs with SERS, the current experimental limitations in the framework of performing EC-SMSERS studies led us to develop a novel, optimized EDC crosslinking procedure on AgNPs for EC-(SM)SERS studies.

3.3.2.3. Homogeneous EDC Crosslinking of R6G on AgNPs

An alternative sample preparation strategy, which we refer to as homogeneous EDC crosslinking, was developed in order to minimize background fluorescence and to increase the density of SERS-active AgNP aggregates. There are two advantages to the "homogeneous" EDC crosslinking procedure in comparison to the heterogeneous method: first, washing steps performed between each reaction step minimizes excess of reactants in solution, and second, the colloids are dropcasted on the ITO *after* EDC crosslinking, avoiding direct binding of R6G-amine to the ITO

Sample:	**S1**	**S2**	**S3**	**S4**	**S5**	**S6**	**S7**	**S8**	**S9**	**S10**
Thiol	MPA	MHA	MPA	MHA	MPA	MPA	MHA	MHA	MPA	MPA
Conc. thiol (mM)	1	1	1	1	10	10	10	10	1	1
Post-thiol wash step	Y	Y	Y	Y	Y	Y	Y	Y	N	N
Method II-A			x	x		x		x		x
Method II-B	x	x			x		x		x	
Mean 610 cm^{-1} Peak intensity (ADU/mW/s/cm^2)	-	-	38	-	41	66	-	-	-	32

Table 3.2 Sample preparation conditions under study for homogeneous EDC crosslinking reaction.

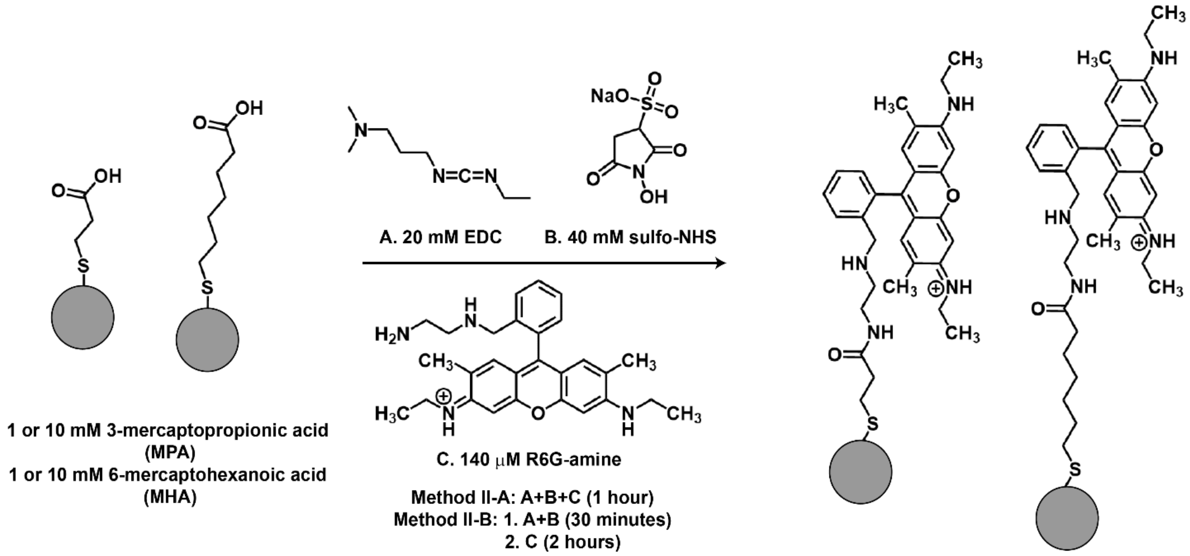

Figure 3.10 Schematic (not to scale) of homogeneous EDC-crosslinking of R6G performed on AgNPs in solution.

and maximizing the R6G-amine molecules located in nanoparticle hot spots. We optimized the homogeneous crosslinking procedure by testing two thiolated acid concentrations and two different EDC reagent/R6G-amine addition steps, as highlighted in Table 3.2 and Figure 3.10. We also investigated the influence of washing steps after carboxylic acid-terminated alkanethiol addition in order to evaluate the effect of unreacted reagent excess in solution (S9 and S10 did not have a washing step, see Experimental section, Method II-A and II-B).

For SERS measurements, samples prepared with the MPA thiol and washing steps (S3, S5 and S6,Table 3.2) provided the best results. These specific samples resulted in a high density of SERS-active AgNP aggregates on the ITO that had minimal fluorescent background and were stable over time. Sample SERS spectra are shown in Figure 3.11A and average 610 cm^{-1} peak intensities are reported in Table 3.2. The highest average signals were obtained from the samples prepared with 10 mM MPA, which is most likely due to the higher density available sites for EDC reaction to occur, and therefore more R6G EDC crosslinked to the AgNPs. Samples prepared by S5 and S6 were prepared with the same MPA concentration but different timing for R6G-amine addition with respect to EDC reagents and we observe that the SERS signal intensity is greater for

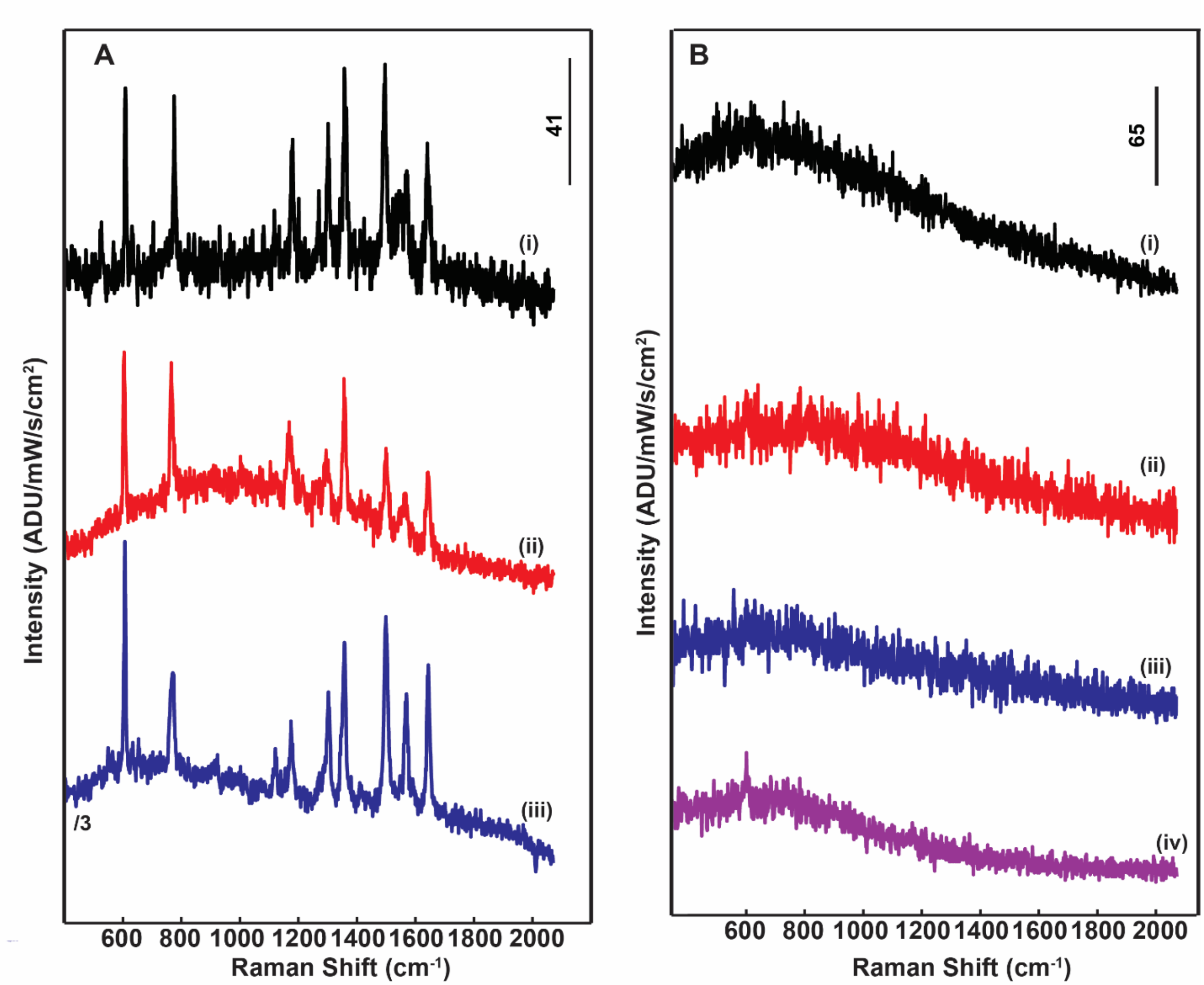

Figure 3.11 Representative SERS spectra of R6G-amine$^+$ homogeneously EDC-crosslinked on AgNPs. A) Samples with prepared that exhibited stable, consistent R6G-amine$^+$ SERS signal. (i) Representative SERS spectrum from sample S3. λ_{ex} = 532 nm, P_{ex} = 12.7 mW (grazing incidence), t_{acq} = 3 s. (ii) Representative SERS spectrum from sample S5. λ_{ex} = 532 nm, P_{ex} = 12.7 mW (grazing incidence), t_{acq} =10 s. (iii) Representative SERS spectrum from sample S6. λ_{ex} = 532 nm, P_{ex} = 15.1 mW (grazing incidence), t_{acq} = 5 s. B) Samples prepared that exhibited weak or no SERS signal of R6G-amine$^+$ (i) Representative spectrum from sample S1. λ_{ex} = 532 nm, P_{ex} = 12.1 mW (grazing incidence), t_{acq} = 3 s. (ii) Representative spectrum from S4. λ_{ex} = 532 nm, P_{ex} = 12.7 mW (grazing incidence), t_{acq} = 3 s. (iii) Representative spectrum from S8. λ_{ex} = 532 nm, P_{ex} = 12.7 mW (grazing incidence), t_{acq} = 3 s. (iv) Representative spectrum from S10. λ_{ex} = 532 nm, P_{ex} = 12.7 mW (grazing incidence), t_{acq} = 3 s.

the simultaneous addition of the EDC reagents and R6G-amine. One origin for the difference in average SERS signal intensity between S5 and S6 is that some of the EDC can react with water and is rendered inactive prior to the addition of R6G-amine in Method II-B. We observed relatively

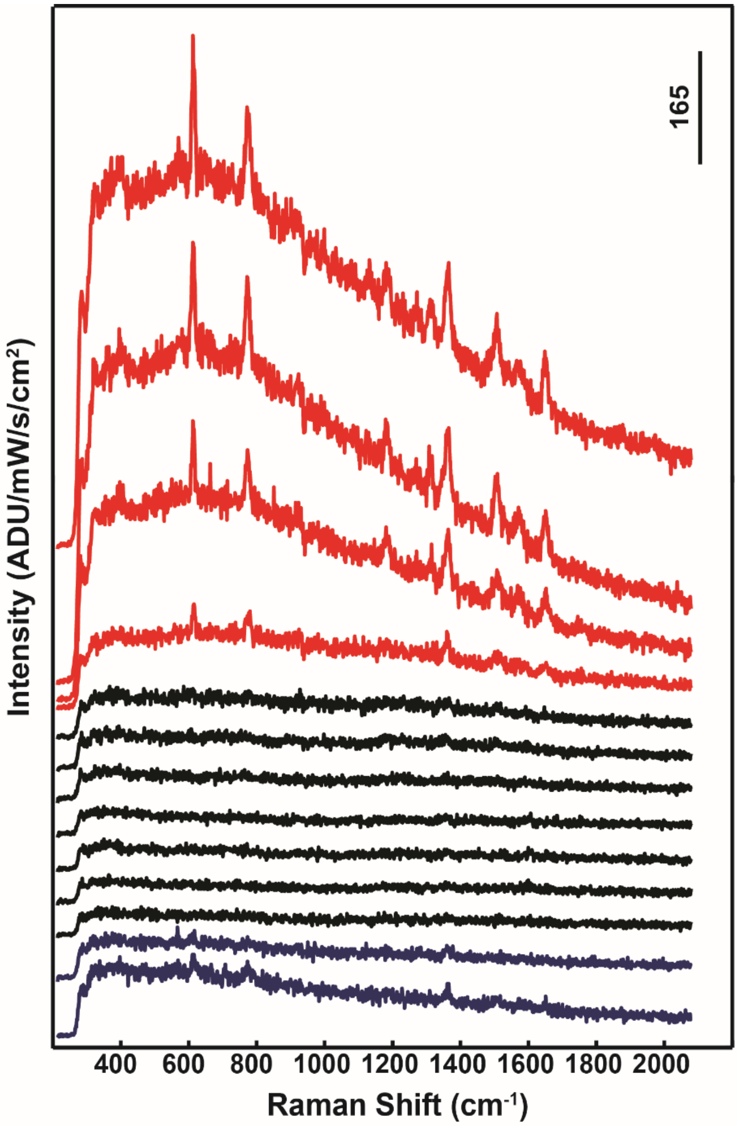

Figure 3.12 EC-SERS of R6G-amine$^+$ homogeneously EDC-crosslinked onto AgNPs. Samples were prepared by preparation method II-B, S6 (Table II). The potential is stepped in 0.1 V steps from -0.6 V to -1.2 V to -0.6 V, with the first red spectrum at -0.6 V as the first potential step. R6G-amine$^+$ is fully reduced to R6G-amine· at -1.0 V (first black trace) and is oxidized at -0.7 V (dark blue trace) R6G-amine SERS acquisition parameters: λ_{ex} = 532 nm, P_{ex} = 15 mW (grazing incidence), t_{acq} = 3 s.

weaker and less consistent SERS signals from the unwashed MPA sample (S10) as illustrated in Figure 3.11B, which could originate from the EDC reagents reacting with unbound MPA in the solution instead of surface-bound MPA. Interestingly, we were not able to obtain SERS signal from the samples prepared with the MHA thiol, as shown in representative spectra in Figure 3.11B (S1, S2, S4, S7-S9). We attribute the lack of SERS signal in MHA samples to the distance dependence of SERS.

Based on our experimental results, we concluded that S6 appeared to be an optimized homogeneous EDC crosslinking procedure, and we performed EC-SERS at 532 nm with samples

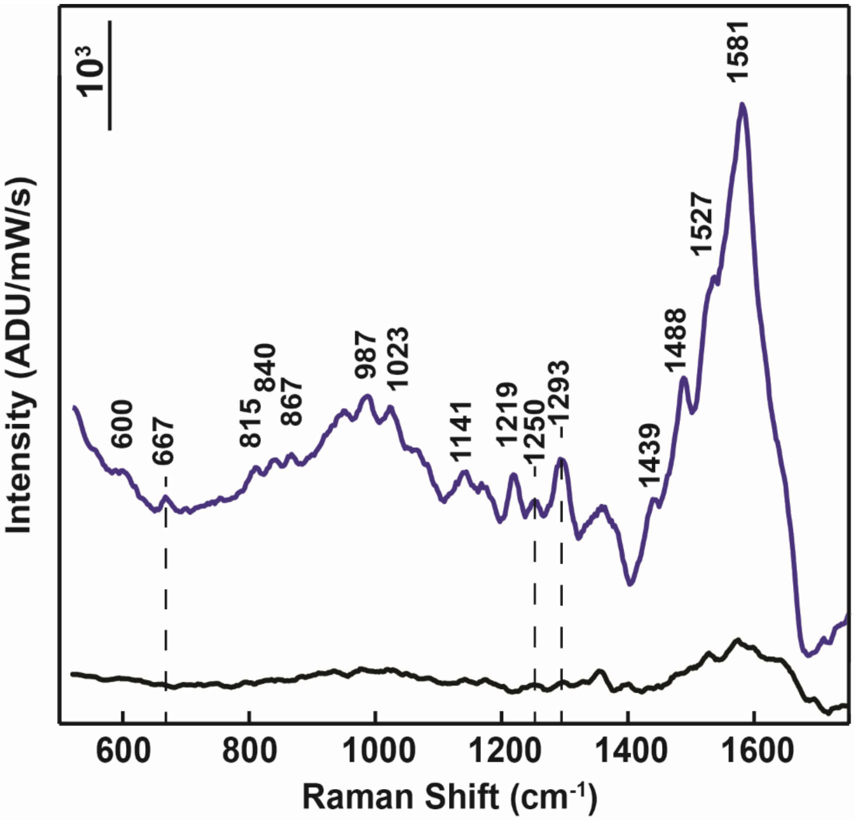

Figure 3.13 Representative SERS spectrum of R6G-amine· with 405 nm excitation. Spectra were acquired at an applied potential of -0.6 V (black trace) and -1.0 V (blue trace). Sample prepared using homogeneous EDC crosslinking procedure (sample preparation S6, Table II). Dashed lines indicate peaks unique to R6G-amine•. Acquisition parameters: λ_{ex} = 405 nm, 100x objective, P_{ex} = 90 µW (epi illumination), t_{acq} = 2 s.

prepared with the same conditions as S6 (Figure 3.12). The SERS signal dependence of a single AgNP aggregate versus applied potential behaved similarly to that of R6G physisorbed on AgNP aggregates, as described in Chapter 2. As shown in Figure 3.12, the SERS signal is lost at -1.0 V, indicating reduction of R6G-amine$^+$ to R6G-amine·, and returns at -0.7 V, indicating oxidation of R6G-amine· to R6G-amine$^+$. The R6G-amine$^+$ signal exhibits sharp peak linewidths compared to known high-coverage R6G SERS spectra (Figure 2.6B), indicative of few to single-molecules present on the AgNP aggregate.[135] Upon reoxidation of R6G-amine· to R6G-amine$^+$, we find that the return signal is not as intense at the initial R6G-amine$^+$ signal. Because the R6G-amine molecules are covalently tethered to the surface, it is unlikely the signal loss is from molecular diffusion. The loss in signal intensity more likely originates from potential-induced structural change of the AgNP aggregate, previously observed in EC-SERS studies.[111,112] Since with these measurements we were able to observe EC-SERS behavior at 532 nm, comparable to physisorbed R6G on AgNPs, we then attempted to observe the SERS spectrum of the reduced R6G-amine· species with 405 nm excitation from the same sample. Figure 3.13 shows a spectrum taken from a single AgNP aggregate at applied potentials of -0.6 and -1.0 V. The peaks in the 405 nm excitation -1.0 V spectrum are listed in Table II on R6G-amine· column. We observe the appearance of peaks at 667, 1250 and 1293 cm^{-1} are in close agreement with the R6G· experimental RRS peaks at 660, 1257, and 1282 cm^{-1}. Slight discrepancies between the R6G RRS and R6G-amine· SERS are expected due to the presence of the amide group and the secondary amine on the pendant phenyl ring. Additionally, we observe a broad feature in the 1400-1600 cm^{-1} region, which we attribute to carbon background formation. We note that this is the first demonstration of detection of a rhodamine radical species with SERS, and the first demonstration of detecting both redox species of a molecule at near-single molecule levels using a dual-wavelength SERS approach. Overall, our results demonstrate the feasibility of monitoring both redox states with EC-SERS.

3.4. Conclusions and Future Work

In this work, we present the spectroscopic characterization of the reduced form of R6G, the R6G neutral radical, and have optimized a new method for preparing SERS-active nanoparticle aggregates using EDC crosslinking. We find that both the electrochemistry and SERS response of the EDC-coupled R6G-amine is not drastically different from its physisorbed R6G analog and we have successfully optimized a "homogeneous", solution-phase EDC coupling procedure with AgNPs. We then use our optimized EDC coupling procedure to demonstrate the first SERS detection of the R6G neutral radical species using a dual-wavelength SERS approach. Future work will implement an EDC coupled AgNP sample to perform EC-SMSERS experiments, specifically for simultaneous dual-wavelength EC-SERS on a single AgNP aggregate. We will also address statistically rigorous SMSERS detection, where we will prove SMSERS using two EDC coupled bianalyte molecules that are structurally similar molecules with unique SERS spectra (e.g. rhodamine B and rhodamine B isothiocyanate).

Chapter 4. Rapid Identification and Quantification of Intravenous Therapy Drugs using Normal Raman Spectroscopy and Electrochemical Surface-Enhanced Raman Spectroscopy

4.1. Introduction

There is a critical need to accurately monitor intravenous (IV) therapy drugs to prevent adverse drug events (ADEs), which include errors such as incorrect drug type prescribed for the patient or drug mislabeling, incorrect concentration, and simultaneous delivery of incompatible drugs. The number of reported ADEs in infusion pumps totaled 56,000 in a 4 year period, 710 of which lead to death.[136] The primary means of administering drugs in infusion pump lines is preprogrammed drug libraries that specify dose limits of particular medications.[137] Although this method is useful for controlling infusion rates, it does not have the ability to accurately identify and quantify the medication administered or to determine whether it is correct. While it is possible to identify and quantify administered drugs using reporter systems such as functionalized nanoparticles[138-140], reporter systems typically cannot be introduced into a patient's IV line due to safety concerns. Therefore, non-invasive techniques are required to monitor administered IV drugs. There is also a need to accurately and rapidly identify the concentrations of compounded solutions; errors in drug compounding of a steroid drug lead to a major meningitis outbreak in 2012.[141,142] Raman spectroscopy is an ideal candidate for both in-line drug sensing and detecting compounding errors in drug solutions, as most drugs have a unique Raman spectrum and water does not have a strong Raman signal. Additionally, the cost of handheld Raman spectrometers has decreased significantly in the past few years, making the use of Raman spectroscopy highly feasible in a clinical setting.

Raman scattering occurs when scattered photons are shifted in energy from the incident photons; the difference in incident and scattered photon energy corresponds to a specific molecular vibration. As noted above, Raman spectroscopy is an ideal technique for detecting drugs because of its high molecular specificity and linear correlation of signal intensity to analyte concentration. Additionally, water does not have a strong Raman profile, making the technique ideal candidate for acquiring measurements of solution-phase analytes. Although Raman is a powerful technique, clinical analyte concentrations are often too low to be detected using normal Raman spectroscopy (NRS). In these cases, very low concentrations can be detected by implementing a phenomenon known as surface-enhanced Raman spectroscopy (SERS), first reported by Jeanmaire and Van Duyne in 1977.[2] The origin of the high enhancements of SERS stems from the excitation of a localized surface plasmon resonance (LSPR) of a noble metal nanoparticle substrate, which in turn generates a strong electromagnetic field near the surface. It has been demonstrated that the SERS signals of ensemble-averaged molecules exhibit enhancements up to eight orders of magnitude compared to the normal Raman signal.[143,144] In recent years, SERS has established itself as a powerful method with unparalleled sensitivity and the lowest known limits of detection. Because of this, SERS has been used in applications such as bacteria sensing,[51,145] dye detection for art conservation,[146] and anthrax detection.[16,17]

There has been a recent push to develop robust, highly enhancing SERS-active platforms, which range from nanoparticle aggregates to lithographically fabricated substrates.[6,144] One lithography-based device, coined film over nanosphere (FON), is a highly reproducible, low-cost SERS platform that was developed in the Van Duyne group. FONs are relatively low-cost to produce, have enhancement factors on the order of 10^5-10^8 and have predictable SERS enhancement with less than 10% SERS enhancement factor (EF) variability across a 25 mm area.[11]

In order to detect analytes with SERS, the target analyte must either sufficiently bind to the SERS substrate or be in close proximity (< 3 nm) from the enhancing surface. Recent work from our group highlights the importance of the distance dependence of SERS for molecular sensing: Masango et al. applied layers of Al_2O_3 via atomic layer deposition (ALD) on an AgFON substrate. When fitting the SERS response versus Al_2O_3 thickness, they found that the SERS signal had a two-term distance dependence. The SERS intensity of the CH_3 bending mode in trimethylaluminum, an Al_2O_3 ALD precursor, was found to drop by 20% with an Al_2O_3 thickness 0.7 nm deposited on the AgFON surface and by 7% with 3 nm Al_2O_3, which was further corroborated using DFT calculations.[147] These findings imply that in order to obtain the maximum sensitivity in SERS sensing, the target analyte should be bound directly to the SERS-active surface, if possible. In most sensing applications, SERS substrates are tailored to attract specific analytes of interest, which has been done for detection of analytes such as chloride ions[148,149] and glucose[150-152]. However, the presence of a capture layer will inherently decrease the SERS signal obtained, and ultimately decrease the sensitivity as dictated by the distance dependence.

Alternatively, electrochemical-SERS (EC-SERS) is a label-free and completely non-invasive SERS detection method that can be utilized in cases where the analyte does not bind to the SERS substrate. In this technique, the potential applied to the substrate can be controlled to electrostatically attract the analyte of interest to the SERS-active surface. When detection is completed, the applied potential can be changed to remove the analyte and re-use the substrate. Using EC-SERS for molecular sensing also means that the molecule is in direct contact with the surface, and the maximum signal enhancement can be achieved. EC-SERS has previously been used to detect molecules such as dopamine in micromolar concentration solutions at neutral pH.[153] Recent work from Brosseau and coworkers has demonstrated the use of a low-cost EC-SERS setup to detect uric acid in synthetic urine samples at clinically relevant concentrations on an Au/Ag multilayer nanoparticle working electrode.[154,155]

The over-arching goal of this work is to develop a non-invasive sensing platform to rapidly monitor drug identity and concentration in a clinical setting or for drug compounding using the molecular specificity and extreme mass sensitivity and non-invasive nature of Raman spectroscopy. Viability in clinical settings also signifies relevance in drug compounding settings, which deal with drugs in higher volumes, equal or higher concentrations, and fewer instrumentation and financial constraints. In this paper, we demonstrate two distinct approaches to identify clinically relevant analytes. First, we use NRS with a handheld device to detect and quantify gentamicin, an antibiotic commonly used to treat a wide variety of Gram-negative and Gram-positive bacterial infections. We then use a label-free EC-SERS approach to detect dobutamine, a catecholamine that is commonly administered after heart surgery, which does not have detectable NRS signals in the clinical range and does not bind strongly to SERS substrates.

4.2. Experimental Details

Chemicals. Hydrogen peroxide solution 30% (H_2O_2), ammonium hydroxide solution 28-30% (NH_4OH), sodium hydroxide (NaOH), 1 N hydrochloric acid (HCl), and gentamicin 50 mg/mL standard solution in deionized water were purchased from Sigma-Aldrich and used without further modification. Gentamicin in 0.9% sodium chloride IV bag solution (2 mg/mL) and dobutamine IV bag solutions in 5% dextrose and 1% sodium bisulfite (1, 2 and 4 mg/mL, pH = 3.5) were received from Baxter; gentamicin dilutions were prepared in 0.9% sodium chloride and dobutamine dilutions were prepared in MQ water. MQ water with a resistivity higher than 18.2 MΩ cm was used in all preparations.

FON Fabrication. 25 mm diameter circular polished Si wafers were purchased from Wafernet, Inc. The Si wafers were first cleaned with Piranha solution for 30 minutes (3:1 H_2SO_4:H_2O_2), rinsed copiously with MQ H_2O and then treated with 5:1:1 H_2O:H_2O_2:NH_4OH for 45 minutes to render the surface hydrophilic. The wafers were stored in MQ H_2O prior to use. 540 nm SiO_2 microspheres (Bangs Laboratories, Indiana) were diluted to 5% with MQ water and 10-12 µL were dropcasted onto the Si wafer and allowed to dry. After drying, 150 nm Au was thermally deposited on the FON mask surface at a rate of 1 Å/s under vacuum conditions (~10^{-6} Torr) (PVD-75, Kurt J. Lesker).

Bulk Electrochemistry. Bulk electrochemical measurements were performed in a capped scintillation vial. A polished Au disc electrode was utilized as the working electrode and was submerged in solution approximately 1 cm above the Pt wire counter electrode. The reference potential was determined by a 2 mm outer diameter leak-free Ag/AgCl reference electrode

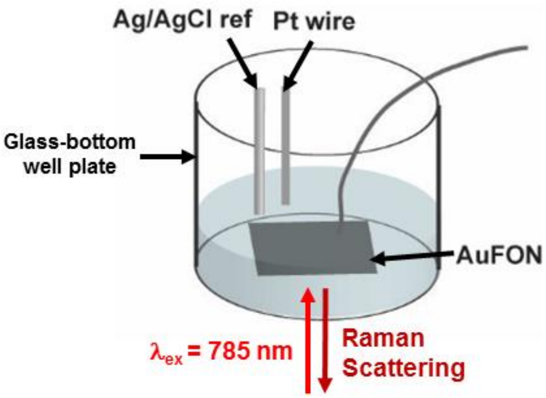

Figure 4.1 Experimental schematic for EC-SERS measurements.

(Harvard Apparatus). Electrochemical measurements were performed using a CH Instruments potentiostat (CHI660D)

EC-SERS Sample Preparation. AuFON working electrodes were prepared by first cutting the as-deposited FON into 1 cm^2 pieces with a diamond scribe pen. A 0.25 mm diameter Ag wire (Alfa Aesar) was then attached to the FON using conductive Ag epoxy (Ted Pella) to allow for electrical contact with the AuFON. A 2 mm diameter leak-free Ag/AgCl electrode (Harvard Apparatus) and 0.5 mm diameter Pt wire (Alfa Aesar) were utilized as the reference electrode and counter electrode, respectively. A #1.5 glass coverslip bottom well plate (Mattek Corporation) was used as the cell for EC-SERS measurements, as illustrated in the schematic in Figure 4.1. Approximately 1.5 mL of the solution of interest was pipetted into a well and the electrodes were suspended in the solution of interest using a rubber septum. The potential was controlled using a CH Instruments potentiostat (CHI660D).

Instrumentation. LSPR measurements were acquired using a fiber light spectrometer (Ocean Optics), with a flat Au 150 nm film deposited on a cleaned glass coverslip as a flat mirror reference. Handheld Raman measurements were performed using a CBEx™ handheld Raman spectrometer with 785 nm excitation, 50 mW power and various acquisition times. Tabletop normal Raman measurements were performed using a 785 nm laser (Innovative Photonic Solutions); the Raman scattered light was collected and redispersed onto a LS785 spectrometer (Princeton Instruments) with a 600 groove/mm grating blazed at 750 nm. EC-SERS measurements were performed using an inverted microscope (Nikon Eclipse Ti-U), where the 785 nm laser excitation was focused onto the sample and the scattered light was collected using a 20x objective (Plan Fluor, NA = 0.45, Nikon). The laser light was filtered using a 785 nm long pass filter (Semrock) and focused onto a

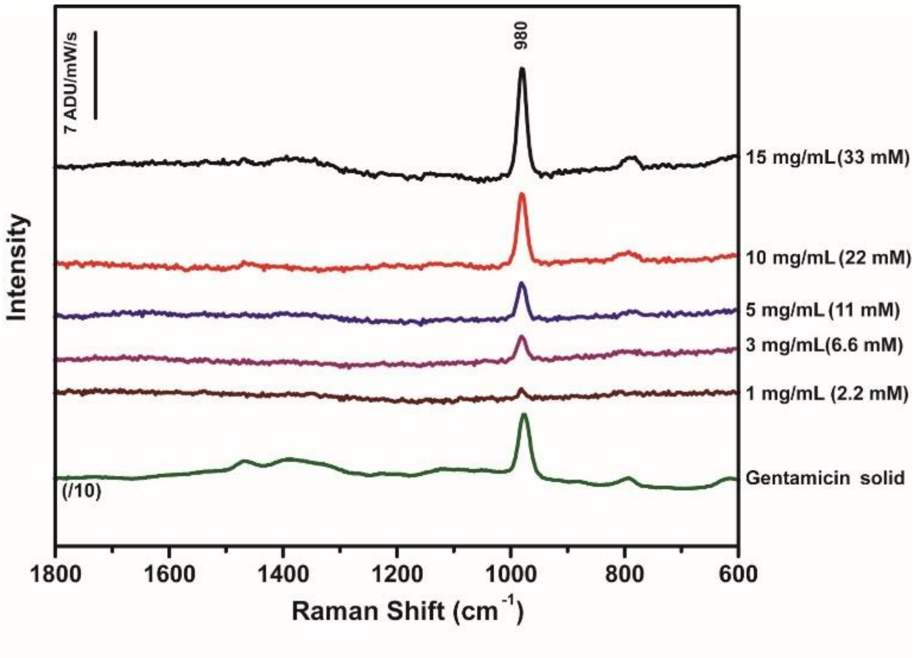

Figure 4.2 NRS of gentamicin in MQ H_2O at various concentrations.
Acquisition parameters: λ_{ex} = 785 nm, P_{ex} = 50 mW, t_{acq} = 5 s.

1/3 m spectrometer (SP2300, Princeton Instruments). The focused light was then dispersed (600 groove/mm grating, 1000 nm blaze) and focused onto a liquid nitrogen-cooled CCD detector (Spec10:400BR, Princeton Instruments). LSPR and Raman spectra were processed with OriginLab 8.0 and MATLAB.

4.3. Results and Discussion

4.3.1. Normal Raman Spectroscopy of Gentamicin

The primary model drug used for antibiotic detection and quantification via NRS in this work is gentamicin. Gentamicin is a heat-stable protein synthesis inhibitor used to treat Gram-negative and *Staphylococcus* bacterial infections and in orthopedic surgery. It is typically administered intravenously at 2 mg/mL (4.3 mM) and at pH 3.0-5.5.[156] We analyzed the NRS spectra for nine reference gentamicin solutions ranging in concentration from 0.5 – 50 mg/mL

(1.12-112 mM) using both a macro Raman instrumental setup and the CBEx™ handheld Raman spectrometer. Each data point presented is an average of five acquired spectra at an acquisition time of 5 seconds each. The most prominent spectral features of gentamicin were a major mode at 980 cm^{-1} and a less intense mode at 790 cm^{-1} (Figure 4.2); we generated NRS linear profiles of concentration versus integrated signal intensity using the 980 and 790 cm^{-1} modes.

Prior to acquiring NRS spectra of gentamicin using the CBEx™ handheld Raman spectrometer, we compared the spectral resolution of the CBEx™ to the macro Raman

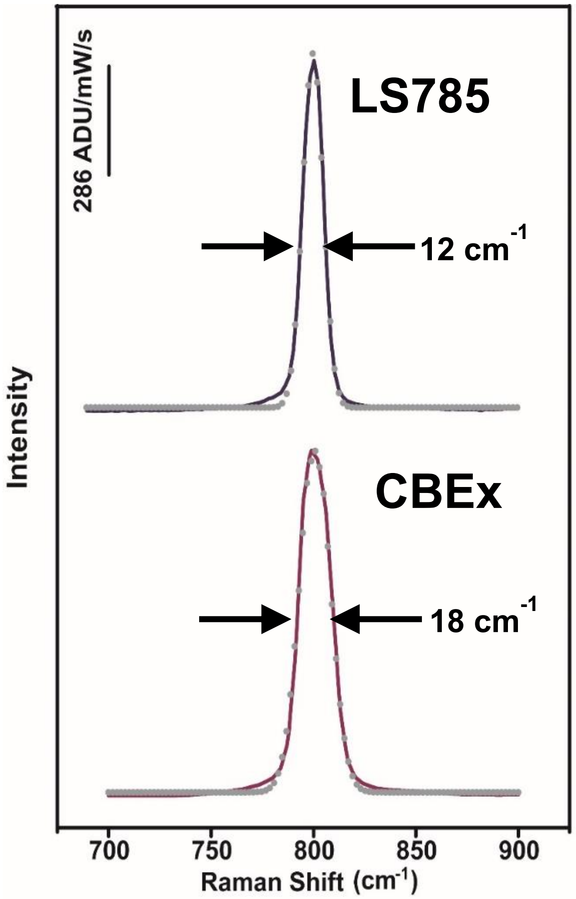

Figure 4.3 Comparison of the full-width half-maximum (FWHM) of the 801.3 cm^{-1} mode of cyclohexane on a standard macro Raman instrument (LS785) and the CBEx™ handheld Raman spectrometer.

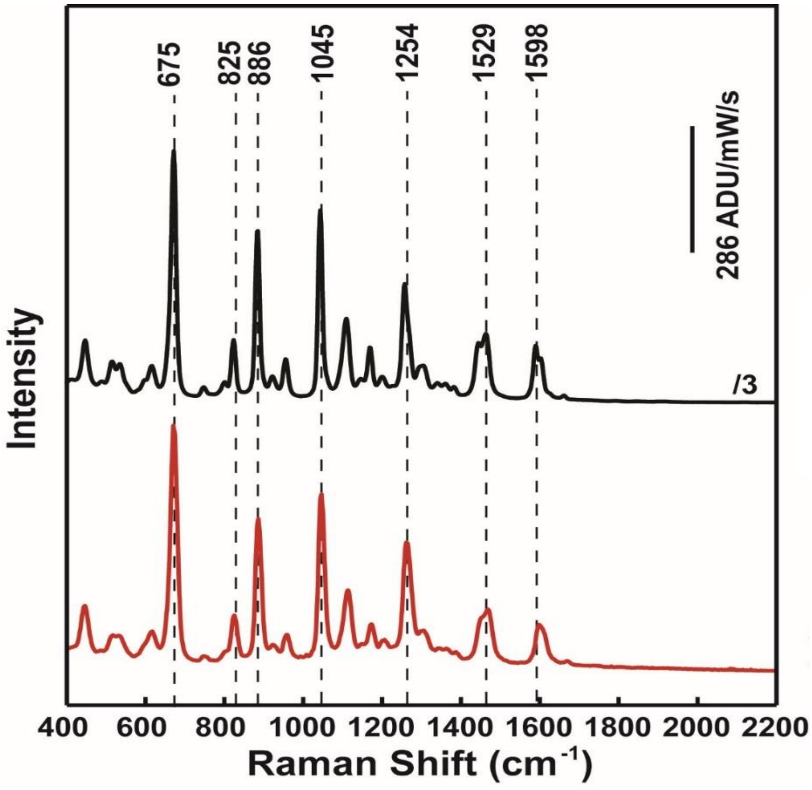

Figure 4.4 NRS of neat propofol. Spectra were acquired with the macro Raman instrument (black trace) and the CBEx™ handheld Raman spectrometer (red trace).

instrumental setup used. First, we acquired an NRS spectrum of cyclohexane, a Raman calibration standard, and compared the peak width of the 801.3 cm^{-1} mode. The macro Raman setup had a peak full-width half maximum (FWHM) of 12 cm^{-1} and the CBEx had a peak FWHM of 18 cm^{-1} (Figure 4.3). Despite the 6 cm^{-1} difference in FWHM, we found that the spectral quality of NRS spectra acquired using the CBEx is comparable to that of a standard macro Raman instrument, as displayed with the NRS spectra of the drug propofol in Figure 4.4.

The mean integrated peak intensities of the 980 and 790 cm^{-1} modes versus concentration of gentamicin show an excellent linear relationship with R^2 values of 0.997 and 0.994 for the standard Raman instrument and 0.999 and 0.999 for the CBEx handheld Raman spectrometer, respectively (Figure 4.5). We found that the integrated peak area of each mode shows a similar

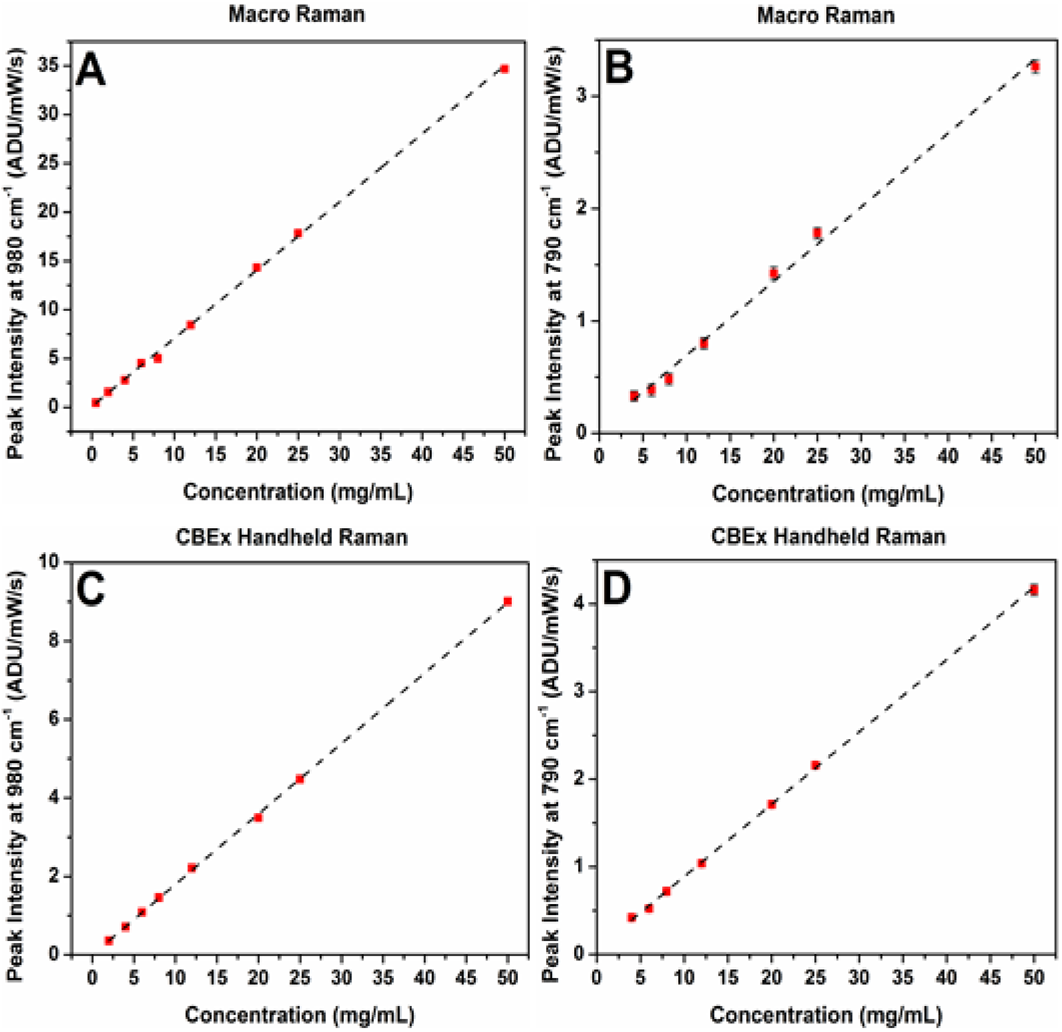

Figure 4.5 Linear NRS calibration curves for gentamicin using integrated peak intensity. Integrated peak intensities at 980 cm^{-1} (A and C) and 790 cm^{-1} (B and D) of gentamicin acquired on the macro Raman instrument (A and B) or the portable CBEx™ Raman spectrometer (C and D). Each data point is the mean of 5 spectra. Acquisition parameters for all spectra: λ_{ex} = 785 nm, P_{ex} = 50 mW, t_{acq} = 5 s.

linear dependence as a function of concentration with $R^2 = 0.996$ and $R^2 = 0.986$ for the standard macro Raman instrument and $R^2 = 0.999$ and $R^2 = 0.992$ for the CBEx handheld spectrometer, respectively (Figure 4.6). This strong linear trend with both the macro Raman setup and the CBEx handheld Raman spectrometer demonstrates the ability of NRS to sensitively and rapidly quantify antibiotic concentrations, and the utility of handheld Raman spectrometers for accurate quantitative Raman measurements.

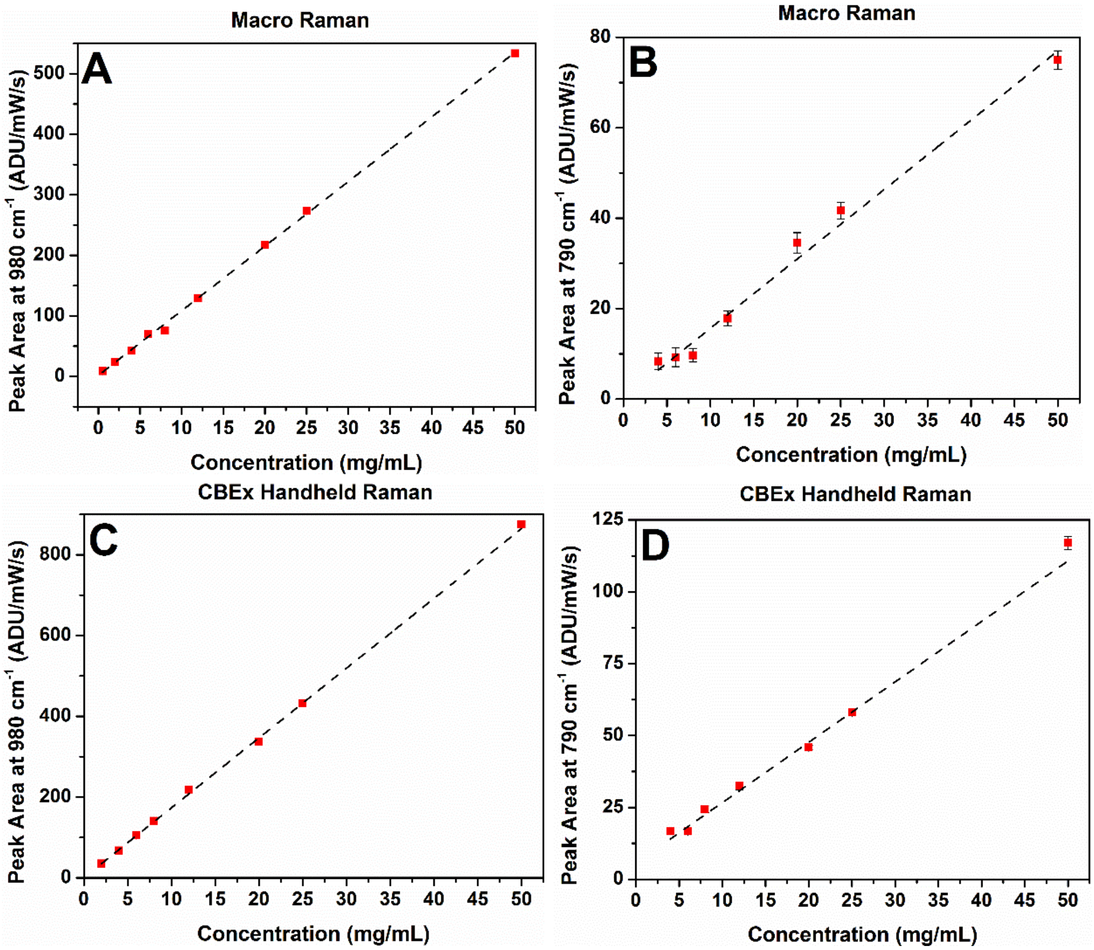

Figure 4.6 Linear NRS calibration curves for gentamicin using integrated peak area. Integrated peak areas at 980 cm^{-1} (A and C) and 790 cm^{-1} (B and D) of gentamicin acquired on the macro Raman instrument (A and B) or the portable CBEx™ Raman spectrometer (C and D). Each data point is the mean of 5 spectra. Acquisition parameters for all spectra: λ_{ex} = 785 nm, P_{ex} = 50 mW, t_{acq} = 5 s.

We then analyzed solutions prepared from a 2 mg/mL commercial gentamicin IV bag solution received from Baxter Healthcare Corporation. This commercial gentamicin solution clearly demonstrated the mode at 980 cm^{-1}. We also observed a clear Raman signal from lower concentrations of gentamicin at the clinically relevant concentration and partial signal below the clinical concentration. The ability to detect NRS of gentamicin in a commercial solution within its clinical range shows promise for the use of handheld Raman to identify antibiotics and other drugs in a clinical setting.

Concentration (mg/mL)	0.5	2	4	6	8	12	20	25	50
Concentration (mM)	1.05	4.20	8.40	12.6	16.8	25.1	41.9	52.4	105
Average integrated peak intensity (ADU/mW/s)	0.477	1.55	2.79	4.51	5.01	8.44	14.3	17.8	34.7
Standard deviation	0.0544	0.0617	0.0728	0.0688	0.0985	0.103	0.139	0.167	0.298
95 % confidence lower limit (ADU/mW/s)	0.456	1.52	2.76	4.48	4.97	8.40	14.3	17.8	34.6
95 % confidence upper limit (ADU/mW/s)	0.499	1.57	2.81	4.54	5.05	8.48	14.4	17.9	34.8

Table 4.1 Calculated mean peak intensities, standard deviation and 95% confidence intervals for the 980 cm^{-1} mode of gentamicin as measured with the macro Raman instrument.

The linear dependence of Raman signal intensity acquired on a standard macro Raman setup versus gentamicin concentration exhibits an interval within 95% confidence of no greater than 0.131 ADU/mW/s aside from 0.234 ADU/mW/s at 50 mg/mL (Table 4.1). The clinically relevant concentrations tested on the macro Raman setup, 2 and 4 mg/mL, showed relatively small confidence intervals of 0.048 and 0.057 ADU/mW/s, respectively (Table 4.1). The correlating experiment performed on the handheld Raman CBEx device showed considerably increased precision. The linear dependence of Raman signal intensity acquired on the CBEx handheld Raman device versus gentamicin concentration exhibits an interval within 95% confidence of no greater than 0.014 ADU/mW/s at any tested concentration aside from 50 mg/mL, which showed a relatively small confidence interval of 0.026 ADU/mW/s (Table 4.2). The concentrations tested within the clinically relevant regime, 2 and 4 mg/mL, showed particularly small confidence intervals of 0.009 and 0.010 ADU/mW/s, respectively (Table 4.2). We also note that each Raman measurement has an acquisition time of 5 seconds per 5 acquisitions, further demonstrating the rapid quantitative nature of handheld NRS experiments. This precise and well-defined relationship demonstrates the strength of this antibiotic's Raman spectrum as an accurate method to quantify drug concentrations both within and out of a clinically relevant concentration range using both a tabletop Raman setup and a handheld Raman spectrometer.

Concentration (mg/mL)	2	4	6	8	12	20	25	50
Concentration (mM)	4.20	8.40	12.6	16.8	25.1	41.9	52.4	105
Average integrated peak intensity (ADU/mW/s)	0.358	0.715	1.10	1.46	2.22	3.49	4.48	9.01
Standard deviation	0.009	0.008	0.009	0.01	0.02	0.01	0.02	0.03
95 % confidence lower limit (ADU/mW/s)	0.354	0.710	1.10	1.46	2.21	3.49	4.48	9.00
95 % confidence upper limit (ADU/mW/s)	0.362	0.721	1.11	1.47	2.22	3.50	4.49	9.02

Table 4.2 Calculated mean peak intensities, standard deviation and 95% confidence intervals for the 980 cm^{-1} mode of gentamicin as measured with the CBEx™ handheld Raman spectrometer.

In addition to quantification of gentamicin concentration with NRS, we examined the effect of pH on the Raman spectrum of gentamicin due to the possible variability of pH in the commercial IV bag solution. The commercial solution of 2 mg/mL gentamicin taken directly from the IV bag was pH = 4.73. Solutions were prepared at ten pH levels ranging from 2 – 11 and after adjusting the peak intensity at 980 cm^{-1} for the added volume of NaOH or HCl, we found the range of Raman signal intensity as a function of pH did not vary significantly. The minimal change in pH shows that gentamicin solutions can be quantified across a wide range of pH values. Overall, using a handheld Raman instrument is an ideal means of rapidly quantifying drug concentrations in a clinical setting or for drug compounding.

4.3.2. Electrochemical SERS of Dobutamine

In the case that the Raman signal is not detectable at clinically relevant concentrations, one can implement SERS to sufficiently amplify the Raman signal. The target analyte in this study was dobutamine, a drug used for improving blood flow and relieving symptoms of heart failure.[122] It is most commonly administered intravenously in concentrations ranging from 0.5 – 4 mg/mL (1.5 - 12 mM) at pH 3.5-3.7. The most common commercial IV bag concentrations are 1, 2, and 4 mg/mL (3, 6 and 12 mM). Additional components of the commercial IV bag solution are 5 % dextrose, edetate disodium dihydrate and 1 % sodium bisulfite. We were not able to detect dobutamine within the clinical range using NRS. We also found that dobutamine was not detectable in its clinically relevant pH range with SERS using a bare, unfunctionalized AuFON due to weak binding of dobutamine to the AuFON surface.

In order to reliably detect dobutamine with SERS, we chose to implement EC-SERS. Previous work has successfully demonstrated SERS of various catecholamines at neutral pH using

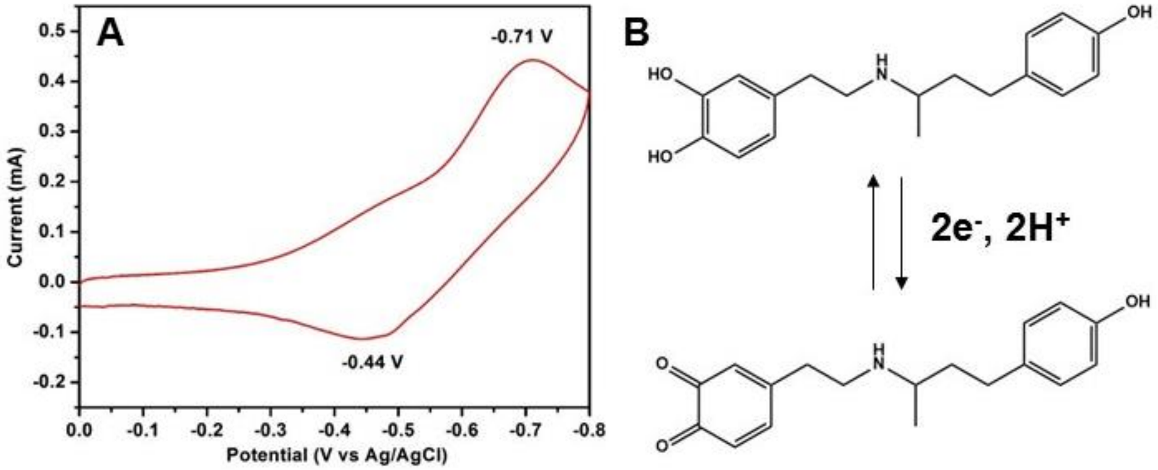

Figure 4.7 Electrochemical behavior of dobutamine. A) CV of 12 mM (4 mg/mL) commercial dobutamine solution at pH = 3.5. Au disc working electrode, Pt wire counter electrode and Ag/AgCl reference electrode. Scan rate = 100 mV/s. B) Schematic of 2-electron, 2-proton transfer of dobutamine from its catechol to quinone species.

an electrochemically roughened Ag working electrode.[153] First, we characterized the solution-phase electrochemistry of the dobutamine IV bag solution with an Au working electrode. The solution phase cyclic voltammogram (CV) using a polished Au disc working electrode is displayed in Figure 4.7A. Dobutamine is a catecholamine and undergoes a reversible 2-electron, 2-proton transfer to form its quinone species (**Figure 4.7**B).[157,158]

EC-SERS measurements were performed using an AuFON working electrode which is a low-cost, highly enhancing SERS-active surface and making electrical contact with the AuFON surface is trivial.[9,12] The FON electrode was fabricated by drop casting 540 nm diameter SiO2 microspheres on a cleaned 25 mm diameter Si wafer. After the spheres dried in a hexagonal close packed array on the surface, 150 nm Au was thermally deposited on the surface. (Figure 4.8A) The LSPR was measured in air and in the dobutamine solution, as the LSPR between a FON in air and in dobutamine solution changes due to the change in local refractive index at the SERS-active surface (Figure 4.8B).[159] The LSPR of the AuFON working electrode in dobutamine overlaps well

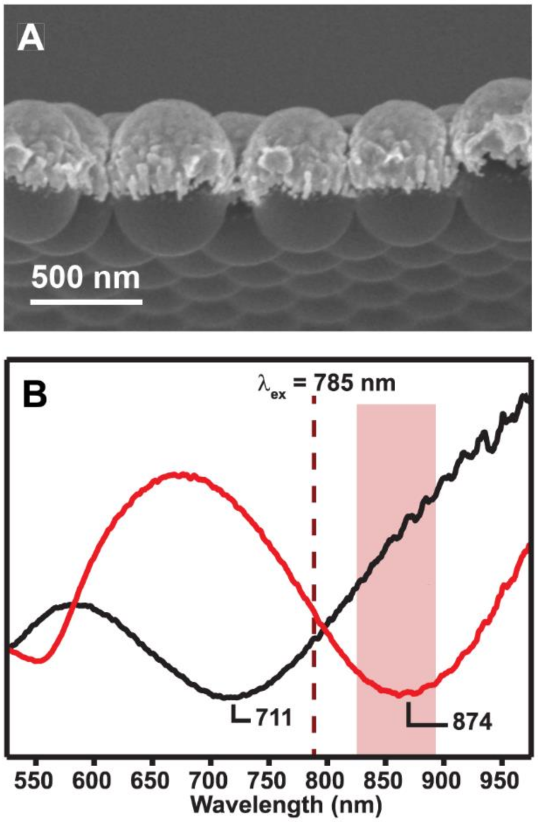

Figure 4.8 AuFON substrates used for EC-SERS. A) Representative SEM image of 540 nm SiO_2 spheres with 150 nm Au deposited. B) LSPR of FON in air (black trace) and in dobutamine solution (red trace).

with the 785 nm excitation wavelength and the wavelength region of the Raman scattered light, ensuring optimal SERS enhancement.[160,161]

We first characterized the EC-SERS response of dobutamine, as shown in Figure 4.9: peaks at 596, 640, 792, 823, 1203, and 1605 cm^{-1} are in excellent agreement with the dobutamine NRS spectrum. In particular, the peak at 1605 cm^{-1} is assigned to the N-H vibration of the secondary amine. Additionally, there are peaks between 1100 and 1500 cm^{-1} in Figure 4.9 that do not appear in the solution phase dobutamine NRS spectrum; these modes are characteristic of a catechol moiety bound to Au.[153,162,163] We then determined the optimal potential to apply to the AuFON working electrode to yield the strongest EC-SERS signal by applying potential stepwise from -0.1 to -0.9 V vs Ag/AgCl in 0.1 V intervals. As shown in Figure 4.10, there is SERS signal at -0.1 V that increased to a maximum at -0.4 V. As the applied potential is swept to more negative values, there is a signal intensity decrease beginning at -0.5 V and the SERS signal then increases in intensity at more negative potentials but does not surpass the intensity at -0.4 V. The decrease in signal between -0.5 and -0.8 V may be due to the oxidation of dobutamine to its quinone form and its relatively weak binding affinity for the AuFON working electrode surface.[164] Based on these results, we chose to apply a constant potential of -0.4 V for detection of dobutamine for all of the following measurements in the study, unless otherwise noted. We also note that this is the first study to demonstrate EC-SERS of secondary catecholamines at acidic pH.

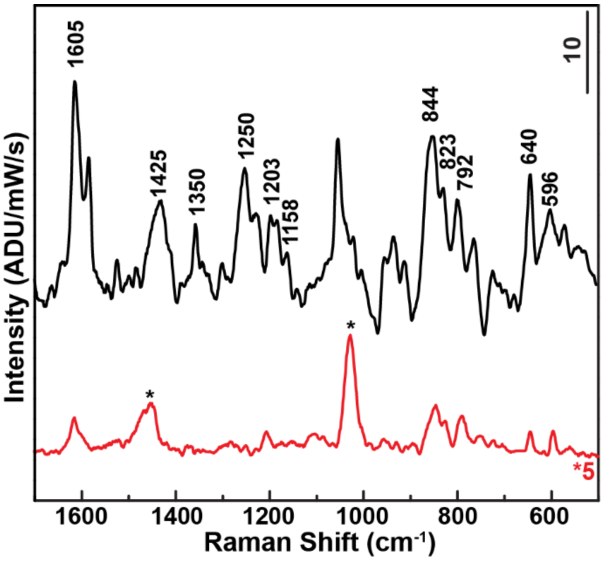

Figure 4.9 EC-SERS of dobutamine. Representative dobutamine EC-SERS spectrum (black trace) compared to NRS of 0.1 M dobutamine in methanol (red trace). Methanol Raman peaks are starred. SERS data: λ_{ex} = 785 nm, P_{ex} = 980 µW, t_{acq} = 30 s. NRS data: λ_{ex} = 785 nm, P_{ex} = 3.4 mW, t_{acq} = 120 s.

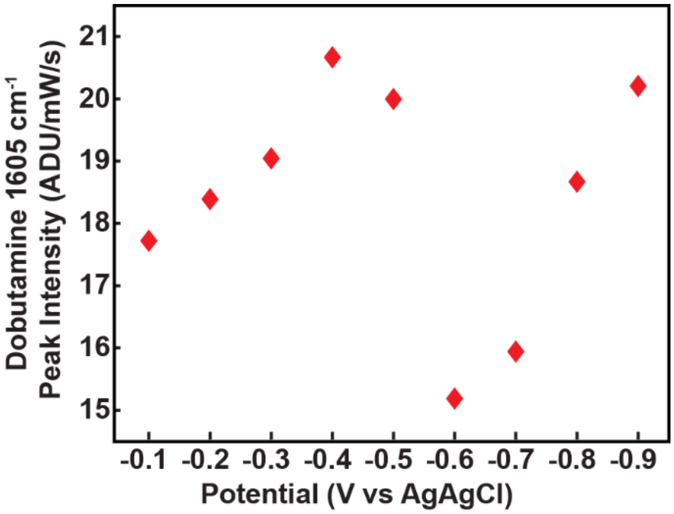

Figure 4.10 Dobutamine EC-SERS 1605 cm^{-1} mode integrated peak intensity as a function of applied potential. Each data point is an average of 3-5 acquired spectra. Acquisition parameters: λ_{ex} = 785 nm, P_{ex} = 980 µW, t_{acq} = 30 s.

Precision and accuracy experiments were then performed to demonstrate the viability of using an AuFON working electrode as a sensing platform. Three individual aliquots of a 2 mg/mL commercial dobutamine IV bag solution were analyzed using the same AuFON working electrode; EC-SERS spectra were acquired from 5 random spots on the AuFON surface. Washing steps with MQ water were performed in between each aliquot measurement. The average peak intensities of the 1605 cm^{-1} mode for each aliquot step are displayed in Figure 4.11. The average peak intensity across the three washing steps does not decrease significantly, which demonstrates the stability and reusability of the AuFON working electrode for multiple EC-SERS measurements. However, the background signal after washing increased after the second wash step, indicating that some dobutamine may still be bound to the AuFON surface.

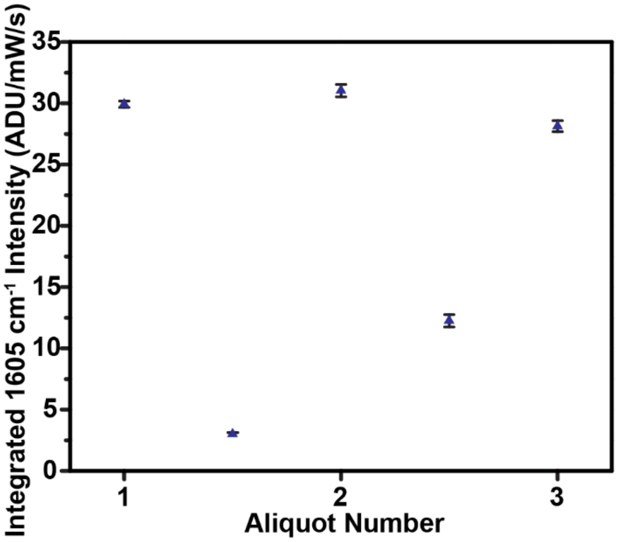

Figure 4.11 Accuracy determination of EC-SERS of dobutamine. Spectra acquired in a solution of 2 mg/mL dobutamine solution with water washing steps in between each aliquot (blue diamonds). Each aliquot was measured on the same AuFON substrate. λ_{ex} = 785 nm, P_{ex} = 980 uW, t_{acq} = 30 s.

Lastly, we performed a limit of detection (LOD) study to determine the sensitivity of the EC-SERS technique. We prepared serial dilutions of the commercial dobutamine IV bag solution ranging from 100 ng/mL – 1 mg/mL (300 nM - 3 mM) and took SERS spectra with the potential held constant at -0.4 V (vs Ag/AgCl). Each data point in Figure 4.12 is an average of 3-5 SERS spectra, where each spectrum is a different spot on the AuFON working electrode surface. We then used the integrated peak intensity of the 1605 cm^{-1} peak to fit the EC-SERS data to a Langmuir adsorption isotherm, as dictated by Equations 4.1 and 4.2[16,17]:

$$\theta = \frac{I_{1605}}{I_{1605,\ max}} = \frac{K_{dobut}\,[D]}{1 + K_{dobut}\,[D]} \qquad \text{(Equation 4.1)}$$

$$\frac{1}{I_{1605}} = \frac{1}{K_{dobut} I_{1605}}\frac{1}{[D]} + \frac{1}{I_{1605,max}} \qquad \text{(Equation 4.2)}$$

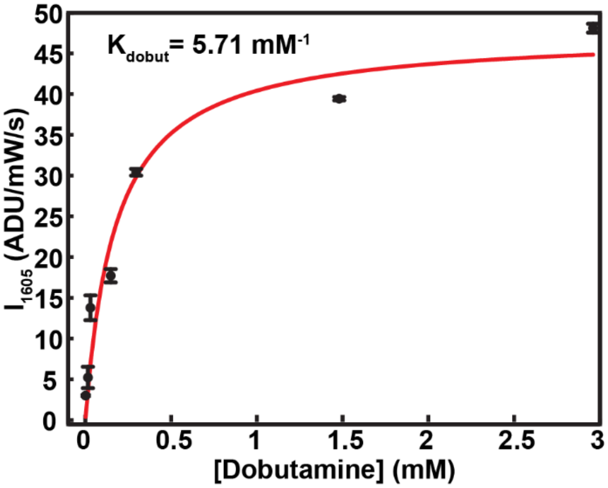

Figure 4.12 Limit of Detection determination for dobutamine. Each data point is an average of 5 spectra on different spots on the AuFON surface (black circles) and fit to a Langmuir isotherm (red trace). Acquisition parameters: λ_{ex} = 785 nm, P_{ex} = 980 µW, t_{acq} = 60 s.

Where θ is the fractional surface coverage, I_{1605} is the normalized peak intensity at 1605 cm^{-1}, [D] is the dobutamine concentration in mM and K_{dobut} is the binding constant. We determined the K_{dobut} from the Langmuir isotherm fitted data to be 5.7 mM^{-1}. (Figure 4.12) We then determined the limit of detection for dobutamine, which is defined as the peak intensity being 3 times greater than the noise level; the LOD of dobutamine was found to be 3 x 10^{-7} M, which is 4 orders of magnitude below the clinical concentration range and agrees well with previous LOD studies of catecholamines with EC-SERS.[153] This data demonstrates that EC-SERS is an extremely sensitive technique for the label-free detection of clinically relevant drugs that cannot be detected using NRS or that bind weakly to SERS substrates.

Lastly, we have demonstrated the feasibility of EC-SERS detection of dobutamine in clinical setting by designing a low-cost, disposable EC-SERS device that can be used for either in-line or off-line testing. A photograph of the bare chip and the assembled EC-SERS device is shown in Figure 4.13. Each disposable EC-SERS device is anticipated to cost approximately $3 and can be fabricated to be less than ~1 in^2 using standard printed circuit board. We used the EC-SERS chip to successfully detect dobutamine taken from a commercial 4 mg/mL IV solution, using the CBEx™ handheld Raman spectrometer. (Figure 4.14) The successful detection of dobutamine with

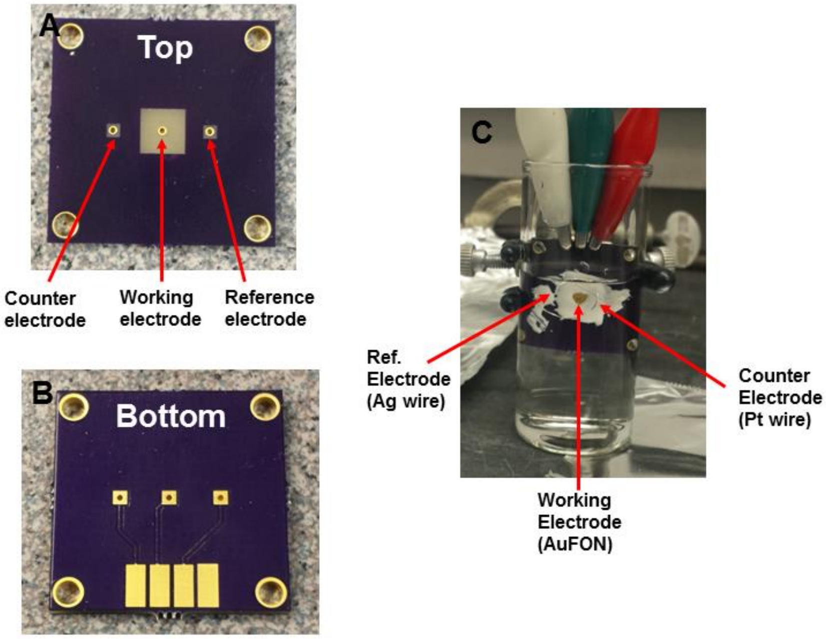

Figure 4.13 Photographs of the commercializable EC-SERS chip. View from the A) top and B) bottom sides. C) EC-SERS chip with epoxied electrodes attached and immersed in a 4 mg/mL dobutamine solution.

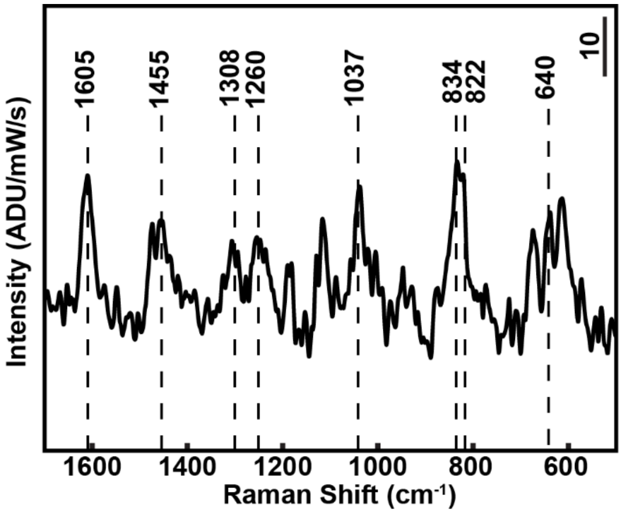

Figure 4.14 EC-SERS of 4 mg/mL dobutamine on AuFON chip device taken with CBex™ spectrometer. Acquisition parameters: λ_{ex} = 785 nm, P_{ex} = 50 mW, t_{acq} = 1 s.

a portable chip and handheld Raman spectrometer proves that EC-SERS has the potential to be a low-cost, sensitive sensing technique for detection of clinically relevant analytes.

4.4. Conclusions and Future Work

Either NRS or EC-SERS can be used as a rapid and sensitive tool to monitor drug concentrations in a clinical setting or for drug compounding. First, we demonstrate the successful detection and precise quantification of gentamicin within its clinically relevant range using both a standard macro and handheld Raman instrument. In the case that the analyte cannot be detected within its clinically relevant range with NRS, like in the case of dobutamine, we can implement SERS. In particular, we implement a label-free EC-SERS detection approach due to the otherwise weak binding of dobutamine on an AuFON SERS substrate. We demonstrate that EC-SERS can detect dobutamine at clinically relevant concentrations and pH range with an LOD of 100 ng/mL (300 nM) and with good accuracy and precision. Additionally, this is the first study to demonstrate EC-SERS of secondary amines at acidic pH. We also demonstrate the potential for a low-cost, commercially viable SERS-active chip for performing EC-SERS experiments in a clinical setting. Overall, this work demonstrates that Raman-based methodologies are a powerful means of facile, rapid monitoring of drug concentrations in a clinical setting or for drug compounding applications.

Chapter 5. Noninvasive Identification of Atherosclerotic Plaques with Spatially Offset Raman Spectroscopy

5.1. Introduction

Together with its complications, atherosclerosis, the buildup of plaques within arteries, is the leading cause of mortality and morbidity in the United States and in most developed countries as of 2012.[165] This systemic process affects multiple arterial beds in the body including the coronary circulation, cerebrovascular circulation, and the peripheral circulation. Respectively, atherosclerosis in these beds leads to heart attack, stroke, and major limb loss through peripheral arterial disease (PAD). The rupture of atherosclerotic plaques increases risk of each of these chronic diseases and accounts for most acute cardiovascular events. The cause of rupture vulnerability in plaques is not well understood, although it is known that plaques' chemical composition and actual size and morphology are directly related to lethality.

Our transcutaneous technique presented in this paper is particularly well suited for detection and characterization of PAD due to the proximity of peripheral arterial beds to the skin surface as well as the relatively low research attention in this area. 8.5 million Americans suffer from PAD alone, and 1.6 million have lost a limb, a significant impairment on their quality of life, as a result. To improve limb salvage it is imperative to improve efforts at early detection and management of peripheral arterial disease (PAD). Like general atherosclerosis, current diagnostic studies for PAD provide little biologic information about the severity of disease. Non-invasive studies such as ankle-brachial indices correlate to gross severity of disease but are falsely elevated in patients with calcified vessels; which is common in patients with diabetes mellitus and end-stage-renal disease. Current diagnostic methods for atherosclerosis and its related diseases are typically costly procedures like MRI scans that often include risk factors by introducing nanoparticles or dyes into patients.[166] Furthermore, imaging studies such as MRI cannot visualize calcium and CT angiography can visualize calcium only as an obscuring factor for luminal flow. Currently, the only method to characterize an atherosclerotic plaque in the peripheral circulation is following open surgical endarterectomy. Other methods of atherosclerosis detection in patients, like listening to blood flow or observing symptoms during stress and exercise, lack the accuracy afforded by the visualization of a plaque. Altogether, these diagnoses are unable to noninvasively characterize a plaque's chemical composition and morphology, which either reduces opportunity for early detection of vulnerable plaques or leads to unnecessary, expensive, and risky surgeries to remove plaques that are not vulnerable. Spatially offset Raman spectroscopy (SORS) provides a transcutaneous method to characterize the calcium profile of patients with PAD and other atherosclerotic diseases and may provide a safe, non-invasive and cost-effective method for early detection and may provide more biologic, severity-specific information.

The nondestructive and noninvasive nature of normal Raman spectroscopy (NRS), along with the low Raman water profile and unique Raman "fingerprints" of many biologically relevant molecules, makes it a strong candidate for biomedical detection and diagnosis. Moreover, it is possible to use NRS for quantification of various chemical components in a substrate. Previous work has demonstrated the potential for using NRS to detect and quantify the components of atherosclerotic plaques, which often contain varying amounts of calcium hydroxyapatite, lipids and triglycerides, and beta-carotene.[167-172] However, all of the arterial plaques that have been tested in previous work were extensively treated and cleaned prior to analysis; blood was removed from the plaque and the spectra were not obtained through peripheral tissues like the arterial wall, fatty tissue, and skin. To date, noninvasive Raman spectroscopy of atherosclerotic plaques embedded within a patient's body has not been modeled or tested.

Raman spectroscopy can be performed noninvasively on tissues inside of the body through the use of spatially offset Raman spectroscopy (SORS). Subsurface Raman scattered photons are more diffusely scattered than surface scattering, which tends to occur within the excitation volume of the laser. In order to collect more diffusely scattered photons, a SORS setup requires only optical fibers arranged in a small ring along with a typical Raman setup, which can be portable.[173] The ring-shaped arrangement of the fibers moves the collection of Raman scattered photons a fixed distance away from the laser excitation point and therefore enables collection of the more diffuse subsurface Raman signals. This ultimately enables the completely noninvasive detection of materials inside the body.[174] SORS has been previously explored for non-invasive detection of cancerous breast tissue[175] and bone deformities[176] with promising results.

In this work, we utilize SORS to demonstrate noninvasive Raman analysis of atherosclerotic arteries. Specifically, we consistently detect calcium hydroxyapatite (HA) within calcified arterial plaque samples. We also analyze the change in HA SORS signal as a function of focal depth within the calcified tissue, showing that the change in signal intensity is correlated to the degree of calcification throughout the plaque sample. We can therefore expect to visualize the sensitivity of SORS to detectable components and to demonstrate their relative prevalence in layers of the calcification. After understanding SORS signal within the arterial plaque alone, we then successfully demonstrate the first SORS spectra of calcified atherosclerotic plaque embedded within femoral arterial tissue. These results verify the ability of SORS to noninvasively identify and characterize atherosclerotic plaques in a clinical setting without the need to perform surgery.

5.2. Experimental Details

All human artery and arterial plaque samples used were received from an institutional review board-approved tissue banking protocol (Biobank) at Washington University, St. Louis. The samples were analyzed as received; no washing treatment was performed to remove excess blood or unwanted tissue. Samples were pinned to a padded board for SORS analysis. 785 nm laser excitation was focused onto the sample with a custom optical setup, as shown in the schematic in Figure 5.1.[177] The excitation power at the sample for all experiments in this work was set to either 4 or 10 mW. We note that previous studies of normal Raman spectroscopy of plaques utilize at least 100 mW NIR laser excitation power.[169] The SORS scattering was collected using a custom-made 26 fiber bundle (C-Technologies), where the fibers arranged in a 6 mm diameter circle on

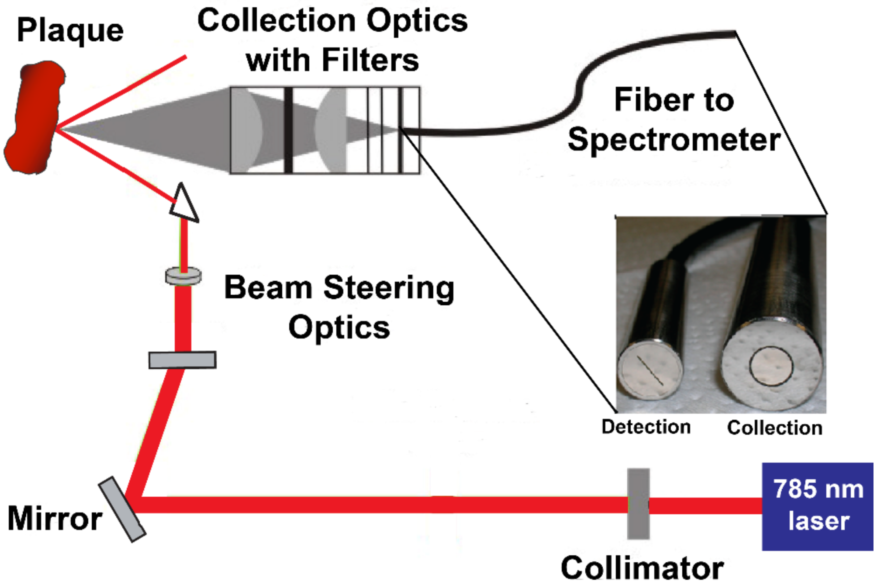

Figure 5.1 SORS Instrumental Setup. Schematic of SORS instrumental setup and photograph of the detection and collection ends of the custom SORS fiber. Adapted with permission from Ref. 176. Copyright 2013 American Chemical Society.

the collection end, and vertically aligned at the detection end (Figure 5.1, inset). Spectra were then baseline corrected using a polynomial fitting routine in MATLAB.

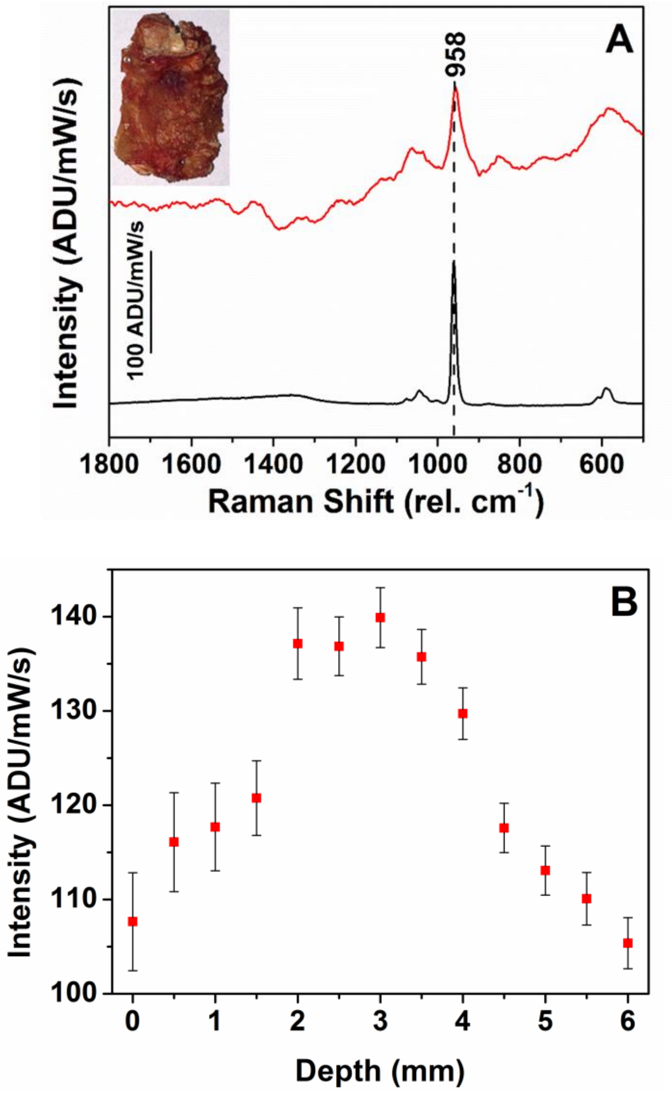

Figure 5.3 SORS of atherosclerotic plaques. A) SORS spectra of atherosclerotic plaque 1 after polynomial baseline fitting and subtraction (red trace) compared to solid HA (black trace). Inset: photograph of plaque sample 1. SORS signal was obtained at 785 nm and 4 mW with 30 s acquisition time. B) Plot of SORS signal intensity versus laser spot focal depth. Spectra were obtained at 785 nm and 10 mW with 30 s acquisition time. The spike in signal correlates strongly with the thickness of the white calcification within the center of the plaque sample.

5.3. Results and Discussion

We first obtained SORS spectra from atherosclerotic plaques without surrounding artery or tissue. The first plaque sample was taken from a diabetic 85 year-old male patient's femoral artery and ranged from 2 to 5 mm in thickness with a distinctive, white, 4 mm thick calcification in the thickest region of the plaque (Figure 5.3, inset). The second and third arterial plaque samples were also collected the femoral artery of the same patient as the first plaque and did not exhibit large calcified regions like the first plaque. We were unable to acquire Raman signal from the plaque samples using a normal Raman spectroscopy setup (not shown). We collected SORS spectra from the atherosclerotic tissue of sample 1, as shown in Figure 5.3A. The primary spectral feature is the peak at 958 cm^{-1}, corresponding to a ν_4 phosphate vibration of calcium hydroxyapatite (HA), one of the major components of atherosclerotic plaques; this matches well to a solid reference spectrum of HA (Figure 5.3) and previously reported spectra.[171]

We then monitored the intensity of the 958 cm^{-1} peak as a function of probe depth in the first plaque tested (Figure 5.3B). The signal intensity reaches a maximum at a depth of 3 mm, which overlaps with the center distance of the large calcified region within the plaque sample. SORS spectra acquired from the latter two arterial plaques also had strong peaks at 958 cm-1, indicative of HA (Figure 5.4).These results demonstrate that SORS can be used to successfully characterize atherosclerotic plaques and monitor the relative degree of calcification within a single arterial plaque sample.

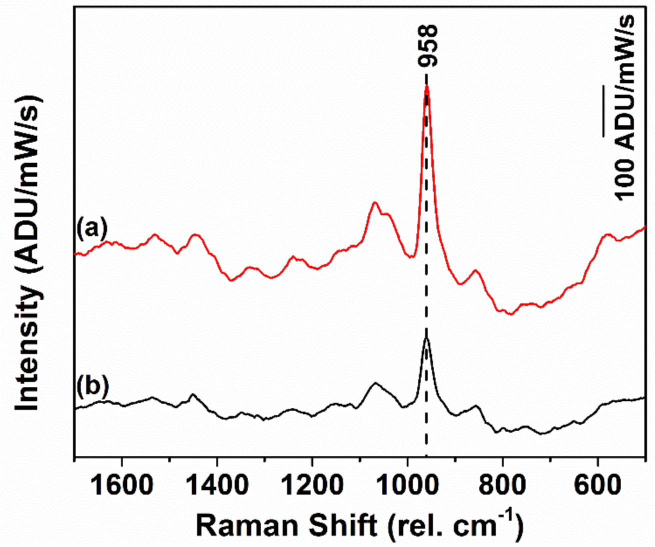

Figure 5.4 SORS of additional atherosclerotic plaques. Baseline-fitted and subtracted SORS spectra of atherosclerotic plaque (a) sample 2 and (b) sample 3. SORS spectra were acquired at 785 nm and 4 mW with 30 s acquisitions. Plaque sample 3 was taken from the same patient as plaque 1.

After successfully demonstrating the detection of artery plaques with SORS, we then analyzed a human femoral atherosclerotic occlusion sample embedded within its original arterial tissue, with some peripheral adipose tissue. The plaque was 5 mm thick, the surrounding arterial wall was 1-2 mm thick and the surrounding adipose tissue islands were 2 mm thick. We first acquired SORS spectra of the plaque sample with whitish plaque feature facing the laser excitation; the presence of the 958 cm^{-1} peak confirmed the plaque was composed of HA. We then focused on the outer artery wall into the artery sample. The SORS spectra obtained from this area had two distinct peaks at 958 and 1442 cm^{-1} (Figure 5.5). The peak at 1442 cm^{-1} can be assigned to a CH_2 scissoring vibration. It is possible that this indicates lipid pools about the calcification.[168] Additionally, if we measure SORS spectra from a different region of the plaque, the 1442 cm^{-1} peak is no longer present. Our results demonstrate multiple components of the arterial plaque can be simultaneously detected with SORS.

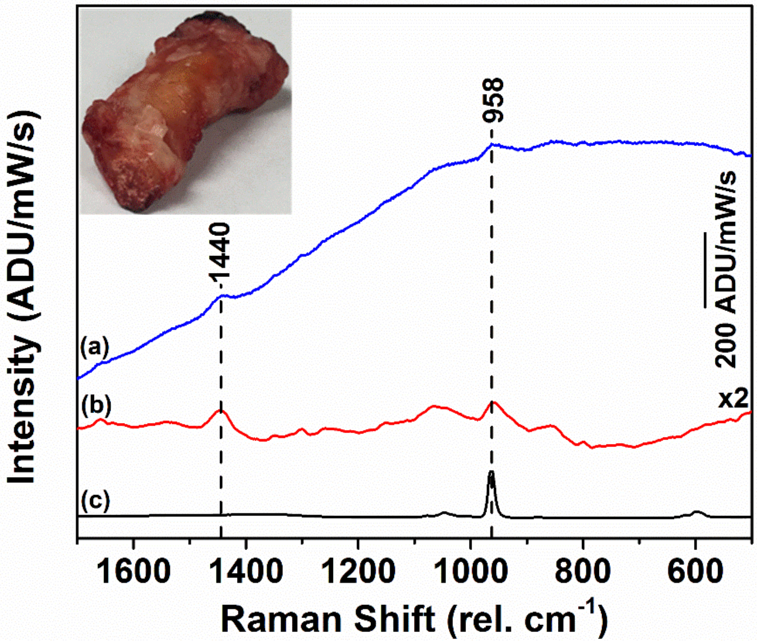

Figure 5.5 SORS of atherosclerotic plaque with surrounding fatty tissue. (a) SORS of atherosclerotic plaque through arterial wall and adipose tissue taken at 785 nm and 4 mW with 60 s acquisitions. (b) polynomial baseline fitted and subtracted spectrum of spectrum (a). (c) normal Raman spectrum of solid HA. Inset: Photograph of the artery sample with the atherosclerotic plaque.

5.4. Conclusions and Future Directions

In this work, we have demonstrated the ability to detect atherosclerotic plaques non-invasively using SORS. We demonstrate the first Raman spectra of plaques at relatively low laser excitation powers and without sample cleaning or pretreatment. The most dominant spectral feature in the SORS spectra of the plaque samples is assigned to calcium hydroxyapatite, the primary component of atherosclerotic plaques. We were also able successful in detecting lipids, which can originate from the plaque itself or the surrounding adipose tissue. Future work towards the viability of SORS as a diagnostic technique for plaque formation and detection includes: 1) determining a threshold limit for plaque detection and 2) assessing the ability to define a relative plaque “lethality” with SORS. In order to achieve these goals, we will first controllably grow calcium hydroxyapatite crystals and structurally characterize the crystals using techniques such as SEM-EDX. Next, we will then assess the limits of detection by placing the HA crystals in a subcutaneous layer and acquire SORS spectra. Finally, we will create a SORS calibration curve, taking into account both plaque size and relative depth underneath an opaque layer (e.g. skin, adipose tissue). Overall, the use of SORS to detect atherosclerotic plaques is an extremely promising non-invasive technique that can readily be applied in a clinical setting.

References

(1) Fleischmann, M.; Hendra, P. J.; McQuillan, A. J. *Chemical Physics Letters* **1974**, *26*, 163.

(2) Jeanmaire, D. L.; Van Duyne, R. P. *Journal of Electroanalytical Chemistry* **1977**, *84*, 1.

(3) Morton, S. M.; Jensen, L. *Journal of the American Chemical Society* **2009**, *131*, 4090.

(4) McMahon, J. M.; Li, S.; Ausman, L. K.; Schatz, G. C. *The Journal of Physical Chemistry C* **2012**, *116*, 1627.

(5) Willets, K. A.; Van Duyne, R. P. *Annual Review of Physical Chemistry* **2007**, *58*, 267.

(6) Kleinman, S. L.; Frontiera, R. R.; Henry, A.-I.; Dieringer, J. A.; Van Duyne, R. P. *Physical Chemistry Chemical Physics* **2013**, *15*, 21.

(7) Lee, P. C.; Meisel, D. *The Journal of Physical Chemistry* **1982**, *86*, 3391.

(8) Kleinman, S. L.; Ringe, E.; Valley, N.; Wustholz, K. L.; Phillips, E.; Scheidt, K. A.; Schatz, G. C.; Van Duyne, R. P. *Journal of the American Chemical Society* **2011**, *133*, 4115.

(9) Hulteen, J. C.; Van Duyne, R. P. *Journal of Vacuum Science & Technology A* **1995**, *13*, 1553.

(10) Zrimsek, A. B.; Henry, A.-I.; Van Duyne, R. P. *The Journal of Physical Chemistry Letters* **2013**, *4*, 3206.

(11) Greeneltch, N. G.; Blaber, M. G.; Henry, A. I.; Schatz, G. C.; Van Duyne, R. P. *Analytical Chemistry* **2013**, *85*, 2297.

(12) Paxton, W. F.; Kleinman, S. L.; Basuray, A. N.; Stoddart, J. F.; Van Duyne, R. P. *The Journal of Physical Chemistry Letters* **2011**, *2*, 1145.

(13) Greeneltch, N. G.; Davis, A. S.; Valley, N. A.; Casadio, F.; Schatz, G. C.; Van Duyne, R. P.; Shah, N. C. *The Journal of Physical Chemistry A* **2012**, *116*, 11863.

(14) Sonntag, M. D.; Klingsporn, J. M.; Zrimsek, A. B.; Sharma, B.; Ruvuna, L. K.; Van Duyne, R. P. *Chemical Society reviews* **2014**, *43*, 1230.

(15) Pozzi, F.; Zaleski, S.; Casadio, F.; Leona, M.; Lombardi, J. R.; Van Duyne, R. P. In *Nanoscience and Cultural Heritage*; Dillmann, P., Bellot-Gurlet, L., Nenner, I., Eds.; Atlantis Press: Paris, 2016, p 161.

(16) Zhang, X.; Young, M. A.; Lyandres, O.; Van Duyne, R. P. *Journal of the American Chemical Society* **2005**, *127*, 4484.

(17) Zhang, X.; Zhao, J.; Whitney, A. V.; Elam, J. W.; Van Duyne, R. P. *Journal of the American Chemical Society* **2006**, *128*, 10304.

(18) Hartman, T.; Wondergem, C. S.; Kumar, N.; van den Berg, A.; Weckhuysen, B. M. *The Journal of Physical Chemistry Letters* **2016**, *7*, 1570.

(19) Kneipp, K.; Wang, Y.; Kneipp, H.; Perelman, L. T.; Itzkan, I.; Dasari, R. R.; Feld, M. S. *Physical Review Letters* **1997**, *78*, 1667.

(20) Nie, S.; Emory, S. R. *Science* **1997**, *275*, 1102.

(21) Andersen, P. C.; Jacobson, M. L.; Rowlen, K. L. *The Journal of Physical Chemistry B* **2004**, *108*, 2148.

(22) Etchegoin, P. G.; Meyer, M.; Le Ru, E. C. *Physical Chemistry Chemical Physics* **2007**, *9*, 3006.

(23) Le Ru, E. C.; Meyer, M.; Etchegoin, P. G. *The Journal of Physical Chemistry B* **2006**, *110*, 1944.

(24) Zrimsek, A. B.; Wong, N. L.; Van Duyne, R. P. *The Journal of Physical Chemistry C* **2016**, *120*, 5133.

(25) Dieringer, J. A.; Lettan, R. B.; Scheidt, K. A.; Van Duyne, R. P. *Journal of the American Chemical Society* **2007**, *129*, 16249.

(26) Sonntag, M. D.; Klingsporn, J. M.; Garibay, L. K.; Roberts, J. M.; Dieringer, J. A.; Seideman, T.; Scheidt, K. A.; Jensen, L.; Schatz, G. C.; Van Duyne, R. P. *The Journal of Physical Chemistry C* **2012**, *116*, 478.

(27) Zhang, Z.; Deckert-Gaudig, T.; Singh, P.; Deckert, V. *Chemical communications* **2015**, *51*, 3069.

(28) Choi, H. K.; Park, W. H.; Park, C. G.; Shin, H. H.; Lee, K. S.; Kim, Z. H. *Journal of the American Chemical Society* **2016**, *138*, 4673.

(29) Zhang, M.; Zhao, L.-B.; Luo, W.-L.; Pang, R.; Zong, C.; Zhou, J.-Z.; Ren, B.; Tian, Z.-Q.; Wu, D.-Y. *The Journal of Physical Chemistry C* **2016**.

(30) Huang, Y.-F.; Zhu, H.-P.; Liu, G.-K.; Wu, D.-Y.; Ren, B.; Tian, Z.-Q. *Journal of the American Chemical Society* **2010**, *132*, 9244.

(31) Wu, D.-Y.; Zhao, L.-B.; Liu, X.-M.; Huang, R.; Huang, Y.-F.; Ren, B.; Tian, Z.-Q. *Chemical communications* **2011**, *47*, 2520.

(32) Brooks, J. L.; Frontiera, R. R. *The Journal of Physical Chemistry C* **2016**.

(33) Ren, X.; Tan, E.; Lang, X.; You, T.; Jiang, L.; Zhang, H.; Yin, P.; Guo, L. *Physical Chemistry Chemical Physics* **2013**, *15*, 14196.

(34) Xu, J.-F.; Liu, G.-K. *Spectrochimica Acta Part A: Molecular and Biomolecular Spectroscopy* **2015**, *138*, 873.

(35) Dong, B.; Fang, Y.; Chen, X.; Xu, H.; Sun, M. *Langmuir* **2011**, *27*, 10677.

(36) Gawinkowski, S.; Pszona, M.; Gorski, A.; Niedziolka-Jonsson, J.; Kaminska, I.; Nogala, W.; Waluk, J. *Nanoscale* **2016**, *8*, 3337.

(37) Sigle, D. O.; Kasera, S.; Herrmann, L. O.; Palma, A.; de Nijs, B.; Benz, F.; Mahajan, S.; Baumberg, J. J.; Scherman, O. A. *The Journal of Physical Chemistry Letters* **2016**, *7*, 704.

(38) Masson, E.; Ling, X.; Joseph, R.; Kyeremeh-Mensah, L.; Lu, X. *RSC Advances* **2012**, *2*, 1213.

(39) Chen, Y.; Klimczak, A.; Galoppini, E.; Lockard, J. V. *RSC Advances* **2013**, *3*, 1354.

(40) Lussier, F.; Brulé, T.; Vishwakarma, M.; Das, T.; Spatz, J. P.; Masson, J.-F. *Nano letters* **2016**.

(41) Fan, F. R.; Bard, A. J. *Science* **1995**, *267*, 871.

(42) Bard, A. J.; Fan, F.-R. F. *Accounts of Chemical Research* **1996**, *29*, 572.

(43) Fan, F.-R. F.; Kwak, J.; Bard, A. J. *Journal of the American Chemical Society* **1996**, *118*, 9669.

(44) Kang, S.; Nieuwenhuis, A. F.; Mathwig, K.; Mampallil, D.; Lemay, S. G. *ACS Nano* **2013**, *7*, 10931.

(45) Byers, J. C.; Paulose Nadappuram, B.; Perry, D.; McKelvey, K.; Colburn, A. W.; Unwin, P. R. *Analytical Chemistry* **2015**, *87*, 10450.

(46) Lemay, S. G.; Kang, S.; Mathwig, K.; Singh, P. S. *Accounts of Chemical Research* **2012**, *46*, 369.

(47) Mathwig, K.; Aartsma, T. J.; Canters, G. W.; Lemay, S. G. *Annual Reviews of Analytical Chemistry* **2014**, *7*, 383.

(48) Oja, S. M.; Fan, Y.; Armstrong, C. M.; Defnet, P.; Zhang, B. *Analytical Chemistry* **2016**, *88*, 414.

(49) Lei, C.; Hu, D.; Ackerman, E. J. *Chemical communications* **2008**, 5490.

(50) Salverda, J. M.; Patil, A. V.; Mizzon, G.; Kuznetsova, S.; Zauner, G.; Akkilic, N.; Canters, G. W.; Davis, J. J.; Heering, H. A.; Aartsma, T. J. *Angewante Chemie International Edition* **2010**, *49*, 5776.

(51) Shen, H.; Zhou, X.; Zou, N.; Chen, P. *The Journal of Physical Chemistry C* **2014**, *118*, 26902.

(52) Rao, V. G.; Dhital, B.; He, Y.; Lu, H. P. *The Journal of Physical Chemistry C* **2014**, *118*, 20209.

(53) Rao, V. G.; Dhital, B.; Peter Lu, H. *Chemical communications* **2015**, *51*, 16821.

(54) Palacios, R. E.; Fan, F.-R. F.; Bard, A. J.; Barbara, P. F. *Journal of the American Chemical Society* **2006**, *128*, 9028.

(55) Chang, Y.-L.; Palacios, R. E.; Fan, F.-R. F.; Bard, A. J.; Barbara, P. F. *Journal of the American Chemical Society* **2008**, *130*, 8906.

(56) Pan, S.; Liu, J.; Hill, C. M. *The Journal of Physical Chemistry C* **2015**, *119*, 27095.

(57) Wilson, A. J.; Marchuk, K.; Willets, K. A. *Nano letters* **2015**, *15*, 6110.

(58) Cortés, E.; Etchegoin, P. G.; Le Ru, E. C.; Fainstein, A.; Vela, M. E.; Salvarezza, R. C. *Journal of the American Chemical Society* **2010**, *132*, 18034.

(59) Wang, Y.; Sevinc, P. C.; He, Y.; Lu, H. P. *Journal of the American Chemical Society* **2011**, *133*, 6989.

(60) Cortes, E.; Etchegoin, P. G.; Le Ru, E. C.; Fainstein, A.; Vela, M. E.; Salvarezza, R. C. *Journal of the American Chemical Society* **2013**, *135*, 2809.

(61) Wilson, A. J.; Willets, K. A. *Nano letters* **2014**, *14*, 939.

(62) Weber, M. L.; Wilson, A. J.; Willets, K. A. *The Journal of Physical Chemistry C* **2015**, *119*, 18591.

(63) Zaleski, S.; Cardinal, M. F.; Klingsporn, J. M.; Van Duyne, R. P. *The Journal of Physical Chemistry C* **2015**, *119*, 28226.

(64) Thompson, M. A.; Lew, M. D.; Moerner, W. E. *Annual Reviews of Biophysics* **2012**, *41*, 321.

(65) Weber, M. L.; Willets, K. A. *The Journal of Physical Chemistry Letters* **2011**, *2*, 1766.

(66) Willets, K. A. *Chemical Society reviews* **2014**, *43*, 3854.

(67) Stranahan, S. M.; Willets, K. A. *Nano letters* **2010**, *10*, 3777.

(68) Titus, E. J.; Weber, M. L.; Stranahan, S. M.; Willets, K. A. *Nano letters* **2012**, *12*, 5103.

(69) Kurouski, D.; Mattei, M.; Van Duyne, R. P. *Nano letters* **2015**, *15*, 7956.

(70) Zong, C.; Chen, C.-J.; Zhang, M.; Wu, D.-Y.; Ren, B. *Journal of the American Chemical Society* **2015**, *137*, 11768.

(71) Zhang, R.; Zhang, Y.; Dong, Z. C.; Jiang, S.; Zhang, C.; Chen, L. G.; Zhang, L.; Liao, Y.; Aizpurua, J.; Luo, Y.; Yang, J. L.; Hou, J. G. *Nature* **2013**, *498*, 82.

(72) Jiang, S.; Zhang, Y.; Zhang, R.; Hu, C.; Liao, M.; Luo, Y.; Yang, J.; Dong, Z.; Hou, J. G. *Nature nanotechnology* **2015**, *10*, 865.

(73) Bartlett, P. N.; Baumberg, J. J.; Coyle, S.; Abdelsalam, M. E. *Faraday Discussions* **2004**, *125*, 117.

(74) Brolo, A. G.; Arctander, E.; Gordon, R.; Leathem, B.; Kavanagh, K. L. *Nano letters* **2004**, *4*, 2015.

(75) Li, J.-F.; Rudnev, A.; Fu, Y.; Bodappa, N.; Wandlowski, T. *ACS Nano* **2013**, *7*, 8940.

(76) Li, Z.; Han, B.; Meszaros, G.; Pobelov, I.; Wandlowski, T.; Blaszczyk, A.; Mayor, M. *Faraday Discussions* **2006**, *131*, 121.

(77) Liu, B.; Blaszczyk, A.; Mayor, M.; Wandlowski, T. *ACS Nano* **2011**, *5*, 5662.

(78) Chidsey, C. E. D.; Bertozzi, C. R.; Putvinski, T. M.; Mujsce, A. M. *Journal of the American Chemical Society* **1990**, *112*, 4301.

(79) Pheeney, C. G.; Barton, J. K. *Langmuir* **2012**, *28*, 7063.

(80) Wilson, A. J.; Molina, N. Y.; Willets, K. A. *The Journal of Physical Chemistry C* **2016**.

(81) Liu, H.-H.; Lu, J.-L.; Zhang, M.; Pang, D.-W. *Analytical Sciences* **2002**, *18*, 1339.

(82) Venkataraman, L.; Klare, J. E.; Nuckolls, C.; Hybertsen, M. S.; Steigerwald, M. L. *Nature* **2006**, *442*, 904.

(83) Shan, X.; Patel, U.; Wang, S.; Iglesias, R.; Tao, N. *Science* **2010**, *327*, 1363.

(84) Mao, X.; Hatton, T. A. *Industrial & Engineering Chemistry Research* **2015**.

(85) Lipson, A. L.; Puntambekar, K.; Comstock, D. J.; Meng, X.; Geier, M. L.; Elam, J. W.; Hersam, M. C. *Chemistry of Materials* **2014**, *26*, 935.

(86) Lipson, A. L.; Ginder, R. S.; Hersam, M. C. *Advanced Materials* **2011**, *23*, 5613.

(87) Yu; Chang, S.-S.; Lee, C.-L.; Wang, C. R. C. *The Journal of Physical Chemistry B* **1997**, *101*, 6661.

(88) Taberna, P. L.; Mitra, S.; Poizot, P.; Simon, P.; Tarascon, J. M. *Nature materials* **2006**, *5*, 567.

(89) Davis, J. J.; Burgess, H.; Zauner, G.; Kuznetsova, S.; Salverda, J.; Aartsma, T.; Canters, G. W. *The Journal of Physical Chemistry B* **2006**, *110*, 20649.

(90) Goldsmith, R. H.; Tabares, L. C.; Kostrz, D.; Dennison, C.; Aartsma, T. J.; Canters, G. W.; Moerner, W. E. *Procedings of the National Academy of Science* **2011**, *108*, 17269.

(91) Huang, K.-C.; White, R. J. *Journal of the American Chemical Society* **2013**, *135*, 12808.

(92) Zhang, J.; Kuznetsov, A. M.; Medvedev, I. G.; Chi, Q.; Albrecht, T.; Jensen, P. S.; Ulstrup, J. *Chemical reviews* **2008**, *108*, 2737.

(93) Hill, C. M.; Clayton, D. A.; Pan, S. *Physical Chemistry Chemical Physics* **2013**, *15*, 20797.

(94) Tao, N. J. *Physical Review Letters* **1996**, *76*, 4066.

(95) Blackie, E.; Le Ru, E. C.; Meyer, M.; Timmer, M.; Burkett, B.; Northcote, P.; Etchegoin, P. G. *Physical Chemistry Chemical Physics* **2008**, *10*, 4147.

(96) Etchegoin, P. G.; Le Ru, E. C.; Fainstein, A. *Physical Chemistry Chemical Physics* **2011**, *13*, 4500.

(97) Blackie, E. J.; Ru, E. C. L.; Etchegoin, P. G. *Journal of the American Chemical Society* **2009**, *131*, 14466.

(98) Etchegoin, P. G.; Le Ru, E. C.; Meyer, M. *Journal of the American Chemical Society* **2009**, *131*, 2713.

(99) Artur, C.; Le Ru, E. C.; Etchegoin, P. G. *The Journal of Physical Chemistry Letters* **2011**, *2*, 3002.

(100) Le Ru, E. C.; Etchegoin, P. G. *Annual Review of Physical Chemistry* **2012**, *63*, 65.

(101) Patra, P. P.; Chikkaraddy, R.; Tripathi, R. P. N.; Dasgupta, A.; Kumar, G. V. P. *Nat Commun* **2014**, *5*.

(102) Crozier, K. B.; Wenqi, Z.; Dongxing, W.; Shiyun, L.; Best, M. D.; Camden, J. P. *Selected Topics in Quantum Electronics, IEEE Journal of* **2014**, *20*, 152.

(103) Ahmed, A.; Gordon, R. *Nano letters* **2012**, *12*, 2625.

(104) Steidtner, J.; Pettinger, B. *Physical Review Letters* **2008**, *100*, 236101.

(105) Mirsaleh-Kohan, N.; Iberi, V.; Simmons, P. D.; Bigelow, N. W.; Vaschillo, A.; Rowland, M. M.; Best, M. D.; Pennycook, S. J.; Masiello, D. J.; Guiton, B. S.; Camden, J. P. *The Journal of Physical Chemistry Letters* **2012**, *3*, 2303.

(106) Galloway, C. M.; Le Ru, E. C.; Etchegoin, P. G. *Physical Chemistry Chemical Physics* **2009**, *11*, 7372.

(107) Dieringer, J. A.; Wustholz, K. L.; Masiello, D. J.; Camden, J. P.; Kleinman, S. L.; Schatz, G. C.; Van Duyne, R. P. *Journal of the American Chemical Society* **2009**, *131*, 849.

(108) Fu, Y.; Dlott, D. D. *The Journal of Physical Chemistry C* **2015**, *119*, 6373.

(109) Zhang, D.; Xie, Y.; Deb, S. K.; Davison, V. J.; Ben-Amotz, D. *Analytical Chemistry* **2005**, *77*, 3563.

(110) Bard, A. J.; Faulkner, L. R. *Electrochemical Methods: Fundamentals and Applications, 2nd Edition*; Wiley, 2000.

(111) Jäckel, F.; Kinkhabwala, A. A.; Moerner, W. E. *Chemical Physics Letters* **2007**, *446*, 339.

(112) Shegai, T.; Vaskevich, A.; Rubinstein, I.; Haran, G. *Journal of the American Chemical Society* **2009**, *131*, 14390.

(113) Redmond, P. L.; Hallock, A. J.; Brus, L. E. *Nano letters* **2005**, *5*, 131.

(114) Dieringer, J. A.; McFarland, A. D.; Shah, N. C.; Stuart, D. A.; Whitney, A. V.; Yonzon, C. R.; Young, M. A.; Zhang, X.; Van Duyne, R. P. *Faraday Discussions* **2006**, *132*, 9.

(115) Sonntag, M. D.; Chulhai, D.; Seideman, T.; Jensen, L.; Van Duyne, R. P. *Journal of the American Chemical Society* **2013**, *135*, 17187.

(116) Klingsporn, J. M.; Jiang, N.; Pozzi, E. A.; Sonntag, M. D.; Chulhai, D.; Seideman, T.; Jensen, L.; Hersam, M. C.; Van Duyne, R. P. *Journal of the American Chemical Society* **2014**, *136*, 3881.

(117) Bublitz, G. U.; Boxer, S. G. *Annual Review of Physical Chemistry* **1997**, *48*, 213.

(118) Andrews, S. S.; Boxer, S. G. *The Journal of Physical Chemistry A* **2000**, *104*, 11853.

(119) Andrews, S. S.; Boxer, S. G. *The Journal of Physical Chemistry A* **2002**, *106*, 469.

(120) Makov, G.; Nitzan, A.; Brus, L. E. *The Journal of Chemical Physics* **1988**, *88*, 5076.

(121) Plieth, W. J. *The Journal of Physical Chemistry* **1982**, *86*, 3166.

(122) Ivanova, O. S.; Zamborini, F. P. *Analytical Chemistry* **2010**, *82*, 5844.

(123) Ivanova, O. S.; Zamborini, F. P. *Journal of the American Chemical Society* **2010**, *132*, 70.

(124) Zhang, X.; Hicks, E. M.; Zhao, J.; Schatz, G. C.; Van Duyne, R. P. *Nano letters* **2005**, *5*, 1503.

(125) Wilson, A. J.; Willets, K. A. *Analyst* **2016**.

(126) Ni, F.; Feng, H.; Gorton, L.; Cotton, T. M. *Langmuir* **1990**, *6*, 66.

(127) Hermanson, G. T. In *Bioconjugate Techniques (Third edition)*; Academic Press: Boston, 2013, p 259.

(128) Kubin, R. F.; Fletcher, A. N. *Journal of Luminescence* **1982**, *27*, 455.

(129) van de Linde, S.; Krstic, I.; Prisner, T.; Doose, S.; Heilemann, M.; Sauer, M. *Photochemical & Photobiological Sciences* **2011**, *10*, 499.

(130) Klingsporn, J. M.; Jiang, N.; Pozzi, E. A.; Sonntag, M. D.; Chulhai, D.; Seideman, T.; Jensen, L.; Hersam, M. C.; Duyne, R. P. V. *Journal of the American Chemical Society* **2014**, *136*, 3881.

(131) Laviron, E. *Journal of Electroanalytical Chemistry and Interfacial Electrochemistry* **1974**, *52*, 355.

(132) Laviron, E. *Journal of Electroanalytical Chemistry and Interfacial Electrochemistry* **1979**, *100*, 263.

(133) Brown, A. P.; Anson, F. C. *Analytical Chemistry* **1977**, *49*, 1589.

(134) Le Ru, E. C.; Etchegoin, P. G. In *Principles of Surface-Enhanced Raman Spectroscopy*; Elsevier: Amsterdam, 2009, p 185.

(135) Etchegoin, P. G.; Le Ru, E. C. *Analytical Chemistry* **2010**, *82*, 2888.

(136) Brady, J. L. In *Association for the Advancement of Medical Instrumentation* 2010.

(137) Carayon, P.; Hundt, A. S.; Wetterneck, T. B. *International Journal of Medical Informatics* **2010**, *79*, 401.

(138) Zengin, A.; Tamer, U.; Caykara, T. *Analytica Chimica Acta* **2014**, *817*, 33.

(139) Rebe Raz, S.; Bremer, M. G. E. G.; Haasnoot, W.; Norde, W. *Analytical Chemistry* **2009**, *81*, 7743.

(140) He, L.; Rodda, T.; Haynes, C. L.; Deschaines, T.; Strother, T.; Diez-Gonzalez, F.; Labuza, T. P. *Analytical Chemistry* **2011**, *83*, 1510.

(141) Wilson, L. E.; Blythe, D.; Sharfstein, J. M. *JAMA* **2012**, *308*, 2461.

(142) Dresser, R. *Hastings Center Report* **2013**, *43*, 9.

(143) Stiles, P. L.; Dieringer, J. A.; Shah, N. C.; Van Duyne, R. P. *Annual Reviews of Analytical Chemistry* **2008**, *1*, 601.

(144) Sharma, B.; Fernanda Cardinal, M.; Kleinman, S. L.; Greeneltch, N. G.; Frontiera, R. R.; Blaber, M. G.; Schatz, G. C.; Van Duyne, R. P. *MRS Bulletin* **2013**, *38*, 615.

(145) Premasiri, W. R.; Moir, D. T.; Klempner, M. S.; Krieger, N.; Jones, G.; Ziegler, L. D. *The Journal of Physical Chemistry B* **2005**, *109*, 312.

(146) Brosseau, C. L.; Casadio, F.; Van Duyne, R. P. *Journal of Raman Spectroscopy* **2011**, *42*, 1305.

(147) Masango, S. S.; Hackler, R. A.; Large, N.; Henry, A.-I.; McAnally, M. O.; Schatz, G. C.; Stair, P. C.; Van Duyne, R. P. *Nano Letters* **2016**.

(148) Jin, J.; Ouyang, X.; Li, J.; Jiang, J.; Wang, H.; Wang, Y.; Yang, R. *Analyst* **2011**, *136*, 3629.

(149) Tsoutsi, D.; Montenegro, J. M.; Dommershausen, F.; Koert, U.; Liz-Marzán, L. M.; Parak, W. J.; Alvarez-Puebla, R. A. *ACS Nano* **2011**, *5*, 7539.

(150) Ma, K.; Yuen, J. M.; Shah, N. C.; Walsh, J. T., Jr.; Glucksberg, M. R.; Van Duyne, R. P. *Analytical Chemistry* **2011**, *83*, 9146.

(151) Shah, N. C.; Lyandres, O.; Walsh, J. T. J.; Glucksberg, M. R.; Van Duyne, R. P. *Analytical Chemistry* **2007**, *79*, 697.

(152) Yuen, J. M.; Shah, N. C.; Walsh, J. T.; Glucksberg, M. R.; Van Duyne, R. P. *Analytical Chemistry* **2010**, *82*, 8382.

(153) Lee, N.-S.; Hsieh, Y.-Z.; Paisley, R. F.; Morris, M. D. *Analytical Chemistry* **1988**, *60*, 442.

(154) Robinson, A. M.; Harroun, S. G.; Bergman, J.; Brosseau, C. L. *Analytical Chemistry* **2012**, *84*, 1760.

(155) Zhao, L.; Blackburn, J.; Brosseau, C. L. *Analytical Chemistry* **2015**, *87*, 441.

(156) Salverda, J. M.; Patil, A. V.; Mizzon, G.; Kuznetsova, S.; Zauner, G.; Akkilic, N.; Canters, G. W.; Davis, J. J.; Heering, H. A.; Aartsma, T. J. *Angewandte Chemie* **2010**, *49*, 5776.

(157) Hawley, M. D.; Tatawawadi, S. V.; Piekarski, S.; Adams, R. N. *Journal of the American Chemical Society* **1967**, *89*, 447.

(158) Zhang, Z.; Huang, J.; Wu, X.; Zhang, W.; Chen, S. *Journal of Electroanalytical Chemistry* **1998**, *444*, 169.

(159) Duval Malinsky, M.; Kelly, K. L.; Schatz, G. C.; Van Duyne, R. P. *The Journal of Physical Chemistry B* **2001**, *105*, 2343.

(160) McFarland, A. D.; Young, M. A.; Dieringer, J. A.; Van Duyne, R. P. *The Journal of Physical Chemistry B* **2005**, *109*, 11279.

(161) Zhao, J.; Dieringer, J. A.; Zhang, X.; Schatz, G. C.; Van Duyne, R. P. *The Journal of Physical Chemistry C* **2008**, *112*, 19302.

(162) Salama, S.; Stong, J. D.; Neilands, J. B.; Spiro, T. G. *Biochemistry* **1978**, *17*, 3781.

(163) Wang, P.; Xia, M.; Liang, O.; Sun, K.; Cipriano, A. F.; Schroeder, T.; Liu, H.; Xie, Y.-H. *Analytical Chemistry* **2015**, *87*, 10255.

(164) Puerto, E. D.; Cuesta, A.; Sanchez-Cortes, S.; Garcia-Ramos, J. V.; Domingo, C. *Analyst* **2013**, *138*, 4670.

(165) Corti, R.; Fuster, V. *European Heart Journal* **2011**.

(166) Saravanakumar, G.; Kim, K.; Park, J. H.; Rhee, K.; Kwon, I. C. *Journal of Biomedical Nanotechnology* **2009**, *5*, 20.

(167) Romer, T. J.; Brennan, J. F. I.; Fitzmaurice, M.; Feldstein, M. L.; Deinum, G.; Myles, J. L.; Kramer, J. R.; Lees, R. S.; Feld, M. S. *Circulation* **1998**, *97*, 878.

(168) van de Poll, S. W. E.; Romer, T. J.; Puppels, G. J.; van der Laarse, A. *Journal of Cardiovascular Risk* **2002**, *9*, 255.

(169) Motz, J. T.; Fitzmaurice, M.; Miller, A.; Gandhi, S. J.; Haka, A. S.; Galindo, L. H.; Dasari, R. R.; Kramer, J. R.; Feld, M. S. *Journal of Biomedical Optics* **2006**, *11*, 021003.

(170) Nogueira, G. V.; Silveira, L.; Martin, A. A.; Zangaro, R. A.; Pacheco, M. T.; Chavantes, M. C.; Pasqualucci, C. A. *Journal of Biomedical Optics* **2005**, *10*, 031117.

(171) Olsztynska-Janus, S.; Gasior-Glogowska, M.; Szymborska-Malek, K.; Komorowska, M.; Witkiewicz, W.; Pezowicz, C.; Szotek, S.; Kobielarz, M. *Acta of Bioengineering and Biomechanics* **2012**, *14*, 121.

(172) Buschman, H. P.; Motz, J. T.; Deinum, G.; Römer, T. J.; Fitzmaurice, M.; Kramer, J. R.; van der Laarse, A.; Bruschke, A. V.; Feld, M. S. *Cardiovascular Pathology* **2001**, *10*, 59.

(173) Matousek, P. *Chemical Society reviews* **2007**, *36*, 1292.

(174) Matousek, P.; Stone, N. *Journal of Biophotonics* **2013**, *6*, 7.

(175) Stone, N.; Baker, R.; Rogers, K.; Parker, A. W.; Matousek, P. *Analyst* **2007**, *132*, 899.

(176) Buckley, K.; Matousek, P.; Parker, A. W.; Goodship, A. E. *Journal of Raman Spectroscopy* **2012**, *43*, 1237.

(177) Sharma, B.; Ma, K.; Glucksberg, M. R.; Van Duyne, R. P. *Journal of the American Chemical Society* **2013**, *135*, 17290.